FACULTY OF ENGINEERING OF THE UNIVERSITY OF PORTO

Drug-Coated Melt Electrowritten Mesh Implants for Pelvic Organ Prolapse Repair

Ana Sofia Wanzeller Lacerda Soares de Sousa



Dissertation elaborated within the scope of the Master's in Biomedical Engineering

Supervisor: Prof. Doutora Maria Elisabete Teixeira da Silva

Co-supervisor: Prof. Doutora Sofia Costa de Oliveira

Co-supervisor: Prof. Doutor António Augusto Fernandes

June 24, 2024

Drug-Coated Melt Electrowritten Mesh Implants for Pelvic Organ Prolapse Repair

Ana Sofia Wanzeller Lacerda Soares de Sousa

Dissertation elaborated within the scope of the Master's in Biomedical Engineering

June 24, 2024

Abstract

In the recent years, pelvic organ prolapse cases have been rising, affecting women's quality of life. Synthetic surgical transvaginal meshes previously used for this disease's treatment were withdrawn from the United States market in 2019 based on the high risks associated with these products, such as infection, erosion of the mesh through the vagina, and recurrent prolapse. As a result, the development of meshes made from biodegradable materials has emerged as an alternative solution, as well as the use of 3D printing technology to produce them.

In the dissertation experimental work, polycaprolactone meshes for pelvic organ prolapse repair were produced through a melt electrospinning writing prototype. Their mechanical properties were evaluated through uniaxial tensile and cyclic tests. The meshes were further coated with antibiotics commonly used for the treatment of genitourinary tract infections: azithromycin (0.15% and 0.20%), gentamicin sulfate (1% and 2%), and ciprofloxacin (0.9%). Microbiological assays, including zone inhibition and biofilm formation assays, were also conducted to assess the antibiotics' effectiveness in preventing mesh infection against common bacterial strains in these infections, *Escherichia coli (E. coli)*, and both susceptible *(MSSA)* and methicilin-resistant *Staphylococcus aureus (MRSA)*.

Regarding the mechanical tests, the printed meshes exhibited closer mechanical behavior to human vaginal tissues than Restorelle® commercial mesh, which presents greater stiffness. Meshes of smaller filament diameter and larger pore size are more promising, particularly 160 μm with 1.5 mm pores. Additionally, the square geometry limits the mechanical behavior of the printed meshes, differing from the vaginal tissue behavior. The printed meshes endured cyclic loading for 100 cycles, mimicking *in vivo* loads, with reduced strain variation. It was also verified that meshes subjected to uniaxial loading after cyclic loading conditions presented more rigidity and higher stress values.

A Fourier transform infrared (FTIR) analysis confirmed the incorporation of antibiotics, except for the azithromycin-coated meshes. In the zone inhibition assay for *MSSA* ATCC 29213, the antimicrobial effect was verified for all of the antibiotics. Ciprofloxacin displayed antibacterial activity against *MRSA* ATCC 43300. Only the lowest concentration of azithromycin proved not to have an antibacterial effect for *E. coli* ATCC 25922. Gentamicin and ciprofloxacin displayed potential inhibitory activity against biofilm formation in *MSSA* ATCC 29213 and *E. coli* ATCC 25922, as well as ciprofloxacin against *MRSA* ATCC 43300. The obtained scanning electron microscopy images support these conclusions.

Keywords: Antibiotic Incorporation; Biodegradable Mesh; Cyclic Loading Conditions; Melt Electrospinning Writing; Pelvic Organ Prolapse.

Resumo

Nos últimos anos os casos de prolapso de órgãos pélvicos têm vindo a aumentar, afetando a qualidade de vida de mulheres. As malhas cirúrgicas transvaginais sintéticas anteriormente utilizadas para o tratamento desta condição foram retiradas do mercado dos Estados Unidos em 2019, devido aos elevados riscos associados a estes produtos, como infeção, erosão da malha através da vagina e prolapso recorrente. Como resultado, o desenvolvimento de malhas constituídas por materiais biodegradáveis tem surgido como uma solução alternativa, bem como o uso de tecnologias de impressão 3D para a sua produção.

No trabalho experimental realizado foram produzidas malhas para o reparo do prolapso dos órgãos pélvicos, compostas por policaprolactona através de um protótipo de *melt electrospinning writing* e as suas propriedades mecânicas foram avaliadas através de ensaios de tração uniaxial e ensaios cíclicos. As malhas foram depois revestidas com antibióticos comummente utilizados para o tratamento de infeções no trato genitourinário, azitromicina (0.15% e 0.20%), sulfato de gentamicina (1% e 2%) e ciprofloxacina (0.9%). Foram realizados ensaios microbiológicos, incluindo ensaios de inibição de zona e de formação de biofilme para avaliar a eficácia dos antibióticos na prevenção da infeção das malhas contra estirpes bacterianas comuns nestas infecções, nomeadamente *Escherichia coli*, e *Staphylococcus aureus* resistente *(MRSA)* e suscetível à meticilina *(MSSA)*.

Nos testes mecânicos as malhas impressas exibiram propriedades mecânicas mais próximas de tecidos vaginais humanos que a malha comercial Restorelle®, que apresenta elevada rigidez. Malhas com menores diâmetro e poros superiores são promissoras, nomeadamente, as malhas de 160 μm e poro de 1.5 mm. Quanto à geometria das malhas, a geometria quadrada limita o comportamento mecânico das malhas impressas, diferindo do comportamento do tecido vaginal. As malhas impressas resistiram a carga cíclica durante 100 ciclos com reduzida deformação. Também foi verificado que, quando sujeitas a tração uniaxial, as malhas apresentaram maior rigidez e tensão após sofrerem carga cíclica.

A análise FTIR comprovou a incorporação dos fármacos, exceto para as malhas revestidas com azitromicina. No ensaio de inibição de zona para *MSSA* ATCC 29213, o efeito antimicrobiano foi verificado para todos os antibióticos. A ciprofloxacina demonstrou atividade antibacteria contra *MRSA* ATCC 43300. Apenas a concentração mais baixa de azitromicina provou não ter efeito antibacteriano contra *E. coli* ATCC 25922. A gentamicina e a ciprofloxacina mostraram potencial atividade inibitória contra a formação de biofilme em *MSSA* ATCC 29213 e *E. coli* ATCC 25922, assim como a ciprofloxacina contra *MRSA* ATCC 43300. As imagens obtidas pelo microscópio eletrônico de varredura comprovaram as conclusões retiradas.

Palavras-Chave: Incorporação de Antibióticos; Malha Biodegradável; Condições de Carga Cíclica; *Melt Electrospinning Writing*; Prolapso dos Órgãos Pélvicos.

Acknowledgements

First and foremost, I would like to express my sincere gratitude and appreciation to my supervisor, Dr. Elisabete Silva, and co-supervisors, Dr. Sofia Oliveira and Prof. Dr. António Augusto Fernandes, for their support and guidance throughout the development of my dissertation.

I want to thank Prof. Abílio de Jesus for the expertise and valuable knowledge transmitted. I would also like to thank the members of the Microbiology Laboratory in the Pathology Department at the Faculty of Medicine of the University of Porto (FMUP) for their warm welcome and kindness during my time there.

I want to express my heartfelt thanks to my colleagues at the Product and Services Development Laboratory (LDPS) for their advice and for brightening my days during coffee breaks. Special thanks to Fábio Pinheiro, Joana Martins, Francisca Vaz, Ana Pais, Nuno Ferreira, and Lucas Lopes.

I am sincerely grateful to my family for their unwavering support and belief in me. To my friends in Lisbon, thank you for always being there for me and for the countless phone calls. To my friends from home, your support means the world to me. To my friends in Porto, thank you for making it feel like home and for being by my side throughout this journey.

I am truly grateful to everyone who has influenced my journey.

Lastly, I gratefully acknowledge the Emprego Científico 2021.00077.CEECIND, funded by FCT - Fundação para a Ciência e a Tecnologia. This work was supported by FCT, through INEGI, in the scope of LAETA, project UIDB/50022/2020 and UIDP/50022/2020. Additionally, this research was funded by National Funds through FCT, I.P., within CINTESIS, R&D Unit (reference UIDP/4255/2020) and RISE LA/P/0053/2020.

Contents

1 Introduction **1**
- 1.1 Motivation . . . 1
- 1.2 Objectives . . . 2
- 1.3 Structure . . . 2

2 Female Pelvis: anatomy and dysfunction **5**
- 2.1 Female Pelvis Anatomy . . . 5
- 2.2 Pelvic Organ Prolapse . . . 7
  - 2.2.1 Diagnosis and Classification . . . 8
  - 2.2.2 Treatment Options . . . 9
  - 2.2.3 Surgical Pelvic Meshes . . . 10

3 Polymer Processing Techniques **15**
- 3.1 Electrospinning . . . 15
  - 3.1.1 Process . . . 16
  - 3.1.2 Solution Electrospinning and Melt Electrospinning . . . 16
- 3.2 Additive Manufacturing . . . 18
- 3.3 Melt Electrospinning Writing . . . 19
  - 3.3.1 Process . . . 19
  - 3.3.2 Parameters . . . 20

4 Infection: predisposing factors and treatment **23**
- 4.1 Mesh-related Infection: Pathogens . . . 23
- 4.2 Predisposing Factors for Infection . . . 24
- 4.3 Adhesion and Biofilm Formation . . . 24
- 4.4 Treatment and Prevention of Infection . . . 26

5 Materials and Methods **29**
- 5.1 Materials . . . 29
  - 5.1.1 Technical-Grade PCL . . . 29
  - 5.1.2 Antibiotics . . . 29
  - 5.1.3 Bacteria Strains . . . 30
- 5.2 Instruments and Tools . . . 30
  - 5.2.1 Mesh Production . . . 30
  - 5.2.2 Mechanical Tests . . . 31
  - 5.2.3 Antimicrobial Incorporation and Evaluation . . . 31
  - 5.2.4 Microbiological Assays . . . 33
  - 5.2.5 Statistical Analysis . . . 33
- 5.3 Experimental Procedures . . . 33

5.3.1 Mesh Production and Characteristics 34
5.3.2 Mechanical Tests 36
5.3.3 Antimicrobial Incorporation and Evaluation 37
5.3.4 Zone Inhibition Assays 38
5.3.5 Biofilm Formation Assays 39

6 Mechanical Tests Results **41**
6.1 Uniaxial Tensile Tests 41
6.2 Cyclic Tests 42
6.3 Tensile Tests After Cyclic Loading Conditions 44
6.4 Results Analysis 44

7 Antimicrobial Incorporation Results **47**
7.1 FTIR Spectroscopy 47
7.2 Microbiological Assays 50
7.2.1 Zone Inhibition Assay 50
7.2.2 Biofilm Formation Assays 52
7.3 Result Analysis 56

8 Conclusions and Future Work **61**
8.1 Conclusions 61
8.2 Limitations and Future Work 62

References **65**

List of Figures

2.1 Division of the pelvis. 5
2.2 Female bony pelvis (pelvic girdle). 6
2.3 Female pelvic cavity organs. 6
2.4 Female pelvic cavity floor. 7
2.5 Types of pelvic organ prolapse. 8
2.6 Example of measurements using the POP-Q system. 9
2.7 Vaginal pessaries used for the treatment of pelvic organ prolapse. 10
2.8 Representation of woven (left) and knitted (right) meshes. 11

3.1 Schematic of the ES process. 16
3.2 Formation of Taylor cone. 16
3.3 Schematic of the SES process. 17
3.4 Schematic of the MES process. 17
3.5 Schematic of the FFF process. 18
3.6 Schematic of a MEW device. 19

4.1 Schematic representation of biofilm formation. 25
4.2 Chemical structure of azithromycin. 26
4.3 Chemical structure of gentamicin sulfate. 27
4.4 Chemical structure of ciprofloxacin. 27

5.1 MEW prototype. 31
5.2 Mechanical Testing Machine. 32
5.3 Agilent Cary 360 FTIR Spectrometer. 32
5.4 Experimental procedures performed, their main characteristics or objective. . . . 34
5.5 Scheme of the applied load during uniaxial tensile test. 36
5.6 Scheme of the applied load during cyclic tests. 37

6.1 Stress-strain curves obtained through uniaxial tensile testing. 41
6.2 Stress-strain curve obtained from cyclic tests of (a) 240 μm samples with 1.5 mm pores; (b) 240 μm samples with 1 mm pores; (c) 160 μm samples with 1.5 mm pores; (d) 160 μm samples with 1 mm pores 43
6.3 Strain suffered at maximum stress in each cycle for a 240 μm mesh with 1 mm pores. 43
6.4 Effect of cyclic loading conditions on 240 μm samples with 1.5 and 1 mm pores. 44

7.1 FTIR spectrum of PCL meshes that were sterilized under UV-C light and PCL meshes that were not subjected to this process. 48
7.2 FTIR spectrum of meshes with solvent incorporation, compared with the control (PCL) spectrum. 48

7.3 FTIR spectra of meshes coated with azithromycin compared with the control (PCL) spectrum. 49
7.4 FTIR spectra of meshes coated with gentamicin sulfate compared with the control (PCL) spectrum. 49
7.5 FTIR spectrum of meshes coated with ciprofloxacin compared with the control (PCL) spectrum. 50
7.6 *MSSA* ATCC 29213 zone inhibition assay results for: (a) Azithromycin (Az); (b) Gentamicin Sulfate (GS); (c) Ciprofloxacin (Cipro). 51
7.7 *MRSA* ATCC 43300 zone inhibition assay results for: (a) Azithromycin (Az); (b) Gentamicin Sulfate (GS); (c) Ciprofloxacin (Cipro). 51
7.8 *E. coli* ATCC 25922 zone inhibition assay results for: (a) Azithromycin; (b) Gentamicin Sulfate; (c) Ciprofloxacin. 52
7.9 SEM images of PCL meshes and incorporated solvents. 53
7.10 *MSSA* ATCC 29213 biofilm formation: (a) XTT assay; (b) CV assay. 53
7.11 SEM images of *MSSA* ATCC 29213 antibiotic loaded meshes. 54
7.12 *MRSA* ATCC 43300 biofilm formation: (a) XTT assay; (b) CV assay. 54
7.13 SEM images of *MRSA* ATCC 43300 in drug-loaded meshes. 55
7.14 *E. coli* ATCC 25922 biofilm formation: (a) XTT assay; (b) CV assay. 55
7.15 SEM images of *E. coli* ATCC 25922 in meshes with antibiotic incorporation. . . 56

List of Tables

2.1 Classification of meshes according to porosity proposed by Amid. 12
2.2 Classification of meshes according to density proposed by *Coda et al.*. 12
2.3 Classification of meshes proposed by Klinge and Klosterhalfen. 13

3.1 Examples of polymers used for SES and MES. 18

5.1 Characteristics of PCL meshes. 35
5.2 Process parameters used in the MEW prototype for printing the 240 and 160 μm meshes. 36

6.1 Maximum stress values obtained in the comfort zone from the stress-strain curves. 42
6.2 Human prolapsed vaginal tissue and Restorelle® maximum stress values in the comfort zone obtained from the literature. 42
6.3 Average strain variation calculated between the 1st and 100th in the cyclic tests. . 43
6.4 Maximum stress values and Young's modulus obtained after cyclic loading. . . . 44

7.1 PCL peaks detected in FTIR spectroscopy. 47
7.2 Gentamicin sulfate peaks detected in FTIR spectroscopy. 49
7.3 Ciprofloxacin peaks detected in FTIR spectroscopy. 50
7.4 Measured diameters of inhibition. 51

Abbreviations

3D	Three-dimensional
AM	Additive Manufacturing
AZ	Azithromycin
CFU	Colony Forming Unit
Cipro	Ciprofloxacin
E	Young's Modulus
ES	Electrospinning
FDA	Food and Drug Administration
FFF	Fused Filament Fabrication
FTIR	Fourier Transform Infrared Spectroscopy
GS	Gentamicin Sulfate
MES	Melt Electrospinning
MEW	Melt Electrospinning Writing
OD	Optical Density
PBS	Phosphate Buffered Saline
PCL	Polycaprolactone
PET	Polyethylene Terephthalate
PFD	Pelvic Floor Dysfunction
PFM	Pelvic Floor Muscles
PID	Pelvic Inflammatory Disease
PLA	Polylactic Acid
PLGA	Poly (Lactic-co-Glycolic Acid)
POP	Pelvic Organ Prolapse
PP	Polypropylene
PTFE	Polytetrafluoroethylene
PU	Polyurethane
PVDF	Polyvinylidenefluoride
SEM	Scanning Electron Microscopy
SES	Solution Electrospinning
SUI	Stress Urinary Incontinence
TPU	Thermoplastic Polyurethane
UTI	Urinary Tract Infection

Chapter 1

Introduction

In this chapter, introductory aspects of the dissertation are presented. First, the background and motivation of pelvic organ prolapse (POP) and the problems associated with the synthetic meshes used for its repair are mentioned. Then, 3D printing is approached as a solution to overcome these complications by printing meshes using biodegradable materials and incorporating antibiotics. Next, both the main and specific goals of the dissertation are specified. The structure of the dissertation is also present in this chapter.

1.1 Motivation

Pelvic organ prolapse (POP) is one of the most common pelvic floor dysfunction (PFD) that concerns one or more organs in the pelvis slipping from their normal position and bulge into the vagina. This dysfunction occurs when tissues and muscles can no longer hold the organs due to several factors, such as pregnancy and age, affecting the quality of life of women. POP affects 40% of women aged between 45 and 85 years worldwide, but only 12% of these women present symptoms [1]. By 2050, the number of women experiencing POP is expected to increase by 46%. The treatment options for this condition vary depending on the prolapse severity, but in most severe cases, surgery is recommended [2]. In Portugal, POP affects around 7,000 women every year. This number is expected to increase by 40% over the next 40 years due to the rising average age of the female population [3].

In many of these surgeries, synthetic surgical meshes have been used. However, in 2019, the Food and Drug Administration (FDA) banned the production and distribution of transvaginal meshes for POP treatment in the United States. The FDA determined that the transvaginal meshes do not present safety and efficacy due to the high risks associated with these products, such as infection, erosion of the mesh through the vagina, and recurrent prolapse [4]. These complications often caused a need for mesh removal [5]. Considering the prevalence of POP, reducing the re-operation rates and complications is important, improving patient well-being [6].

To overcome this problem, with the evolution of technology come different materials, techniques, and ways to minimize the disadvantages of surgical meshes. Thus, biodegradable meshes

have been attracting the attention of researchers, as well as 3D printing for the production of surgical meshes for POP treatment. The electrospinning (ES) technology associated with 3D printing, melt electrospinning writing (MEW), has proven to be a valuable tool for producing complex and resistant structures. It allows the use of biodegradable polymers, such as polycaprolactone (PCL) that is FDA-approved for clinical use, and the incorporation of other substances, such as antimicrobial agents [7, 8].

The production of meshes with antimicrobial properties has been studied to inhibit bacterial growth and biofilm formation, ultimately preventing infection [9]. Gentamicin, azithromycin, and ciprofloxacin integration into polymers has proven to be effective against *Escherichia coli* (*E. coli*) and *Staphylococcus aureus* (*S. aureus*), common pathogens associated pelvic mesh infection [10, 11, 12].

Therefore, it is of utmost interest to produce anti-infective biodegradable meshes that are less stiff than synthetic meshes through MEW to prevent complications associated with pelvic meshes that lead to their removal.

1.2 Objectives

This dissertation's main goal is to contribute to the development of biodegradable mesh implants that are safer and more effective than synthetic meshes for female pelvic organ prolapse repair. The specific objectives of this dissertation are:

- Print technical-grade PCL meshes of different filament diameters and porosities with antibiotics incorporation through melt electrospinning writing to investigate the possibility of enhancing the mesh's mechanical properties and characteristics.
- Perform cyclic tests on the printed meshes to evaluate their long-term behavior when subjected to stress and strain cycles.
- Conduct microbiological assays to assess the effectiveness of the incorporated drugs in preventing biofilm formation and, therefore, mesh infection.

1.3 Structure

The dissertation is structured as follows:

- **Chapter 2 - Female Pelvis: anatomy and dysfunction:** Describes a literature review of the female pelvic anatomy and associated dysfunctions, in particular, pelvic organ prolapse, its symptoms, diagnosis, and treatment options. The use of synthetic meshes and the investigation of biodegradable meshes for surgical repair of pelvic organ prolapse are also covered in this chapter.

- **Chapter 3 - Polymer Processing Techniques:** Presents a theoretical review of the electrospinning technique, additive manufacturing, and its combination in melt electrospinning writing, the technique used in the developed work. Biomedical applications of this technique are also approached.
- **Chapter 4 - Infection: predisposing factors and treatment:** Describes the context of infection in pelvic meshes, microorganisms involved, and antimicrobial agents for infection treatment. Studies regarding drug incorporation in polymer processing techniques are also approached.
- **Chapter 5 - Materials and Methods:** This chapter introduces the materials, instruments, equipment, and tools employed in the experimental work. The experimental process and stages are also presented.
- **Chapter 6 - Mechanical Tests Results:** Outlines and discusses the results obtained from the mechanical tests, specifically the uniaxial tensile and cyclic tests.
- **Chapter 7 - Antimicrobial Incorporation Results:** In this chapter, the obtained results regarding antimicrobial incorporation in the meshes are presented and discussed. These consist of the Fourier-transform infrared spectroscopy (FTIR) analysis and the microbiological assays. More precisely, the zone inhibition and the biofilm formation assays. Images obtained through Scanning Electron Microscopy (SEM) are also presented.

Chapter 2

Female Pelvis: anatomy and dysfunction

The following chapter reviews the theoretical fundamentals to understand the disease behind the developed work. First, the female pelvis anatomy is described, as well as one of its dysfunctions, pelvic organ prolapse, and its context, such as symptoms, classification, diagnosis, and treatments. Then, a review of the existing synthetic surgical meshes and the development of biodegradable meshes is presented.

2.1 Female Pelvis Anatomy

The pelvis is a bony structure that supports the organs in the pelvic cavity, located between the abdomen, superiorly, and the thighs, inferiorly. It includes the bony pelvis or pelvic girdle, the pelvic cavity, the pelvic floor, and the perineum [13]. The female pelvis can be divided by an imaginary line as seen in Figure 2.1. The false or greater pelvis is situated above this line, involving the lower lumbar vertebra, the abdominal cavity, and part of the small intestine. On the other hand, the true or lesser pelvis is below the line and contains the reproductive organs, the distal part of the urinary tract [14, 15].

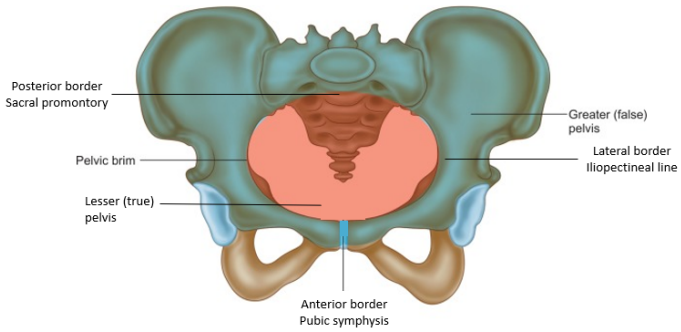


Figure 2.1: Division of the pelvis (adapted from [16]).

The primary roles of the pelvis include supporting the spinal column, transferring weight from the upper body towards the lower limbs, serving as an attachment point for muscles, and safeguarding the organs and vessels located within the pelvic cavity [14].

The skeletal structure known as the bony pelvis or pelvic girdle connects the vertebral column to the two femora. It comprises the right and left hip bones at the front and sides and, posteriorly, the sacrococcygeal part of the vertebral column. It contains the sacrum, the coccyx, and two hip bones. Each hip bone is formed by the ilium, the pubis, and the ischium [16]. Within the bony pelvis, there are also four articulations: the symphysis pubis, responsible for connecting the hip bones anteriorly; two sacroiliac joints, where the medial aspect of the hip bone articulates with the corresponding lateral aspect of the sacrum on both sides; and the sacrococcygeal joint, formed by the articulation between the inferior end of the sacrum and the upper surface of the coccyx [14]. The bony pelvis or pelvic girdle is represented in Figure 2.2, and provides structural support and protection for the pelvic floor and organs [17].

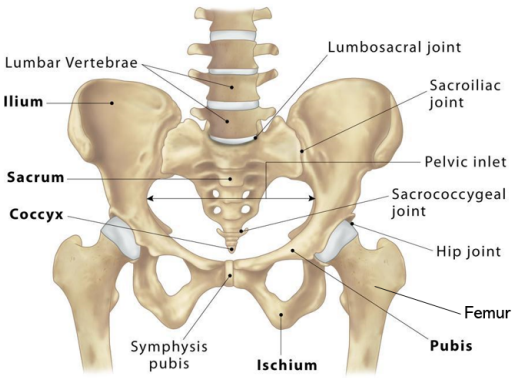


Figure 2.2: Female bony pelvis (pelvic girdle) (adapted from [17]).

The pelvic cavity is a hollow bony structure that sits between the abdominal cavity and the pelvic floor, consisting of the area inside the pelvic bones. It includes several organs of the gastrointestinal tract, musculoskeletal system, and urogenital system, such as the rectum, uterus, ovaries, fallopian tubes, vagina, urethra, bladder and ureters, as well as vessels, nerves and lymphatics [13]. Some of the female pelvic cavity organs are represented in Figure 2.3.

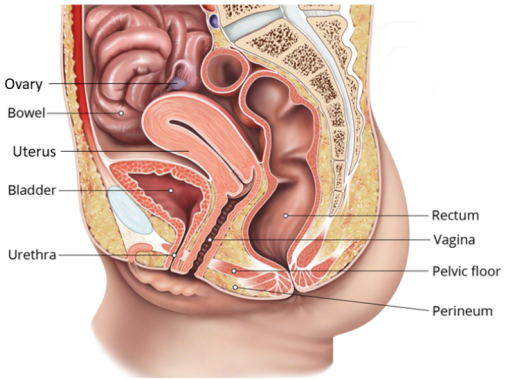


Figure 2.3: Female pelvic cavity organs (adapted from [18]).

The pelvic floor comprises the muscles, ligaments, and fascia supporting the organs in the pelvic cavity [19]. It presents a diamond-like shape and can be divided by drawing a line between the two ischial spines into anterior and posterior compartments [16].

The pelvic floor muscles (PFM) not only keep the organs in position but also provide the necessary flexibility required for bodily functions. Levator ani and coccygeus are the primary muscles and are present bilaterally. The levator ani comprises the pubococcygeus, puborectalis, and iliococcygeus muscles and composes the bulk of the PFM. The coccygeus is located in the back of the pelvis and is a muscle of smaller dimensions [19].

The pelvis muscles have a superficial and a deep layer (Figure 2.4). The deep pelvic floor is formed by the iliococcygeus, puborectalis, and pubovisceral muscles. The superficial muscles are ischiocavernosus, bulbospongiosus, and superficial transverse perineal [16].

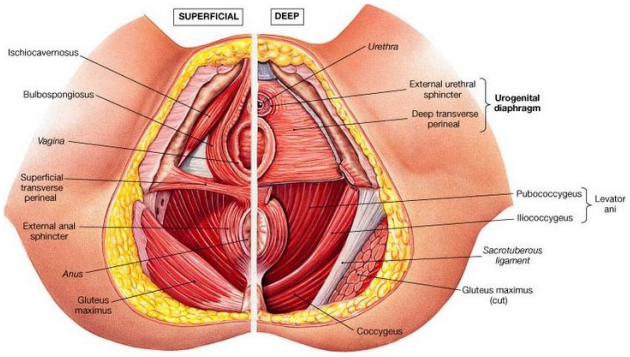


Figure 2.4: Female pelvic floor (adapted from [20]).

2.2 Pelvic Organ Prolapse

Pelvic Floor Dysfunction (PFD) consists of abnormal function of the female PFM when these muscles are too relaxed or tight, affecting women's quality of life. The main manifestations of PFD are pelvic organ prolapse (POP), stress urinary incontinence (SUI), fecal incontinence (FI), and overactive bladder (OAB) syndrome [21]. These disorders can coexist and affect 30 to 50% of middle-aged to elderly women. This percentage is expected to grow 46% by 2050, with the increase of average life expectancy [2, 22].

POP, one of the most common PFD, is described as a protrusion of the pelvic organs through the vaginal walls and pelvic floor when ligaments, connective tissues, and muscles can no longer hold them due to lesions or weakness [6]. As can be seen in Figure 2.5, different types of POP are distinguished by the specific anatomical region or organ that is impacted. In cystocele or anterior vaginal wall prolapse, there's a bladder prolapse. In enterocele and urethrocele, there is a small intestine and urethra prolapse into the vagina, respectfully. In rectocele or posterior vaginal wall prolapse, there is a prolapse of the rectum. In vaginal vault prolapse, the top part of the vagina falls into the vaginal canal [23].

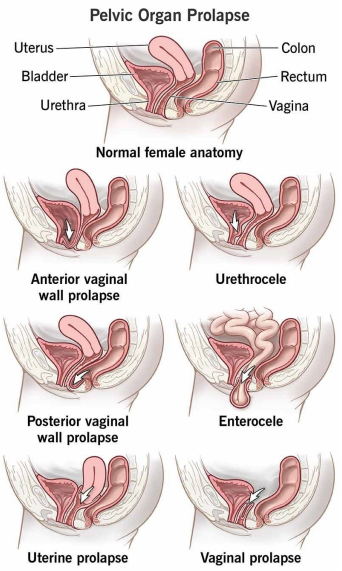


Figure 2.5: Types of pelvic organ prolapse (adapted from [24]).

There are several risk factors for developing POP, such as elevated mass index, age, vaginal delivery, smoking, physical activity, hysterectomy status, menopausal status, levator hiatal area, levator defect, and pregnancy, the most common one. Most patients with POP are asymptomatic; only 12% of them report symptoms. Some of these symptoms include feeling a bulge past the vaginal opening, urinary problems, discomfort around the genital area, and vaginal spotting, although these depend on the prolapsed organ [1].

2.2.1 Diagnosis and Classification

The diagnosis consists mainly of performing a pelvic exam, but bladder function tests and imaging procedures can also be included [2]. The prolapse is classified using a pelvic organ prolapse quantification (POP-Q) system to assess its severity. In this quantification method, the measurements are in centimeters (cm) with the plane of the hymen as a reference. Measurements above or proximal are negative numbers, and below or distal are positive numbers. There are six defined points to measure in POP-Q (Aa, Ba, C, D, Ap, Bp), and the genital hiatus (GH), total vaginal length (TVL), and perineal body (PB) are also taken into account. The measurements for each location can be organized into a grid, as shown in Figure 2.6. According to POP-Q there are five stages [25, 26]:

- Stage 0: No prolapse is observed.
- Stage 1: The prolapse is more than 1 cm above the level of the hymen.
- Stage 2: The prolapse is 1 cm above or below the hymen level.
- Stage 3: The most distal portion of the prolapse protrudes between 1 cm to 2 cm less than the total vaginal length below the hymen.
- Stage 4: Vaginal eversion is essentially complete.

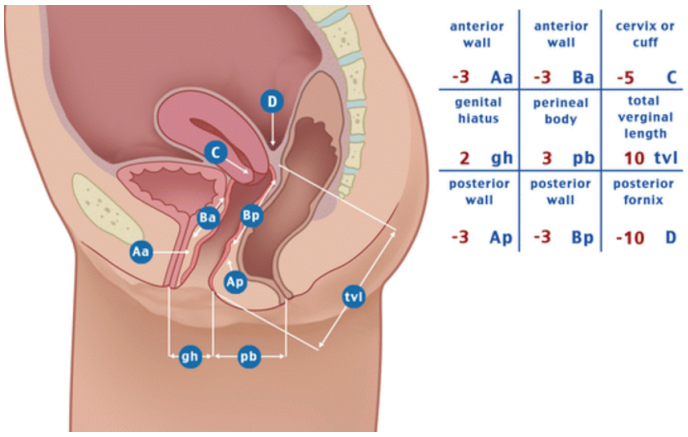


Figure 2.6: Example of measurements using the POP-Q system [27].

For symptoms associated with prolapse during the pelvic exam, there can be performed several exams such as a cystoscopy, a defecography, a magnetic resonance image (MRI), a computerized tomography (CT) scan, and an ultrasound to assess the severity of the prolapse [28].

2.2.2 Treatment Options

Treatment options for POP vary according to the severity of the symptoms and the patient's characteristics. These can be surgical or non-surgical. The non-surgical options include: lifestyle changes, for example, weight loss; physical therapy; hormonal treatments; and vaginal pessaries [29].

Physical therapy might be recommended for less severe cases of POP, from stage 1 to 3. The physical therapist teaches pelvic floor exercises or *Kegel* exercises to strengthen the pelvic muscles through contractions and relaxations [30]. Physical therapy using biofeedback is another option that involves monitoring with sensors placed in the vagina, rectum, or skin of the patient. As the exercises are performed, a screen shows the muscle contraction and its strength to teach how to perform the exercises [29]. Biofeedback therapy using electrical stimulation can also stimulate pelvic tissue nerves with current pulses [31].

Concerning hormonal treatments, the administration of oestrogen is used to treat POP either alone or in combination with other treatment options. However, performed studies present insufficient evidence regarding the benefits or harms of oestrogen therapy for managing POP symptoms in postmenopausal women [32, 33].

Another non-surgical solution for POP treatment is the use of vaginal pessaries, removable devices that can be inserted into the vagina to support the pelvic walls and organs. These are composed of soft, non-absorbent, and inert materials, like silicone. Vaginal pessaries can have different shapes and sizes, but mainly there are two types of pessaries, support pessaries, and space-filling pessaries, as shown in Figure 2.7. The first type is used in various types of prolapse and SUI, while the last is usually used for more complex cases [34].

The usage time of these devices varies; some can be used for months, while others have to be replaced daily. A six-monthly follow-up of the patients who can insert the devices by themselves

is recommended, with more frequent follow-ups for patients who cannot self-insert. It is also advised to alternate between two types of pessaries [34, 35]. Although pessaries are treatment options associated with high levels of satisfaction (75.3%) and efficacy (90.7%), they can present some few complications like vaginal irritation, bleeding, and ulceration, which means there may be a need to remove the pessary until the lesions are cured. Also, if the pessary is not the right size, it can cause pain or discomfort [36].

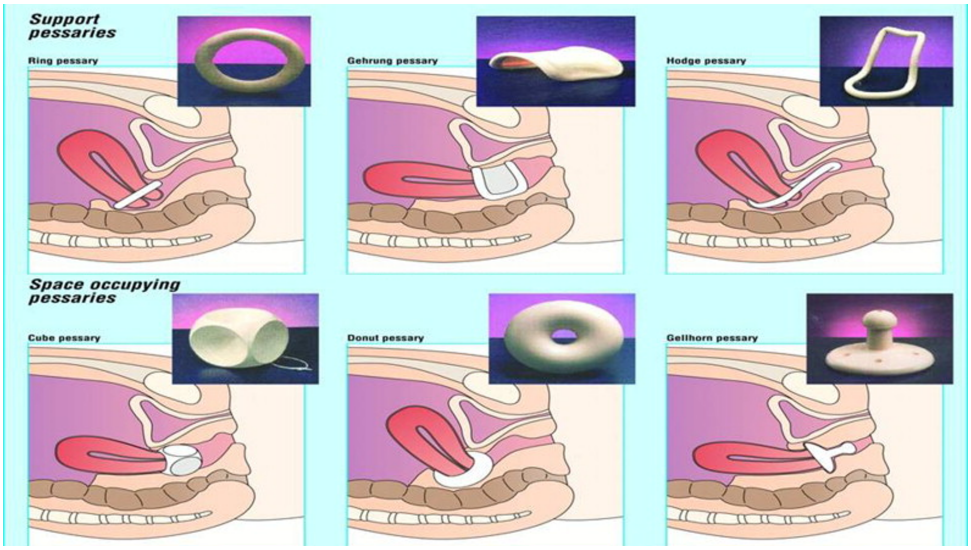


Figure 2.7: Vaginal pessaries used for the treatment of pelvic organ prolapse (adapted from [34]).

When the previous options are not enough, or the prolapse is severe, the doctors will suggest performing surgery. In general, there are two types of surgery: obliterative and reconstructive. In obliterative surgery or colpocleisis, the vagina is narrowed to provide support for prolapsed organs. This surgery has high success rates but is usually advised for older women [37]. On the other hand, in reconstructive surgery, the organs are restored to their original position using the patient's tissues - native tissue repair - or surgical meshes, as will be discussed later. These surgeries can be performed through an incision in the vagina, but also through an incision in the abdomen or through minimally invasive approaches, such as laparoscopic and robotic-assisted techniques, reducing scarring and complications [38, 30].

It's important to consider that recurrent prolapse is common in reconstructive surgery, with a re-operation rate of 30%, as surgery doesn't repair the underlying weakened tissues [6, 29]. Regarding the surgeries using native tissues to restore the prolapsed organs, although these are an option, they still present a high failure rate of 29% [39].

2.2.3 Surgical Pelvic Meshes

Surgical meshes are medical devices that support weak or damaged tissues. As stated before, there are surgical POP treatment approaches that include the use of biologic grafts or synthetic surgical meshes [40]. Biological grafts can be produced from porcine, bovine, or human tissue

[27]. Most surgical meshes are produced with synthetic materials since the meshes made from animal tissues do not perform as well as those produced in a laboratory setting [41].

The emergence of synthetic surgical meshes for pelvic floor reconstruction began in the 1970s when gynecologists started using surgical meshes intended for hernia repair for pelvic floor reconstructive surgery. Since these implants were not appropriate for the pelvic floor, medical device companies started developing meshes with different characteristics, shapes, and sizes. This led to the Food and Drug Administration (FDA) approval of the first pelvic mesh product made of polypropylene (PP), ProtoGen Sling®(Boston Scientific, USA) in 1996, intended for SUI treatment. From this point on, other implants emerged from different manufacturers due to their similarity to ProtoGen Sling®, even though no clinical trials were performed. In 2002, the FDA approved the use of these implants for POP treatment [7, 42].

Synthetic surgical meshes vary and can be classified according to characteristics such as porosity, density, mechanical properties, structure, filament type, and absorption capacity since these can influence cell attachment and regeneration [43].

The materials used to manufacture the mesh can be absorbable, non-absorbable, or a combination of both. Some non-absorbable materials used to produce meshes are polypropylene (PP), polyethylene terephthalate (PET), polyvinylidene fluoride (PVDF), or polytetrafluoroethylene (PTFE) [44]. These meshes maintain their mechanical properties but are stiffer, which causes weakening of the surrounding tissues and can cause infection after the implantation. On the other hand, absorbable meshes degrade during the healing process, tending to lose tensile strength once absorbed, but are not usually associated with infection. Examples of absorbable materials are polycaprolactone (PCL), polylactic acid (PLA), poly(lactic-co-glycolic acid) (PLGA), and polyurethane (PU) [7].

Concerning the filament type, meshes can be composed of one filament (monofilament) or various filaments (multifilament). It has been shown that multifilament meshes increase the risk of infection due to the increased surface area and spaces within the filaments that allow bacterial entrance and growth. Multifilament meshes are usually soft and flexible, while monofilament ones are stiffer and have limited flexibility [7, 45].

According to structure, the meshes can be woven or knitted. Meshes produced through knitting consist of a single filament looped to create its structure, while woven implants consist of two different filaments crossed perpendicularly with each other as shown in Figure 2.8 [42, 45].

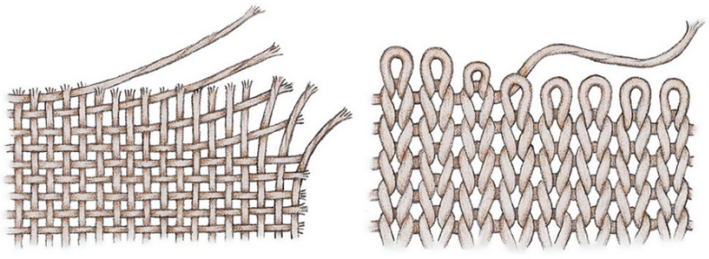


Figure 2.8: Representation of woven (left) and knitted (right) meshes [42].

Porosity is defined as the ratio of the space in a mesh and the area occupied by the mesh. Meshes are usually described as microporous or macroporous, depending on the pore's size. In 1997, Amid classified meshes into four groups that can be seen in Table 2.1 according to their porosity. Meshes with submicronic pores are not often used in prolapse surgery. The pore size of a mesh is crucial to determine its biocompatibility. Macroporous implants prevent the harboring and growth of bacteria, allowing more efficient infection combat and improving the host response to the mesh [7, 46].

Table 2.1: Classification of meshes according to porosity proposed by Amid (adapted from [46]).

Type	**Porosity**
Type I	Totally macroporous (> 75 μm)
Type II	Totally microporous (< 10 μm)
Type III	Macroporous with multifilaments or microporous components
Type IV	Sub-micronic pores (< 1 μm)

The mesh density was categorized by *Coda et al.* in 2012 by its weight into four groups shown in Table 2.2. The light-weight meshes tend to have lower inflammation rates since they have less material than the others [45, 47].

Table 2.2: Classification of meshes according to density proposed by *Coda et al.* (adapted from [47]).

Type	**Porosity**
Ultra-light	< 35 g/m^2
Light	35 - 70 g/m^2
Standard	70 - 140 g/m^2
Heavy	> 140 g/m^2

Also, in 2012, Klinge and Klosterhalfen performed a more profound analysis and classified meshes into six classes, as can be seen in Table 2.3. Class I and II consist of meshes with large and small pores, respectively. The meshes with special features from class III consist of meshes to prevent adhesions, for example, while those with films from class IV have submicronic pores or no porosity. Class V 3D meshes consist of implants that are not flat. At last, class VI refers to meshes of biological origin [48]. Besides these various classification systems, there is not one to be considered the best to be used [49].

Up to this date, three main surgical procedures have been performed using surgical meshes to treat PFD: mesh sling to treat SUI, POP treatment using transabdominal mesh, and POP treatment using transvaginal mesh. However, currently, there are no FDA-approved implants manufactured

for the transvaginal approach in the United States [50]. Restorelle® (Coloplast, Denmark) is a commercially available mesh used for other types of POP repair. It consists of an ultra-lightweight PP mesh made from knitted monofilaments. It has a density of 19 g/m^2 and a pore size of approximately 2 mm. This implant is composed of three filaments of 80 μm diameter [51].

Table 2.3: Classification of meshes proposed by Klinge and Klosterhalfen (adapted from [48]).

Class	Group	Subgroup
I	Large Pore Mesh	Ia) Monofilament
		Ib) Multifilament
		Ic) Mixed structure or polymer
II	Small Pore Mesh	IIa) Monofilament
		IIb) Multifilament
		IIc) Mixed structure or polymer
III	Meshes with Special Features	
IV	Meshes with Films	
V	3D Meshes	
VI	Biologicals	VIa) Non cross-linked
		VIb) Cross-linked
		VIc) Special Features

Although the introduction of synthetic meshes to the market has improved the treatment outcomes for POP, it has also brought several complications [7]. In 2016, the meshes used for transvaginal POP repair were classified as high-risk products instead of the previous moderate-risk classification. In 2019, the FDA banned the production and commercialization of transvaginal surgical meshes for POP in the United States based on the belief that the benefits did not outweigh the risks. Some of the reported complications were mesh erosion through the vagina, pain, infection, bleeding, urinary incontinence, and recurrent prolapse, making it necessary to perform another surgery [4]. It is believed that the reported complications are most likely due to insufficient biocompatibility and inappropriate biomechanical properties of these implants [51].

The mechanical properties of a mesh used for POP repair should be related to the organs and soft tissues the mesh is intended to support to avoid erosion and infection [7, 52]. The material used during the production of the mesh should be able to withstand at least 180 mmHg (20 kPa) before failing since the maximum intra-abdominal pressure in a healthy adult is approximately 170 mmHg [45]. An ideal mesh should be biocompatible, nontoxic, and have antibacterial properties and appropriate mechanical properties. The design should provide support without creating excessive tension, and the shape and size of the mesh should be specific to the patient. The placement technique is very important, as well as performing clinical tests and long-term monitoring to ensure the safety and effectiveness of the meshes [42].

Considering that the commercially available meshes nowadays are synthetic and knitted, research regarding the use of 3D printing methods and biodegradable materials has been performed [8]. Although an ideal mesh does not exist, with the evolution of technology come different techniques, materials, and ways to minimize the disadvantages of surgical meshes. Meshes composed of biodegradable materials like PCL, PLA, PLGA, and PU have been attracting the attention of investigators as an approach to solving the insufficient biocompatibility and inappropriate biomechanical properties related to the synthetic implants [7].

Chapter 3

Polymer Processing Techniques

This chapter presents the theoretical fundamentals regarding the polymer processing technique used in the developed work. First, electrospinning (ES) and additive manufacturing (AM) technologies are discussed. Then, the melt electrospinning writing (MEW) technique was addressed as a valuable tool to produce biodegradable meshes for pelvic organ prolapse repair. Studies regarding biomedical applications of MEW are also mentioned.

3.1 Electrospinning

Electrospinning (ES) is a well-known technique that uses a field of electrical forces to produce continuous polymer fibers from solution or melted materials. It allows the production of ultra-thin fibers with diameters down to the nanometer scale [53].

The concept of ES was first introduced in the 1600s when William Gilbert observed the formation of a cone-shaped water droplet in the presence of an electric field. In 1934, Anton Formhals patented this method, but it wasn't until the 1990s that it started gaining attention due to the increasing interest in nanotechnology [54, 55].

The typical components of an ES device consist of a syringe with a spinneret, like a needle, a high voltage source, and a grounded collector plate, as shown in Figure 3.1 [53]. ES offers several advantages, making it a versatile and valuable technique that can be used for a wide range of applications from water and air filtration to biomedical applications such as tissue engineering and drug delivery [55, 56].

Besides its capacity to produce ultra-thin fibers with high surface area/volume, this technique allows different polymers to be used and to adjust their properties. This means that the manufacturers can tailor the fibers according to the desired application, meeting specific requirements, such as porosity, degradation rates, mechanical strength, and biocompatibility, by controlling the processing parameters or through additives. The setup used in this method has relatively simple components, allowing its use on a large scale. This low-cost method also allows relatively fast production of the desired structure [53, 57].

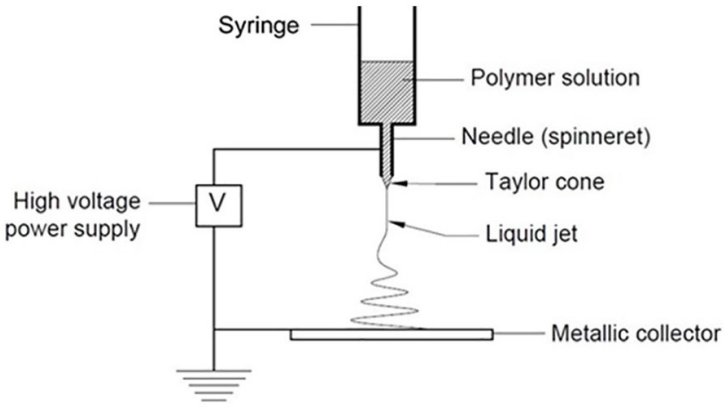


Figure 3.1: Schematic of the ES process [58].

3.1.1 Process

Initially, in the ES process, the syringe is filled with polymer solution. Then, a high voltage creates an electric field between the needle and the collector plate, causing the liquid drop to acquire a conical shape, the Taylor cone (Figure 3.2), at the tip of the needle. When the repulsive forces within the charged solution overcome the surface tension forces, the drop is deformed, and a thin jet is ejected from the cone to the collector. This stretches and aligns the molecules in the direction of the electrical field, attracting them to the collector and making it a continuous filament. With the solvent's evaporation, the fibers are produced and then solidify, forming a layer of ultra-fine solid material that can then be collected [59].

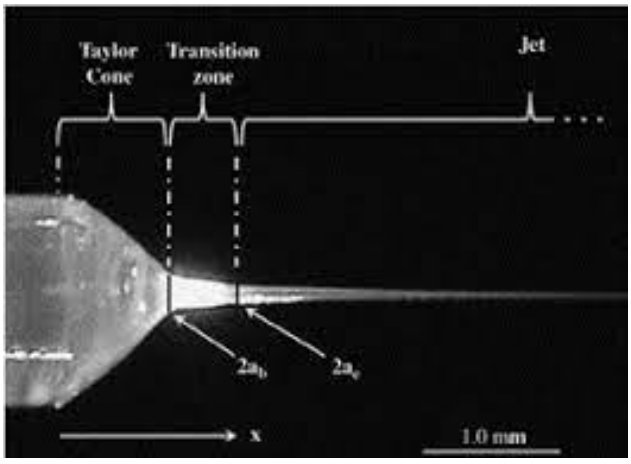


Figure 3.2: Formation of Taylor cone [60].

3.1.2 Solution Electrospinning and Melt Electrospinning

Solution Electrospinning (SES) is a variant of ES and is more commonly used and studied than MES. In this process, the polymer is first dissolved in an appropriate solvent and then loaded into a syringe connected to the spinneret. Then, an electric field is applied to the solution to induce

electrostatic forces and initiate the formation of nanofibers. These nanofibers then solidify through solvent evaporation, as represented in Figure 3.3 [53, 61].

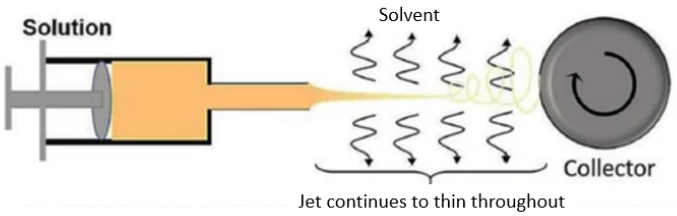


Figure 3.3: Schematic of the SES process (adapted from [62]).

Melt electrospinning (MES) is another ES variant that requires more complex equipment and high-temperature conditions. Besides the ES components shown in Figure 3.1, this technique's setup includes a higher spinning voltage and a heating device with a temperature sensor. This method works similarly to ES, but first, the polymer is heated to or above its melting point and loaded into the syringe connected to the spinneret. Then, an electric field is applied to the molten polymer to induce electrostatic forces. The polymer is stretched and elongated into fibers as it travels towards the collector. Finally, the fibers solidify after cooling [63]. A representation of this process can be seen in Figure 3.4. Since there is no evaporating solvent, the melted polymer will have higher viscosity and lower conductivity. This means that the fibers will have larger diameters in the micron range [64]. MES is used for processing thermoplastic polymers with dissolution difficulties that can be melted without degrading. It is also more adequate for large-scale production [63].

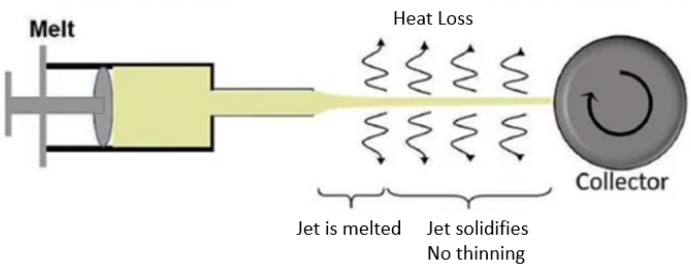


Figure 3.4: Schematic of the MES process (adapted from [62]).

Although ES can be performed with a wide range of materials, such as polymers, composites, small molecules, and colloidal particles, organic polymers are frequently used. In SES, the polymer is dissolved in a proper solvent like alcohols, dichloromethane, chloroform, dimethylformamide (DMF), tetrahydrofuran (THF), acetone, dimethyl sulfoxide (DMSO), hexafluoroisopropanol (HFIP), and trifluoroethanol. In MES, the polymers that are not easily dissolved are melted without suffering degradation. Some polymers used in these ES methods are present in Table 3.1 [53, 65]

Table 3.1: Examples of polymers used for SES and MES (adapted from [53]).

Solution Electrospinning	**Melt Electrospinning**
Polystyrene (PS), poly(vinyl chloride) (PVC), PCL, PLA, PLGA, DNA, silk fibroin, fibrinogens, dextran, chitin, chitosan, alginate, collagen, gelatin, polyaniline (PANi), polypyrrole (PPy), PVDF.	Polyethylene, PP, nylon-6, poly(methyl methacrylate) (PMMA), PET, PU, PCL, PLA, and PLGA).

3.2 Additive Manufacturing

3D printing is a process of additive manufacturing (AM) that uses a 3D printer to produce objects layer by layer. It allows the construction of models with geometries that were not possible with the conventional manufacturing processes [66]. The material can be printed through various techniques, including vat photopolymerization, material extrusion, material jetting, binder jetting, powder bed fusion, directed energy deposition, and sheet lamination [67].

One of the most common techniques of 3D printing is material extrusion, specifically fused filament fabrication (FFF). The principles of this technique are used in the melt electrospinning writing (MEW) technique, which will be discussed later. The FFF technique uses a continuous material filament to build a 3D object. A schematic of the FFF process can be seen in Figure 3.5. First, using rollers, the filament is fed through a heated nozzle, where it's melted to a semi-solid state. Then, it's extruded due to the pressure generated by these rollers. Finally, the material is deposited layer by layer onto the platform, where it must solidify completely. Subsequent layers can be produced: once a layer is finished printing, the printer's build plate moves down, and the movement is repeated until all layers are built [8, 68].

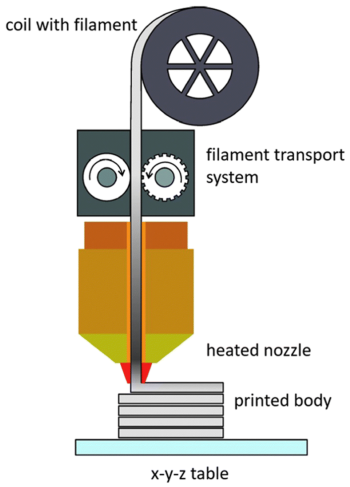


Figure 3.5: Schematic of the FFF process [69].

3.3 Melt Electrospinning Writing

Melt electrospinning writing (MEW) is a technique that joins electrospinning and additive manufacturing technologies, enabling the printing of complex 3D structures with high resolution at low cost from melted polymers. This relatively recent technique has mostly been studied for tissue engineering and biomedical applications. MEW makes it possible to build structures with mechanical strength at micrometer and nanometer diameter of range without solvents, avoiding toxicity, biodegradability, and biocompatibility issues. It allows to mimic the biological tissue's properties without compromising cellular growth and proliferation [51].

Figure 3.6 shows a scheme of typical MEW equipment. Its main components are a high voltage source, a movable collecting plate that allows a controlled fiber placement, a heating system, and an air supply or pneumatically regulated melt feeding system that causes the material extrusion through the spinneret [70].

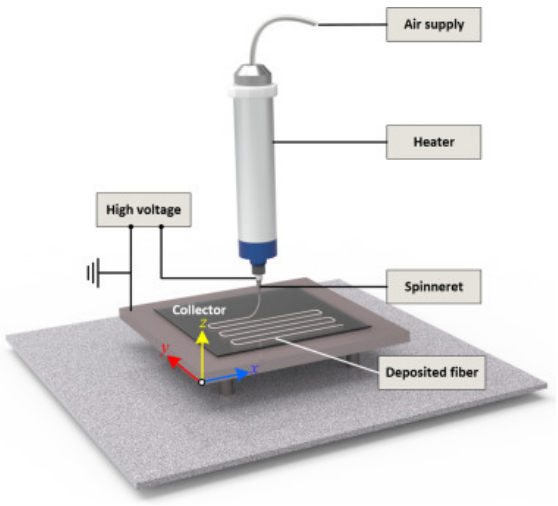


Figure 3.6: Schematic of a MEW device [71].

3.3.1 Process

The process starts by filling a print head with a thermoplastic polymer. This print head includes a heating system that melts the polymer, delivering it to the spinneret. Air pressure causes the material to extrude through the nozzle. The material is then subjected to an electric field generated between the spinneret and the collector from the high-voltage source. The electric field makes the material at the tip of the nozzle acquire a conical shape, the Taylor cone. Then, a small filament is formed at the end of this cone, developing into a fiber that is drawn toward the collector. This allows the ejection of a thin continuous jet with low flow rates, stretching the fibers. The formed ultra-fine fibers are deposited and solidify on the collector through cooling, forming a 3D structure. This structure can have several layers [72]. A Geometric code (G-code) file provides the parameters of the machine and the printing, such as the fiber's design and temperature.

3.3.2 Parameters

Several parameters will determine the quality of the printed structures during the MEW process. These can be material or process parameters [8].

Concerning the material parameters, these are:

- Molecular weight, melt flow rate, and viscosity: A higher molecular weight means more viscosity, which makes the material flow less easily, leading to a lower melt flow rate. Most materials used in MEW have high viscosity. Heating the material can reduce its viscosity, but it may undergo thermal degradation at a certain temperature. Materials with lower viscosity are typically not used in MEW due to the risk of the jet breaking in the presence of electrical forces [71].
- Electrical conductivity: The material must have low conductivity to maintain the stability of the electric field between the collector and the spinneret [72].

Regarding the process parameters, some are:

- Temperature: The materials used in MEW are subjected to temperatures above their crystalline melting point, reducing the material's viscosity and producing fibers with lower diameters. This favors the process; however, if the temperature is too high, the material undergoes thermal degradation, which compromises the jet [72].
- High voltage: This parameter is very important as it allows obtaining fibers with a very small diameter. However, the electric field strengthens if the high voltage is too high. This will result in a high filament extrusion speed, which means that more material will be in the Taylor cone, resulting in fibers with high diameters [73].
- Flow rate: An increase in the flow rate of the extracted material leads to lower stretching forces, also affecting the jet speed. This can increase the produced fiber diameter and vice versa. However, decreasing the flow too much can affect the formation of the Taylor cone [74].
- Collection speed: If the used speed is higher than the critical translation speed, straight-line fibers will be produced, or else the obtained will be curled. However, the collector's speed should not be too fast to maintain precision in the process [75].
- Tip-collector distance: The greater the distance between the spinneret and the collector plate, the weaker the electric field between them, leading to a smaller fiber diameter. Also, if the jet travels a greater distance to the collector plate, the fibers will solidify faster, compromising the fibers' adhesion and the 3D structure itself [74].

This technique can be applied in various areas, standing out as particularly relevant for biomedical applications. In the POP context particularly, MEW has already been studied as a method of

producing biocompatible and biodegradable meshes. In a study conducted in 2022, PCL mesh filaments were printed with different filament diameters and layers. The mechanical properties of the printed filaments were compared with the PP Restorelle® mesh and vaginal tissue's mechanical properties. The authors concluded that the PCL printed meshes presented biomechanical properties closest to the ones of the vaginal tissues than the Restorelle® mesh [8]. MEW has also proven to be effective in producing 3D-printed implants with incorporated antimicrobial agents to prevent infections associated with medical devices [76].

Chapter 4

Infection: predisposing factors and treatment

The following chapter presents considerations regarding pelvic mesh infection and predisposing factors. First, a literature review of the pathogens related to these infections, their adhesion, and biofilm formation is presented. Then, the treatment and prevention of these infections are addressed. More specifically, studies about using antimicrobial agent-incorporated meshes, such as gentamicin, azithromycin, and ciprofloxacin, and applications of polymer processing techniques to produce POP meshes to prevent and treat mesh-related infections, are mentioned.

4.1 Mesh-related Infection: Pathogens

Mesh-related infections are relatively rare but serious complications that can occur after pelvic floor repair. These have been reported to occur in up to 8% of all cases, leading to significant discomfort for patients and may even require the removal of the mesh implant [5]. While mesh infection is considered asymptomatic, it can interfere with the successful integration of the mesh into host tissues, leading to mesh exposure in some cases [5].

Studies reported that 77% of the tested vaginal meshes explanted due to pain, mesh erosion, mesh infection, and recurrent urinary tract infection (UTI) presented pathogenic bacterial content. Additionally, 31% of these meshes presented positive cultures with multiple pathogenic strains [5, 77].

The most commonly found organisms in infected pelvic meshes are gram-positive, gram-negative, anaerobic bacteria, and fungal microorganisms [78]. Previous research studies have found that *Escherichia coli* (*E. coli*) and *Staphylococcus aureus* (*S. aureus*) are among the most commonly found bacteria in infected biomaterial [79].

Staphylococcus aureus is a gram-positive bacterium that can lead to a variety of community and hospital-acquired infections [80]. *S. aureus* infections can be particularly challenging because the bacteria often develop antibiotic resistance. *Methicillin-resistant Staphylococcus aureus (MRSA)* strains are especially concerning because they are associated with higher mortality rates

and longer hospital stays compared to strains that are sensitive to methicillin (*MSSA*) [81, 82]. A study conducted in 2018 revealed that *S. aureus* was the most common pathogen in infected vaginal meshes, present in at least 80% of cases, followed by *E. coli*, *Enterococcus*, and *Candida*. It was also noted that of the isolated *S. aureus*, most were resistant to methicillin [5].

E. coli is the most common type of gram-negative bacteria. While it is typically harmless in the human gastrointestinal tract, it can lead to infections such as UTI, pneumonia, and peritonitis when outside the intestinal tract. Besides being part of the intestinal microbiota, it is often found on the floors of healthcare facilities [83]. Apart from often being present in infected biomaterials, *E. coli* was found in 12% of POP or SUI meshes removed due to complications such as vaginal erosion [79].

4.2 Predisposing Factors for Infection

Pelvic mesh infection may occur due to several factors, including the characteristics of the mesh itself, such as its material or pore size, which can make the mesh more susceptible to bacterial colonization or affect its biocompatibility. The human body may also react to the mesh as a foreign object, leading to inflammation and potential infection [84]. The surgical technique can also allow bacteria to enter the surgical site and contaminate the mesh. Bacteria can also adhere to the surface of the mesh and form biofilms, making infections difficult to treat. Certain patient characteristics, such as age, obesity, or diabetes, may increase the risk of infection [5].

The vaginal microbiome is crucial for maintaining vaginal health and preventing the growth of harmful microorganisms. Variations in the composition and diversity of the vaginal microbiota can make individuals more susceptible to pelvic mesh infection after their implantation. A healthy vaginal microbiome is primarily populated by *Lactobacillus* bacteria, which help maintain an acidic environment and provide protection against pathogens [85].

Although POP treatment, such as pessary usage or reconstructive surgery, leads to symptom improvement, it can also disrupt the vaginal microbiome. Studies have shown that patients with pessary-related erosions had higher bacterial diversity, increased gram-negative bacteria, and decreased *Lactobacillus*. An imbalanced vaginal microbiome, such as low *Lactobacillus* abundance, high diversity of anaerobic species, or pre-existing vaginal infections may also increase the risk of mesh infection [85].

4.3 Adhesion and Biofilm Formation

Infection is caused by a microorganism invasion, disrupting normal bodily functions. Depending on the pathogen and affected system, different symptoms may appear. These symptoms are caused by the body's immune system's attempt to eliminate these invading organisms, which can be viruses, bacteria, fungi, or parasites [86]. When biomaterials are implanted in the human body,

they come into contact with the surrounding tissues and may come in contact with microorganisms. These microorganisms may be pathogenic and adhere to the surface of the material, causing the formation of a biofilm that further leads to infection.

There are three main stages in the formation of biofilms, as displayed in Figure 4.1 [87, 88]:

- Attachment: During this phase, the pathogen attaches to the biomaterial's surface via Van der Waals forces, hydrophobic, and electrostatic interactions. This phase depends on the surface of the biomaterial. At this point, the adhesion is still reversible, but when the attraction force between the pathogen cells and the implant surface becomes greater than the repulsive force, an irreversible adhesion is formed.
- Maturation: Following the attachment, the pathogen proliferates and forms microcolonies after the pathogen becomes well adhered. These microorganisms then produce and release extracellular polymeric substances (EPS), like proteins and polysaccharides, that surround and encapsulate the pathogenic cells within the biofilm, forming a complex structure. This structure shields the pathogen from threats, being able to cause a reduced host's immune response and resistance to antimicrobial agents due to its complexity.
- Dispersion: Finally, in this stage, the pathogen disperses by detaching from the biofilm, returning to the initial planktonic state. The microorganism in this initial state can spread to other regions, restarting the biofilm formation cycle in those regions and spreading the infection.

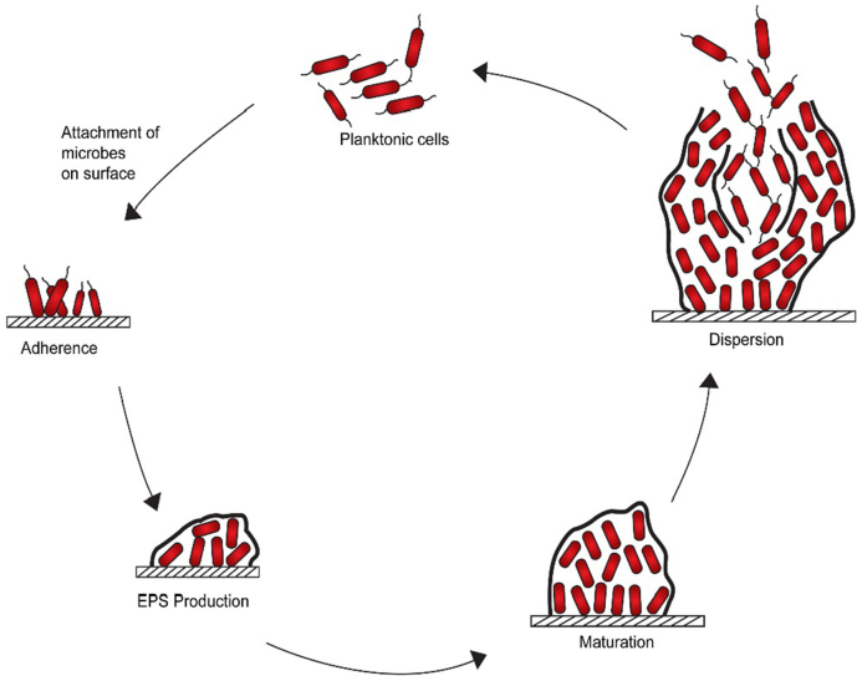


Figure 4.1: Schematic representation of biofilm formation [88].

4.4 Treatment and Prevention of Infection

The biofilm structure formed during infection can make bacteria more resistant to various antibiotics. When an infection develops in implanted biomaterial, and antibiotics cannot treat it, removing the implanted device may become necessary to prevent the infection from spreading [89]. That is the case with pelvic mesh-related infections. Consequently, removing the mesh can lead to several complications, such as tissue injury, as well as the return of the symptoms that initially led to its insertion, once again negatively impacting the quality of life of women. For this reason, it is of extreme importance to study measures to prevent infection in these mesh implants [5, 90].

The treatment of mesh-related infections in women who have undergone pelvic organ reconstruction involves a combination of surgical and medical approaches. It includes the application of topical estrogen cream and the administration of intravenous or oral antibiotics. Surgical treatment of vaginal mesh-related infections in female pelvic surgery involves draining any abscesses and partial or full removal of the vaginal mesh [78].

Various preventive measures have been taken to prevent mesh infection. It is believed that meshes with a pore size of over 75 μm can reduce the risk of infection. This is because they allow certain types of white blood cells, macrophages, and fibroblasts to pass through the mesh in case of infection. Additionally, lighter and softer meshes are expected to prevent mesh infection as they involve less implanted material and have a lower chance of becoming infected [78].

Azithromycin (Figure 4.2) is a broad-spectrum antibiotic effective against both gram-positive and gram-negative susceptible bacteria [91]. It is indicated for mild to moderate infections. Besides targeting various amounts of pathogens, it is FDA-approved for treating pelvic infections [92]. This antibiotic is a member of the macrolide antibiotic class and targets the bacteria's ribosomes, preventing protein synthesis and ultimately eliminating the infection [93]. Studies have also shown its effectiveness in inhibiting the growth of *S. aureus* bacteria when used in 3D printing of meshes with antibacterial properties [10].

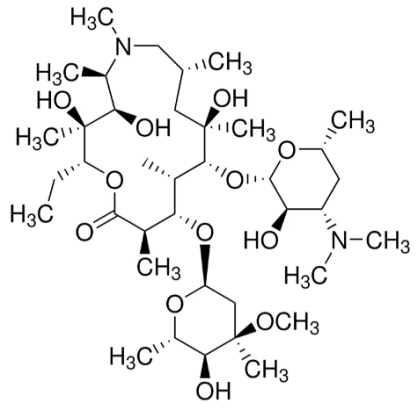


Figure 4.2: Chemical structure of azithromycin [93].

Gentamicin Sulfate (4.3) is an aminoglycoside antibiotic that inhibits the growth of certain bacteria, including both gram-positive and gram-negative bacteria, such as *S. aureus* and *S. epidermidis* [94, 95]. This is achieved by disrupting the protein synthesis in bacteria by binding to the 30S ribosomal subunit, which blocks the translocation of peptidyl-tRNA, preventing the accurate decoding of genetic information. This leads to the production of defective proteins, ultimately killing the bacteria [96]. In addition to treating skin conditions or infections, UTIs, and pelvic inflammatory disease, gentamicin has also been studied for applications in the field of 3D printing [97, 98]. Recent studies have used gentamicin to coat 3D-printed implants to prevent post-surgical infections in bone fractures [99], as well as in the manufacture of catheters used for drug delivery [100]. Gentamicin has also proved to be effective against *E. coli* in 3D-printed antibiotic-loaded meshes for infection prevention in hernia repair [11].

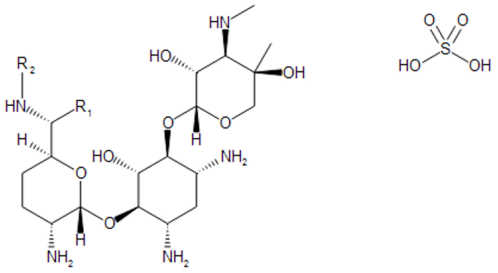


Figure 4.3: Chemical structure of gentamicin sulfate [101].

Ciprofloxacin (Figure 4.4) is also a broad-spectrum antibiotic with activity against both gram-positive and gram-negative bacteria. It belongs to the quinolone class of antibiotics and works by inhibiting DNA synthesis. This drug is commonly used for severe abdominal or UTI, and has shown to be capable of destroying biofilms [102]. Additionally, ciprofloxacin has been studied in other medical applications, such as in 3D printed meshes for hernia repair, where it has been found to reduce adhesions and inflammation [12].

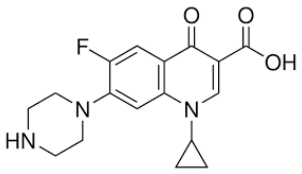


Figure 4.4: Chemical structure of ciprofloxacin [103].

Considering that infection is a prevalent factor in surgical pelvic mesh failure, the integration of antibiotics into meshes produced by polymer processing techniques has been attracting the attention of investigators. In these studies, the antibiotics were incorporated into the meshes through different processes, either by coating the mesh after printing or by mixing the antibiotic directly with the polymer and then printing them together. However, it was observed that the effectiveness of the antibiotics may be reduced when they are mixed with the polymer and printed, possibly due to the high printing temperature [76].

Incorporation of ciprofloxacin in PP and PVA meshes: Through 3D printing, this study explores the fabrication of hernia meshes with drug loading of ciprofloxacin, made from PP and PVA filaments. The printed meshes were characterized for mechanical properties, drug loading/release, and biocompatibility. In vivo testing in rabbits showed reduced adhesions and inflammation with the drug-loaded meshes. The results demonstrate that 3D printing is effective for developing tailored drug-loaded meshes for hernia management [12].

Integration of gentamicin in PCL meshes with calcium chloride and sodium alginate: In this study, 3D printed PCL meshes combined with alginate and the antibiotic gentamicin were evaluated for hernia repair applications. The meshes were tested in vitro against *E. coli* cultures and in vivo in a rat model. In vitro, meshes containing gentamicin showed inhibition zones against *E. coli*. The study demonstrated the potential for 3D printed, antibiotic-loaded meshes for infection prevention in hernia repair [11].

Chapter 5

Materials and Methods

This chapter discusses the materials, equipment, instruments, tools, and experimental procedures employed for 3D printing meshes, antibiotics incorporation, and their subsequent testing.

5.1 Materials

In this section, the materials used in the experimental work are approached. PCL was the polymer used to print the meshes that were further coated with antimicrobial agents, such as gentamicin sulfate, azithromycin, and ciprofloxacin. These antibiotics were chosen based on the literature as common drugs used in the genitourinary tract that have already been studied with polymer processing techniques [10, 12].

5.1.1 Technical-Grade PCL

PCL is a biodegradable polymer often used in ES processes, and it is approved by the FDA for medical use in humans. Besides its expected slow degradation of 2 to 3 years, this material is advantageous for MEW due to its low melting temperature and fast solidification [104].

This material, named Facilan™ PCL 100 (3D4Makers, The Netherlands), is a 1.75 mm diameter filament. It has a density of 1.1 g/cm^3 (ISO 1183), a melting point of 58 to 60 ºC, a glass transition temperature of - 60 ºC, a decomposition temperature of 200 ºC and a melt flow index of 11.3 to 5.2 g/10min [8].

5.1.2 Antibiotics

For this study, antibiotics were purchased from Sigma-Aldrich to coat the PCL meshes manufactured through MEW for POP treatment. To perform this incorporation, ciprofloxacin and gentamicin sulfate were diluted in distilled water, and azithromycin was diluted in pure ethanol.

5.1.3 Bacteria Strains

Bacterial strains were obtained from the American Type Culture Collection (ATCC, USA), namely *Escherichia coli* (*E. coli*) ATCC 25922, *Methicillin-susceptible Staphylococcus aureus* (*MSSA*) ATCC 29213, and *Methicillin-resistant Staphylococcus aureus* (*MRSA*) ATCC 43300. These bacteria were used to evaluate the efficiency of the antibiotics.

5.2 Instruments and Tools

Different instruments and tools were used to produce the meshes, to perform the mechanical tests, antimicrobial incorporation, and microbiological assays.

5.2.1 Mesh Production

The following instruments and tools were used to manufacture the meshes:

- **Melt Electrospinning Writing Prototype:** A MEW prototype developed during the "SPIN-MESH" project in 2021 was used to print the PCL meshes. The main components of this prototype are the structure, the linear actuators, the collector plate, the extruders, the graphic touch screen, and the high voltage generator that can be seen in Figure 5.1. Although this device allows printing through different extruders, only the filament extruder was used during this work. The precision of the movement is very important in this technique, being in Cartesian configuration. The collector's movement is guaranteed by linear actuators, resulting in movements in X and Y directions. In the Z direction, the movement occurs in the print head, allowing a maximum height of 70 mm. The spinneret is a conventional FFF nozzle, allowing the formation of the Taylor cone at its tip. The nozzle's orifice has a diameter of 400 μm, as well as the maximum fiber diameter. The high voltage source generates a 60 kV voltage, a 150 W power, and a minimum output current of 0.01 mA. The collector consists of a square aluminum plate with an area of 270x270 mm^2 and a thickness of 3 mm since aluminum is a material with high conductivity [8]. This prototype is available at the Product and Services Development Laboratory (LDPS), FEUP.

- **GCode designing software:** The FullControl GCode Designer software was used to design the meshes, obtaining the code to be sent to the MEW prototype. NC Viewer, a GCode Viewer, was used to obtain a preview of the meshes with the previously obtained GCode.

- **Optical microscope:** The Zeis Axiophot Microscope, a binocular optical microscope, was used to obtain images of the fibers and meshes produced to confirm their dimensions, along with the Olympus Stream micro-imaging software. This tool was available in the Materialography Laboratory at the Mechanical Engineering Department, FEUP.

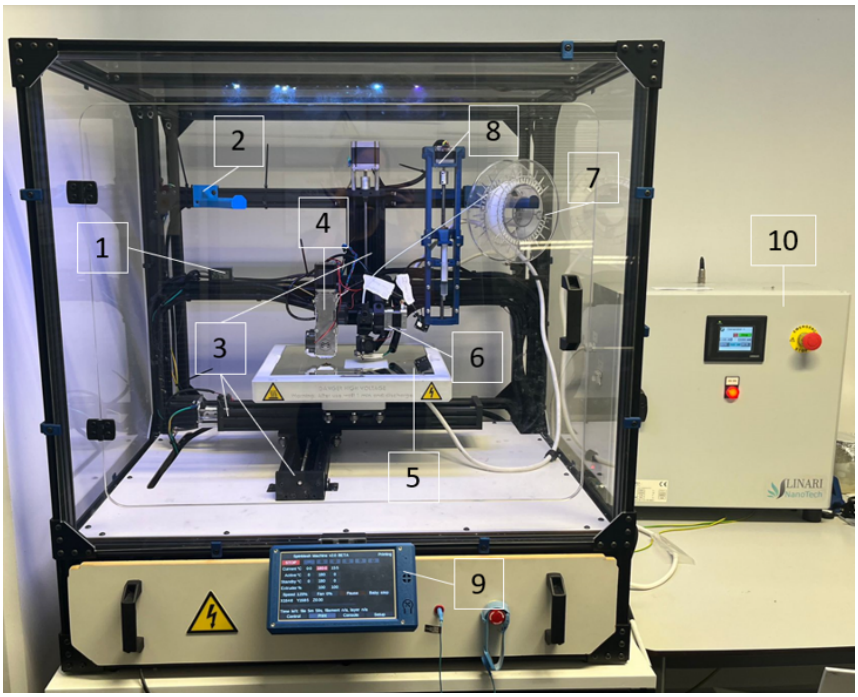


Figure 5.1: MEW prototype: 1) Digital thermometer and hygrometer; 2) Filament holder; 3) Linear actuators (X, Y, and Z directions); 4) Pellet extruder; 5) Collector plate; 6) Filament extruder; 7) Filament; 8) Syringe pump; 9) User interface; 10) High-voltage generator.

5.2.2 Mechanical Tests

The following tools, equipment, and instruments were used to perform the mechanical tests, more precisely, both the uniaxial tensile tests and the cyclic tests:

- **Mechanical Testing Machine:** The mechanical tests of the printed meshes were conducted on the Mecmesin Multitest 10-í (Mecmesin GmbH, Germany) along with the Emperor Force Testing System software. The machine was configured with a 500 N load cell at a 10 mm/min elongation rate. This device was available at the Biomechanics Laboratory, Institute of Science and Innovation in Mechanical and Industrial Engineering (INEGI) and can be seen in Figure 5.2.

- **Caliper:** This tool was used to measure the distance between the folds of the mechanical testing machine. It was also available at the Biomechanics Laboratory, INEGI.

5.2.3 Antimicrobial Incorporation and Evaluation

To perform the drug incorporation in the PCL meshes and to evaluate its effectiveness, the following instruments and tools were used:

- **Scale:** The antibiotics were weighed using the AX623 Sartorius M-pact Series electrical scale. This scale was available at the Biomechanics Laboratory, INEGI.

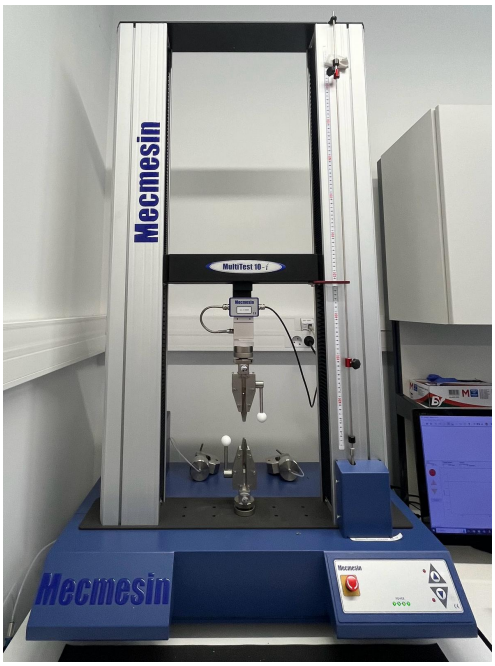


Figure 5.2: Mechanical Testing Machine.

- **Magnetic Stirrer:** This tool was used to dissolve the antibiotics into the solvents and was available at Biomechanics Laboratory, INEGI.
- **Laminar Flow Cabinet:** The Thermo Scientific MSC-Advantage Class II biological safety cabinet (Thermo Fisher Scientific, USA) was also available at Biomechanics Laboratory, INEGI. It was used to sterilize the samples and material under UV-C light and to ensure a sterile environment during the experimental procedure.
- **Fourier-transform infrared (FTIR) Spectrometer:** The Agilent Cary 360 FTIR Spectrometer (Agilent Technologies, USA) with a diamond attenuated total reflectance (ATR) accessory was used to evaluate the composition of the meshes; this is, to ensure the antibiotics incorporation. This technique uses infrared light to characterize a material's chemical composition by analyzing FTIR peaks specific to chemical bonds or functional groups, obtaining a spectrum fingerprint of the compound [105]. Spectra were acquired with a resolution of 4 cm^{-1}, with wavelengths from 900 to 4000 cm^{-1}. This device can be seen in 5.3 and was available in the Tribology Laboratory, FEUP.

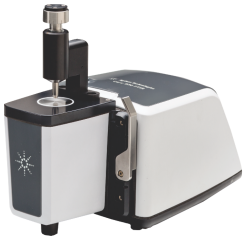


Figure 5.3: Agilent Cary 360 FTIR Spectrometer [106].

5.2.4 Microbiological Assays

During the microbiological assays, the following tools and devices were used:

- **Orbital Shaker:** This device was used to culture the bacterial strains overnight, configured for 120 rpm and 37ºC. The orbital shaker was available in the Microbiology Laboratory at the Pathology Department, FMUP.
- **Laminar Flow Cabinet:** The FASTER BH-EN 2004-S equipped with a UV-C light was used to sterilize the samples before the microbiological assays. This device was available in the Microbiology Laboratory at the Pathology Department, FMUP.
- **Densiometer:** The BioMerieux DensiCHEK Plus Densitometer was used to adjust the bacterial concentration to 0.5 McFarland (MCF). This tool was available in the Microbiology Laboratory at the Pathology Department, FMUP.
- **Incubator:** The incubator available in the Microbiology Laboratory at the Pathology Department at FMUP was used to incubate the cultures.
- **Spectrophotometer:** The SHIMADZU UV-160A spectrophotometer was used to obtain absorbance values regarding the biofilm formation in the mesh samples. This device was available in the Microbiology Laboratory at the Pathology Department, FMUP.
- **Scanning Electron Microscope (SEM):** SEM analyses were carried out to study the presence of bacteria on the meshes coated with antibiotics. These analysis were carried out using a High-resolution (Schottky) Environmental Scanning Electron Microscope with X-ray microanalysis and Electron Backscattered Diffraction analysis: FEI Quanta 400 FEG ESEM / EDAX Genesis X4M. To perform this analysis, the samples were coated by sputtering with an Au/Pd thin film using the SPI Module Sputter Coater equipment. Images were obtained for 80x, 500x, 4000x, and 13000x ampliations. These equipments were available at the Materials Centre of the University of Porto (CEMUP).

5.2.5 Statistical Analysis

To evaluate the collected data in the biofilm formation assays, a statistical analysis with a 95% confidence level was performed in Microsoft Excel 365, version 2405. A t-test with independent samples was performed to determine the statistical significance of each result, comparing the means of meshes with only bacterial content (positive control) and each of the antibiotic-coated meshes with bacterial strains. The results were found statistically significant for p values < 0.05.

5.3 Experimental Procedures

The overall process of the developed work can be seen in Figure 5.4. Explaining the process briefly, the first step consisted of printing 160 and 240 μm diameter meshes with pore sizes of

both 1 and 1.5 mm. To obtain these meshes, first, the process parameters of the MEW prototype shown in Figure 5.1 were adjusted to optimize the production of the PCL meshes. Using these parameters, the meshes were printed according to the desired characteristics. Afterwards, the process was divided into two independent phases. In the first phase, mechanical tests were performed to evaluate the meshes' mechanical properties, more precisely, uniaxial tensile tests and cyclic tests. In the other route, the printed meshes were coated with antibiotics, and their incorporation was evaluated through FTIR spectroscopy. The next step consisted of performing microbiological assays, specifically zone inhibition and biofilm formation assays, to investigate the antimicrobial activity of the meshes against bacterial strains and their effect on biofilm dynamics. SEM images were also obtained to study the morphology of the meshes and microorganisms' presence after the antibiotic incorporation in the meshes. These stages will be explained in greater detail in the following sections.

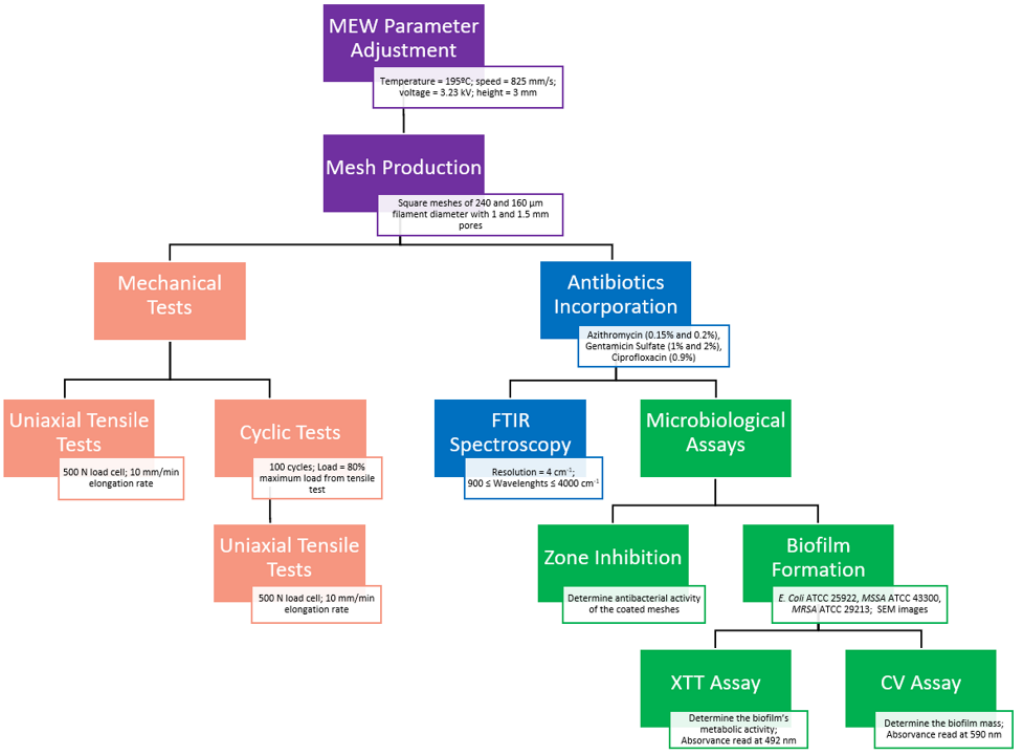


Figure 5.4: Experimental procedures performed, their main characteristics or objective.

5.3.1 Mesh Production and Characteristics

The first step of the experimental work consisted of writing the G-code files to print meshes with the desired characteristics using FullControl GCode Designer software and NC Viewer. These files consist of instructions, where each line typically represents a specific operation followed by Cartesian coordinates. These indicate the required movement of the machine's nozzle to print the desired structure.

The FullControl software allows the entrance of several parameters, such as pore size, fiber diameter, mesh size, extrusion temperature, print speed, and mesh geometry. The characteristics of the meshes to be printed were inserted, specifically, square-shaped geometry with 160 μm and 240 μm fiber diameter of two different pore sizes: 1 and 1.5 mm, as shown in Table 5.1. The chosen dimension of the meshes was 84x84mm. The square mesh geometry was chosen based on its similarity to a commercially available mesh [51]. The used fiber diameters were selected following previous studies [107].

Table 5.1: Characteristics of PCL meshes.

Geometry	Filament Diameter	Pore Size (mm)
Square-shaped	240 μm	1.5
		1
	160 μm	1.5
		1

The fiber diameter is related to the extrusion rate inserted in the G-code. This rate is the amount of material that gets extruded to form fibers of a certain diameter. The extrusion rate is calculated by the following Equation 5.1:

$$E = \frac{(D_{\text{Fiber}}^2 \cdot l_{\text{Fiber}})}{D_{\text{Filament}}^2} \tag{5.1}$$

Where:

D_{Fiber} - Fiber diameter;

l_{Fiber} - Length of the printed segment;

D_{Filament} - Filament diameter of 1.75 mm.

To be able to print the meshes with the correct dimensions, the printing parameters of the MEW prototype had to be adjusted. The process parameters used to print the meshes are listed in Table 5.2. These parameters proved to be the ones that provided diameter and porosity values closest to the desired ones. These dimensions of the meshes were assessed under the optical microscope. The chosen parameters allowed printing with a stable continuous filament, without elongation, with only minor errors. All of these parameters were defined in the code files except the voltage, which involved manually turning on the voltage supply and inserting the desired value.

Using the mentioned parameters and the written G-code files, square meshes with 240 μm and 160 μm fiber diameters were printed with both 1.5 mm and 1 mm pores.

Table 5.2: Process parameters used in the MEW prototype for printing the 240 and 160 μm meshes.

Parameter	Value
Temperature	195 ºC
Voltage	3.23 kV
Speed	825 mm/min
Height	3 mm

5.3.2 Mechanical Tests

Using the equipment shown previously in Figure 5.2, uniaxial tensile tests were performed on 50x10mm samples of the printed PCL meshes using a 500 N load cell and a constant 10 mm/min elongation rate. A scheme of the uniaxial tensile test and the applied load can be seen in Figure 5.5. The samples of the meshes were placed on the equipment, and a preload of 0.1 N was applied to avoid slack before starting the test. The distance between the mechanical folds was also measured.

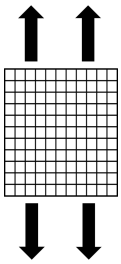


Figure 5.5: Scheme of the applied load during uniaxial tensile test.

Force-displacement data was acquired for three samples of each category, which allowed obtaining average stress-strain curves through Equations 5.2 and 5.3. The calculated stress was apparent since the area was considered equal to the diameter of the filament (since the meshes are only composed of 1 layer) multiplied by the width of the sample (10 mm).

$$\text{Stress: } \sigma = \frac{F}{A} \tag{5.2}$$

Where:

σ - Stress [MPa];
F - Force [N];
A - Area [mm^2].

$$\text{Strain: } \varepsilon = \frac{\Delta L}{L_0} \tag{5.3}$$

Where:

ε - Strain;
ΔL - Displacement [mm];
L_0 - Initial length [mm] (distance between the mechanical folds before the test).

Young's modulus (E), or elastic modulus, is a mechanical property of a material that determines its resistance to mechanical load in the elastic region and, therefore, the material's stiffness. It is defined as the ratio between the applied stress and the deformation it undergoes in the linear elastic region of a material. The Young's modulus was calculated using Equation 5.4 and is usually expressed in megapascals (MPa) [75].

$$\text{Young's Modulus: } E = \frac{\sigma}{\varepsilon} \tag{5.4}$$

After the tensile tests, cyclic tests were performed to evaluate the behavior of the meshes when subjected to cyclic loading conditions. Using the same equipment as the previous test (Figure 5.2) and a 10 mm/min elongation rate, the samples were continuously compressed and distended for 100 cycles [108], as shown in Figure 5.6. 80% of the maximum load reached that caused sample rupture in the uniaxial tensile tests was inserted into the machine software to perform the cyclic tests, as described in previous studies [109].

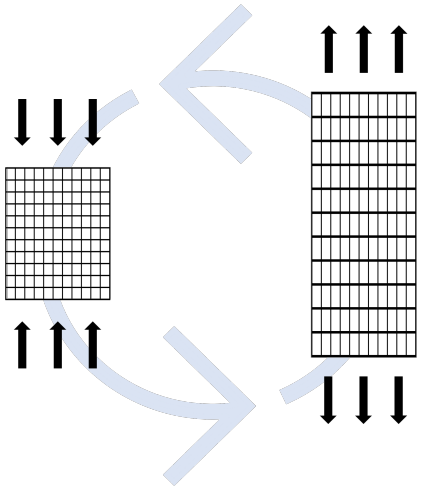


Figure 5.6: Scheme of the applied load during cyclic tests.

After the cyclic tests, the samples were stored and subjected to uniaxial tensile testing to evaluate the meshes' performance after cyclic loading conditions and how these altered the strain-stress curves obtained previously [90].

5.3.3 Antimicrobial Incorporation and Evaluation

The antimicrobial incorporation was performed by coating the meshes with the desired antibiotics rather than incorporating drugs directly into the filament before its extrusion. This approach was chosen based on previous studies, which proved that the high 3D printing temperatures affect drug incorporation and, therefore, antimicrobial activity [76].

First, to initiate the meshes' coating with the chosen drugs, they were cut into 1 cm^2 samples using surgical scissors and gloves to avoid possible contamination. Meshes with a diameter of 240

μm and 1.5 mm pore size were selected for use in the drug incorporation phase of the experimental work owing to their thicker composition, facilitating manipulation during sample preparation.

The samples and the necessary material were sterilized for 30 min under UV-C light in the laminated flow cabinet. Then, the samples were immersed for 24h in the previously prepared solutions of the antibiotics, obtaining meshes with the following concentrations of antibiotics:

- Azithromycin: 0.15% (w/w) and 0.20% (w/w), using pure ethanol as the solvent.
- Gentamicin Sulfate: 1% (w/w) and 2% (w/w), using distilled water as a solvent.
- Ciprofloxacin: 0.9% (w/w), using distilled water as a solvent.

The antibiotic concentrations were chosen to see if the drugs had an effect when in different concentrations than the ones previously tested in different studies [10, 100, 110].

Mesh samples were also immersed in distilled water and pure ethanol to analyze if the solvents interfered with the material or the antibiotic.

After 24 hours, the samples were removed from the solutions and placed apart in Petri dishes. They were then left to air-dry for another 24 hours in the laminated flow cabinet.

FTIR spectroscopy analysis was performed to evaluate the drug incorporation in the meshes. The FTIR spectra were obtained for the 8 types of mesh samples: PCL (control), pure ethanol, distilled water, ciprofloxacin 0.9%, gentamicin sulfate 1%, gentamicin sulfate 2%, azithromycin 0.15% and azithromycin 0.2%.

5.3.4 Zone Inhibition Assays

The antimicrobial activity of the meshes was determined using the agar diffusion assay against the previously mentioned bacteria strains: *Escherichia coli* (*E. coli*) ATCC 25922, *Methicillin-susceptible Staphylococcus aureus* (*MSSA*) ATCC 29213, and *Methicillin-resistant Staphylococcus aureus* (*MRSA*) ATCC 43300.

These bacteria were cultured in Brain Heart infusion broth (BH) overnight in an orbital shaker at 37 °C and 120 rpm. The bacterial culture was then centrifuged at 9000 rpm for 5 minutes at 22ºC. Then, the bacterial concentration was adjusted to 0.5 McFarland standard, which corresponds to approximately 1.5×10^8 CFU/mL [111]. This suspension was smeared in triplicate on Mueller-Hinton agar plates. The 1 cm^2 drug-loaded and unloaded mesh samples were sterilized for 30 min on each side under UV-C and were then placed in the plates containing the previously mentioned bacterial strains, which were incubated for 24h at 37ºC.

The antibacterial activity of the coated mesh samples was determined by measuring the diameter of the inhibition zone after 24 and 48 hours of incubation, using the PCL samples as a control.

5.3.5 Biofilm Formation Assays

The previous process of bacteria culture detailed in Subsection 5.3.4 was repeated for the three bacterial strains. After adjusting the bacterial concentration to 0.5 McFarland, the suspensions were diluted to 1:10 in Brain Heart infusion broth (BH). The meshes were plated in 12-well plates, and 1 mL of the bacterial suspension was added per well. The plates were then incubated for 24 hours at 37ºC under static conditions.

XTT (tetrazolium salt) and Crystal Violet (CV) assays were performed to obtain insight into how the incorporated drugs affect the metabolic activity of the biofilm and their impact on biofilm formation and biomass, respectively.

In the XTT assay, the supernatant was first removed, and the samples were washed three times in Phosphate-buffered saline (PBS). Two mL of XTT solution was added to each plate well with mesh samples. The plates were then incubated in the dark with agitation. After 3 hours of incubation, the optical density (OD) of the solution the mesh samples were immersed in was measured in the spectrophotometer at 492 nm in triplicate, using the negative control (PCL meshes) as the baseline.

For the crystal violet (CV) assay, the samples were washed three times in PBS, and 0.5 mL of methanol was added to each well. After 30 minutes of incubation, the liquid was removed, and the remaining methanol was left to evaporate for 30 minutes at room temperature. Then, 1 mL of CV 0.5% was added and incubated for 20 min. After removing the CV, the samples were washed three times with 1.5 mL of water. Next, 1.5 mL of acetic acid 33% (v/v) was added and left to rest for 15 min. Finally, the OD of the solution the mesh samples were immersed in was registered at 590 nm in triplicate, using the negative control as the baseline.

The optical density of the positive control ($OD_{Control}$) in both assays allowed the classification of the biofilm formation according to the three categories [112, 113].

In the XTT assay, the biofilms were classified according to metabolic activity intensity:

- High metabolic activity: $OD_{Sample} \geq 75\%\ OD_{Control}$;
- Moderate metabolic activity: $25\%\ OD_{Control} \leq OD_{Sample} < 75\%\ OD_{Control}$;
- Weak metabolic activity: $OD_{Sample} < 25\%\ OD_{Control}$.

In the CV assay, biofilm formation was classified by concentration of biofilm cells:

- Strong biofilm producer: $OD_{Sample} \geq 75\%\ OD_{Control}$;
- Moderate biofilm producer: $25\%\ OD_{Control} \leq OD_{Sample} < 75\%\ OD_{Control}$;
- Weak biofilm producer: $OD_{Sample} < 25\%\ OD_{Control}$.

A percentage of reduction in biofilm biomass and its metabolic activity was calculated through Equation 5.5.

$$\%\ \text{Reduction} = \left(1 - \frac{OD_{Sample}}{OD_{Control}}\right) \times 100 \tag{5.5}$$

Chapter 6

Mechanical Tests Results

In this chapter, the results obtained in the mechanical tests are approached and discussed. Initially, uniaxial tensile tests were performed. During these tests, force-displacement data was gathered, obtaining stress-strain curves. This allowed the determination of the maximum stress that the samples could withstand to be applied in the cyclic tests. In the cyclic tests, the long-term behavior of the meshes was evaluated throughout various cycles, continuously compressing and distending the samples. After the cyclic tests, the samples were subjected to uniaxial tensile tests to evaluate the effect of cyclic loading conditions on the material's mechanical properties.

6.1 Uniaxial Tensile Tests

From the acquired force-displacement data, average stress-strain curves were obtained. The stress-strain curves for printed square meshes with fiber diameters of 160 and 240 μm and pore sizes of 1 and 1.5 mm are presented in Figure 6.1. A curve of the expected 160 μm mesh with 1.5 mm pore behavior is also presented. This graph encompasses the stress-strain curve for Restorelle®, a commercial mesh [109], as well as curves derived from anterior and posterior prolapsed vaginal human tissue [114].

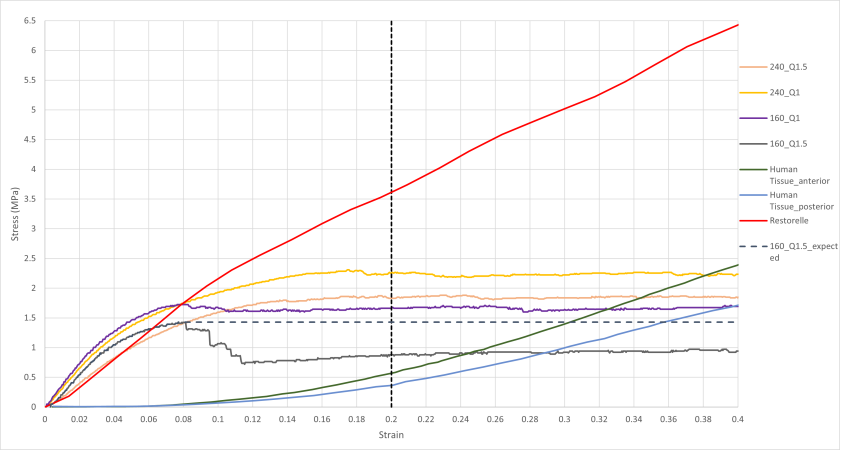


Figure 6.1: Stress-strain curves obtained through uniaxial tensile testing.

The graph displays results for the comfort and safety zones. The comfort zone represents the typical stresses experienced during everyday activities, usually within a range of up to 20% strains. On the other hand, the safety zone accommodates extreme stress peaks, up to a 40% strain [115].

The PCL meshes exhibit similar behavior; however, they differ both from the commercial mesh and the human vaginal tissue. While the samples present a plastic behavior [75], the vaginal tissue presents a hyperelastic behavior [116].

Although the meshes behave similarly, they reach different maximum stresses, presented in Table 6.1. The stresses obtained for the 240 μm diameter meshes are higher than those of the 160 μm diameter meshes. In addition, the meshes with a 1 mm pore size reach a higher stress value than the 1.5 mm pore meshes.

Table 6.1: Maximum stress values obtained in the comfort zone from the stress-strain curves.

Filament Diameter (μm)	**Pore Size (mm)**	σ_{max} **(MPa)**
240	1.5	1.88
	1	2.31
160	1.5	1.43
	1	1.74

In Table 6.2 are the stress values obtained for 20% strain that limits the comfort zone for posterior prolapsed human tissue, anterior prolapsed human tissue, and the commercial mesh.

Table 6.2: Human prolapsed vaginal tissue and Restorelle® maximum stress values in the comfort zone obtained from the literature [109, 114].

	$\sigma_{(\varepsilon=20\%)}$ **(MPa)**
Restorelle®	3.62
Anterior Human Tissue	0.56
Posterior Human Tissue	0.36

6.2 Cyclic Tests

The cyclic tests were performed for 100 cycles using a load-control method. In these tests, the maximum load the samples were subjected to was defined as 80% of the average load the samples could withstand in the uniaxial tensile tests. Figure 6.2 depicts the results of one sample representative of each tested group, namely 160 and 240 μm filament, and pore sizes of 1 and 1.5 mm. The obtained graphs show that the samples withstand the loads they are subjected to for 100 cycles without major failure.

The variation of strain ($\Delta\varepsilon$) in the sample can be obtained by calculating the difference between the 100th cycle strain and the strain for the 1st cycle at the maximum stress. In Table 6.3 are the obtained strain variation averages for each mesh type.

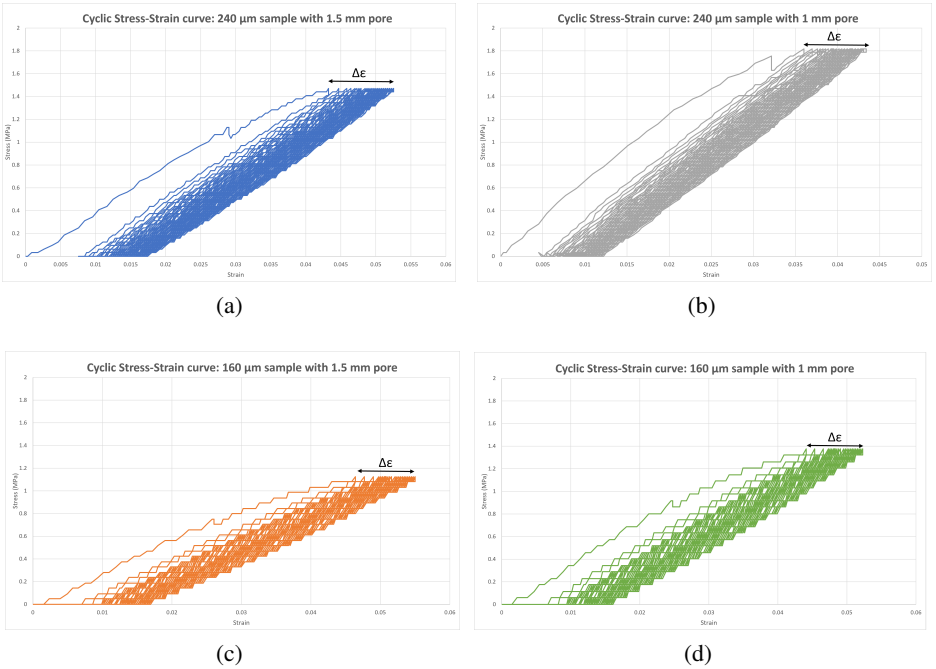


Figure 6.2: Stress-strain curve obtained from cyclic tests of (a) 240 μm samples with 1.5 mm pores; (b) 240 μm samples with 1 mm pores; (c) 160 μm samples with 1.5 mm pores; (d) 160 μm samples with 1 mm pores

Table 6.3: Average strain variation calculated between the 1st and 100th in the cyclic tests.

Filament Diameter (μm)	**Pore Size (mm)**	σ_{max} **(MPa)**	$\Delta\varepsilon$ **(%)**
240	1.5	1.47	1.79
	1	1.82	0.73
160	1.5	1.13	0.95
	1	1.38	0.79

Figure 6.3 shows the deformation caused by each of the 100 cycles in a 240 μm mesh with 1 mm pores. A logarithmic trend line can be fitted into the strain points which can predict the fatigue conditions of the mesh.

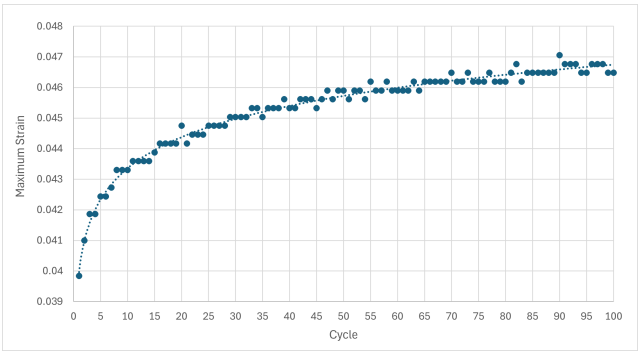


Figure 6.3: Strain suffered at maximum stress in each cycle for a 240 μm mesh with 1 mm pores.

6.3 Tensile Tests After Cyclic Loading Conditions

After undergoing cyclic testing, the 240 μm samples were subjected to a uniaxial tensile test to assess the material's cyclic damage. This is to infer how much of the material's original strength remains after it has been subjected to cyclic loading. Figure 6.4 shows the stress-strain curves of the 240 μm filament diameter meshes of both 1.5 and 1 mm pore sizes before and after performing cyclic testing.

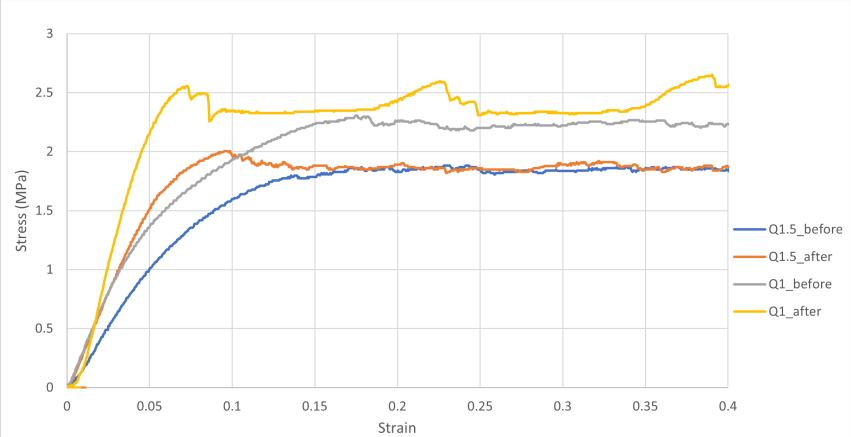


Figure 6.4: Effect of cyclic loading conditions on 240 μm samples with 1.5 and 1 mm pores.

The maximum stress values and Young's modulus calculated before and after the cyclic tests are present in Table 6.4 for each pore size.

Table 6.4: Maximum stress values and Young's modulus obtained after cyclic loading.

	Pore size (mm)	σ_{max} **(MPa)**	E **(MPa)**
Before Cyclic Loading	1.5	1.88	23.43
	1	2.31	32.47
After Cyclic Loading	1.5	2.01	33.16
	1	2.65	40.19

6.4 Results Analysis

As previously mentioned, available surgical synthetic pelvic meshes for POP repair are associated with high complication rates and risks, affecting the health and quality of life of women. The reported complications include mesh infection, recurrent prolapse, erosion of the mesh through the vagina, and urinary problems. These are associated with the synthetic mesh's insufficient biocompatibility and inappropriate biomechanical properties. The production of biodegradable meshes

for POP repair through 3D printing technologies emerges as an alternative, allowing the manufacture of less stiff and more deformable meshes, decreasing their negative outcomes. In this study, the performance of 3D-printed biodegradable meshes is assessed by performing uniaxial tensile tests to ensure appropriate mesh stiffness, and their performance under cyclic loading conditions is evaluated to predict their long-term behavior.

The results obtained in the uniaxial tensile tests of the printed meshes reveal that there is initially an elastic region where the mesh can still return to its original position despite the samples being deformed. In this region, the stress-strain relationship is approximately linear, with the slope representing Young's Modulus. Once the yield stress value is reached, the material behavior switches from elastic to plastic. From this point on, the deformation is permanent, and the stress-strain curve starts to form a curve-like shape until it reaches the maximum stress value. At this point, the curve stabilizes, as typical when plasticity is reached. The final stage, not depicted in the shown curves, consists of the fracture. This is when the sample breaks completely [75].

The PCL meshes present a similar behavior among themselves, which suggests that the plastic behavior is mainly controlled by the material, PCL, and sample geometry, not its diameter or pore size, the varied characteristics. The stress-strain curve of the 160 μm diameter sample with 1.5 mm pores presents a slightly different behavior from the other samples after reaching the maximum stress. While the 160 μm diameter sample with 1 mm pores and both of the 240 μm diameter samples remain approximately constant after the maximum stress point, the 160 μm sample with 1.5 mm pores presents a stress decrease. This could be due to the testing machine's grips crushing the already thin material, leading to higher degradation. Furthermore, the fracture of the samples occurred very close to the grips rather than in the middle, likely due to the force exerted by the grips. That is why a curve of the 160 μm diameter sample with 1.5 mm pore expected behavior was represented, considering other curves and previous studies [107]. The following analysis was performed considering the results obtained by this curve.

The obtained maximum stresses suggest that the 240 μm diameter sample with 1 mm pores has a higher resistance to plastic deformation, and the 160 μm with 1.5 mm pores has the lowest. It can be observed that the 240 μm diameter samples endure about 25% more stress than 160 μm ones. Also, the samples of 1 mm pore size endure about 18% more stress than the 1.5 mm ones. Considering this, it can be concluded that the higher the filament diameter and the smaller the pores, the greater the stress the samples can handle before failure, and vice versa, which is in line with *Cunha et al.* findings in 2021 [8]. Despite this, mesh pores smaller than 1 mm have been associated with a high risk of infection due to poor tissue growth. This sets an acceptable range of pore sizes from 1 to 2 mm [51].

Analyzing the Restorelle® mesh, a continuous increase of its stress with the strain and, therefore, higher stiffness can be observed, unlike the PCL meshes. At 20% strain, the commercial mesh presents a stress value of 3.62 MPa, a much greater value than those obtained from the anterior and posterior human tissue of 0.56 MPa and 0.36 MPa, respectively. This suggests that the PCL meshes may have a more positive outcome than the commercial mesh, as reported from various studies [107].

The 3D-printed PCL meshes have the drawback of exhibiting plastic behavior at low strains. This behavior is not inherent to the material itself but rather to its square geometry. Other research has shown that different geometries, such as sinusoidal waves, closely mimic the behavior of vaginal tissue [75].

The polymer meshes with 160 μm fiber diameter are the most promising since their maximum stress values are the closest to those of the vaginal tissue in the comfort zone. In particular, the 1.5 mm pore mesh would be considered the best if the tests had gone according to the expected. Since that is not the case, the 160 μm mesh with 1 mm pores is considered the closest to the vaginal tissues. On the other hand, both of the PCL meshes with 240 μm diameters present high-stress values. Despite enduring more force, they are stiffer than the vaginal tissue and may result in complications such as mesh erosion [42].

The cyclic tests were performed to evaluate the performance of the meshes to repeated loads, mimicking the expected *in vivo* loads [108]. Concerning the cyclic tests, it can be seen that the material has a cyclic creep behavior since the plastic deformation accumulates, and the curves do not go back to the same displacement [117]. This is a common result in polymers due to their viscous material behavior [118].

The fatigue is not linear in the first cycle, which basically consists of a uniaxial tensile test. This is due to the polymer's chain alignment and possibly plastic deformation [118]. It can be seen that the first cycle is the one that causes the most damage to the mesh since the area of the loop gradually decreases with the number of cycles. This suggests that the material undergoes hardening when plastic deformation occurs [119]

Although the loads the materials are subjected to in the pelvic floor are not well studied, *Roman et al.* defined a 25% strain rate that the vaginal tissues can endure without damage. From the calculated average strain variations, we can see that all samples exhibit a strain variation lower than 2%, which is much lower, meaning that the mesh deformations appear to be appropriate for their intended application [109]. In particular, both of the 160 μm that proved to be less stiff in the tensile tests and, therefore, were considered superior, presenting a reduced strain variation.

Calculating the strain the samples were subjected to in each cycle shows a trend towards strain stabilization with low strain increase. Although the meshes underwent significant strain in the first cycles, the material response to cyclic loading is becoming more stable and predictable.

Since the meshes presented plastic deformation in the cyclic tests, tensile tests were performed to check the material's fatigue damage. These tests showed increased maximum stress and Young's modulus on the meshes subjected to cyclic loading conditions. This shows that during the cyclic tests, the material suffered hardening, and the PCL chains suffered chain alignment [109].

Mechanically testing biomaterials is of vital importance in assessing materials for future clinical use. The uniaxial tensile tests provided important insights regarding the stiffness of the printed meshes. Their deformation was then evaluated under cyclic fatigue testing. It was proved that the printed meshes are less stiff than the commercial mesh and, therefore, closer to the vaginal tissue behavior. The material deformation appears to be appropriate for the intended application.

Chapter 7

Antimicrobial Incorporation Results

The following chapter outlines and discusses the results obtained regarding the antimicrobial agents' incorporation in the meshes. First, the results obtained from FTIR spectroscopy are presented. Then, the results obtained in the microbiological assays are approached, more precisely, zone inhibition and biofilm formation assays. Finally, these results were analyzed thoroughly.

7.1 FTIR Spectroscopy

FTIR spectroscopy analysis was performed to ensure the antibiotics were incorporated into the 3D-printed meshes. The FTIR spectra were obtained for PCL meshes with the previously mentioned concentrations of the antibiotics (gentamicin sulfate, azithromycin, and ciprofloxacin), without them (control), and with only the solvents used (distilled water and pure ethanol). The obtained FTIR spectra are displayed in Figures 7.1 to 7.5. It's important to note that the peak intensity or reflectance does not allow quantifying the amount of antibiotics present.

When analyzing the FTIR spectra of the control sample, that can be seen in Figure 7.1, peaks in the wavelengths of PCL's chemical bonds and functional groups were observed, as detailed in Table 7.1. These peaks were consistently present in all samples, although sometimes with lower intensity. This is expected, as all the samples were composed of PCL despite the solvents and incorporated antibiotics.

Table 7.1: PCL peaks detected in FTIR spectroscopy [120].

Wavelength (cm^{-1})	**Peak characteristics**
2943	Asymmetric CH_2 stretching
2866	Symmetric CH_2 stretching
1721	$C = O$ carbonyl stretching
1471 - 732	Bending, wagging, twisting, and stretching vibrations of the CH_2 groups, C-O and C-C bonds in the ester linkages of the polymer

FTIR spectra were obtained for both the PCL meshes sterilized under UV-C light and for PCL meshes that did not go through this stage. This was performed to infer if UV-C exposure affected PCL's chemical structure. From Figure 7.1 it can be seen that the structure of PCL, besides presenting some slight alterations, was not drastically altered. It's important to note that in the upcoming results, the spectrum used as a control is the one obtained from the PCL samples that were sterilized with UV-C light since the samples with antibiotics also went through this process.

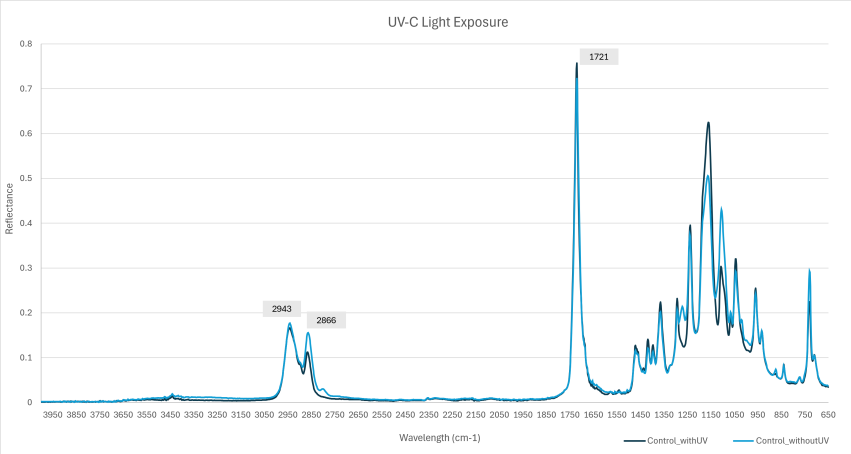


Figure 7.1: FTIR spectrum of PCL meshes that were sterilized under UV-C light and PCL meshes that were not subjected to this process.

FTIR spectra were also obtained for the meshes with only solvent incorporation, present in Figure 7.2. For both distilled water and pure ethanol, the peaks coincided with the ones from PCL, the control.

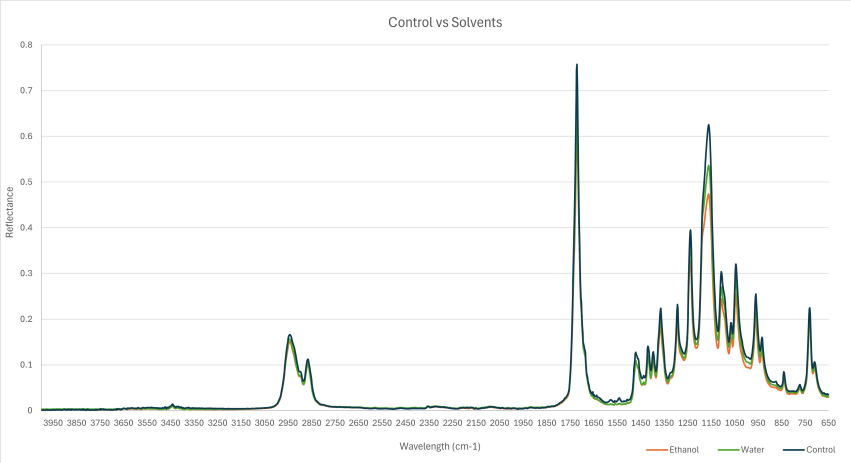


Figure 7.2: FTIR spectrum of meshes with solvent incorporation, compared with the control (PCL) spectrum.

In Figure 7.3 is the FTIR spectrum obtained for 0.15% and 0.2% concentration of incorporated azithromycin, compared to the control spectrum (PCL). It can be observed that the spectrum of both concentrations coincides with the control one.

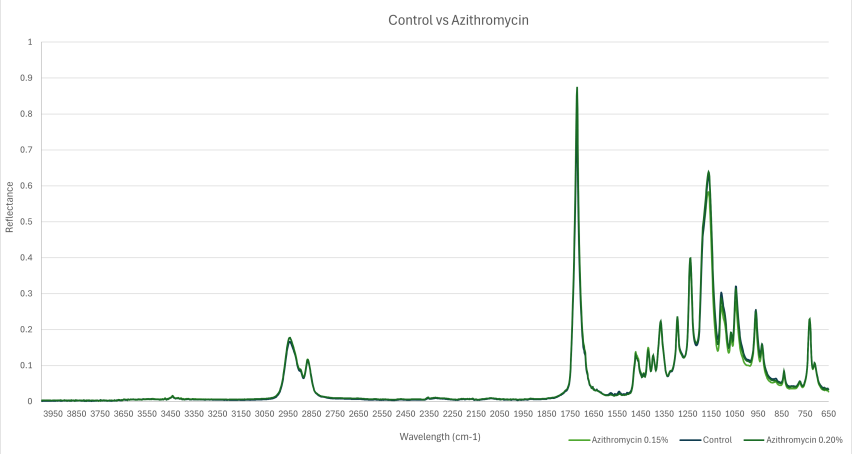


Figure 7.3: FTIR spectra of meshes coated with azithromycin compared with the control (PCL) spectrum.

FTIR spectroscopy was performed for both samples with 1% and 2% gentamicin sulfate, which can be seen in Figure 7.4. For the 1% gentamicin sulfate, the FTIR spectra coincided with the control one. However, for the 2% concentration, two peaks were identified and are highlighted in Table 7.2.

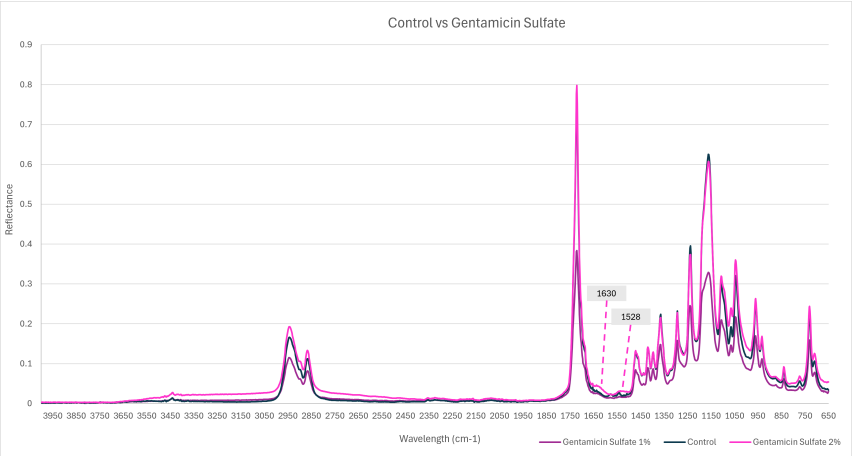


Figure 7.4: FTIR spectra of meshes coated with gentamicin sulfate compared with the control (PCL) spectrum.

Table 7.2: Gentamicin sulfate peaks detected in FTIR spectroscopy [121].

Wavelength cm^{-1}	**Peak characteristics**
1630	$N-H$ I vibration
1528	$N-H$ II vibration

Figure 7.5 shows the FTIR spectrum for the incorporation of ciprofloxacin and its comparison with the control, the PCL spectrum. The most relevant peaks identified are present in Table 7.3.

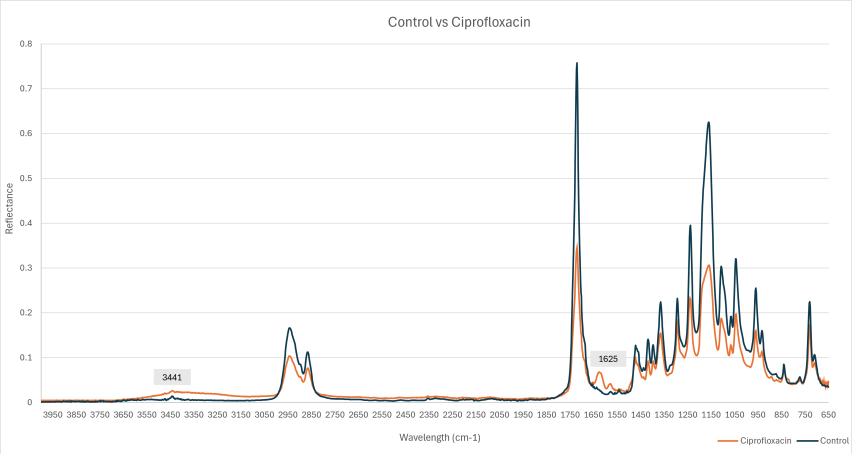


Figure 7.5: FTIR spectrum of meshes coated with ciprofloxacin compared with the control (PCL) spectrum.

Table 7.3: Ciprofloxacin peaks detected in FTIR spectroscopy [122].

Wavelength cm^{-1}	**Peak characteristics**
3441	OH stretch
1625	$C == O$ vibration

7.2 Microbiological Assays

This section presents the results of the microbiological assays. These assays were performed using two different approaches: zone inhibition and biofilm formation assays.

7.2.1 Zone Inhibition Assay

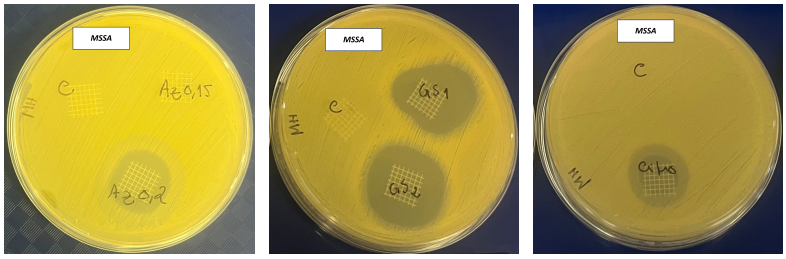
For the zone inhibition assay, the diameter of inhibition was measured for each mesh coated with antibiotics and compared with the control, the PCL mesh, for each bacterial strain to obtain information regarding the antimicrobial activity of the meshes. These results are in Table 7.4.

Figures 7.6 to 7.8 show images of the obtained inhibition zone radius for each bacterial strain.

The obtained results regarding *MSSA* ATCC 29213 can be seen in Figure 7.6. All of the meshes with incorporated drugs presented an inhibition zone. Of all, the 0.2% azithromycin-coated meshes presented a greater inhibition zone.

Table 7.4: Measured diameters of inhibition.

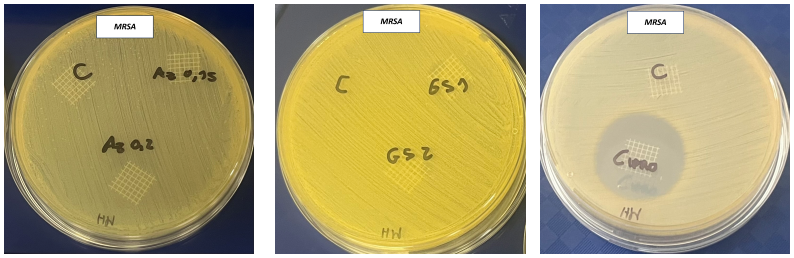
	MSSA **ATCC 29213**	***MRSA*** **ATCC 43300**	***E. coli*** **ATCC 25922**
Control	0 mm	0 mm	0 mm
Azithromycin (0.15%)	11 mm	0 mm	0 mm
Azithromycin (0.20%)	35 mm	0 mm	22 mm
Gentamicin Sulfate (1%)	32 mm	0 mm	30 mm
Gentamicin Sulfate (2%)	31 mm	0 mm	31 mm
Ciprofloxacin (0.90%)	26 mm	29 mm	39 mm



(a) (b) (c)

Figure 7.6: *MSSA* ATCC 29213 zone inhibition assay results for: (a) Azithromycin (Az); (b) Gentamicin Sulfate (GS); (c) Ciprofloxacin (Cipro).

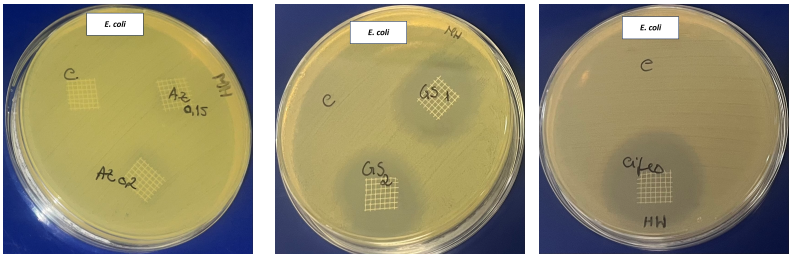
The results concerning *MRSA* ATCC 43300 are shown in Figure 7.7. Of all the tested drugs, only ciprofloxacin appeared to have antimicrobial activity against this bacteria strain. None of the azithromycin concentrations caused the formation of a diameter of inhibition, as well as in gentamicin sulfate.



(a) (b) (c)

Figure 7.7: *MRSA* ATCC 43300 zone inhibition assay results for: (a) Azithromycin (Az); (b) Gentamicin Sulfate (GS); (c) Ciprofloxacin (Cipro).

The zone of inhibition formed by the effect of the different drugs on *E. coli* ATCC 25922 can be seen in Figures 7.8. Ciprofloxacin presented a greater inhibition zone of 39 mm. Both concentrations of gentamicin sulfate presented antibacterial activity against *E. coli* ATCC 25922. Regarding azithromycin, no inhibition zone was observed for both of its concentrations.



(a) (b) (c)

Figure 7.8: *E. coli* ATCC 25922 zone inhibition assay results for: (a) Azithromycin; (b) Gentamicin Sulfate; (c) Ciprofloxacin.

7.2.2 Biofilm Formation Assays

The biofilm formation assays were performed using XTT and CV assays to obtain information regarding the metabolic activity of the biofilm viable cells (XTT) and the biofilm's biomass, including extracellular matrix, viable and dead cells concentration (CV) [123]. Regarding *MRSA* ATCC 43300, it was decided to perform the biofilm assays only for the higher concentrations of gentamicin sulfate and azithromycin since none of these antibiotics showed a radius of inhibition in this bacteria strain.

The results of the XTT and CV assays are presented in Figure 7.10 to 7.14. The graphs depict the percentage of reduction in metabolic activity of the biofilm (XTT) and biofilm cell concentration (CV) for each antibiotic relative to the positive control. These results are for *MSSA* ATCC 29213 (Figure 7.10), *MRSA* ATCC 43300 (Figure 7.12), and *E. coli* ATCC 25922 (Figure 7.14). Statistically significant differences in the XTT assay were found in ciprofloxacin-coated meshes with *MRSA* ATCC 43300 and all of the drug-loaded meshes with *E. coli* ATCC 25922 except for 0.2% azithromycin. However, no statistically significant differences were found in the samples for the CV assay.

Images of the different meshes and bacteria strains obtained through scanning electron microscopy (SEM) can be seen in Figure 7.9 to 7.15. Figure 7.9 compares SEM images of the PCL meshes (negative control) and meshes with the solvents (distilled water and pure ethanol). Minimum fiber diameter variations with solvent incorporation can be seen.

As seen in Figure 7.10 (a) and following *Lade et al.* classification [112], ciprofloxacin and both concentrations of gentamicin presented a high reduction of the *MSSA* ATCC 29213 biofilm's metabolic activity. On the other hand, the 0.2 % azithromycin showed a moderate reduction of the biofilm's metabolic activity, while the 0.15% azithromycin's metabolic activity was still high.

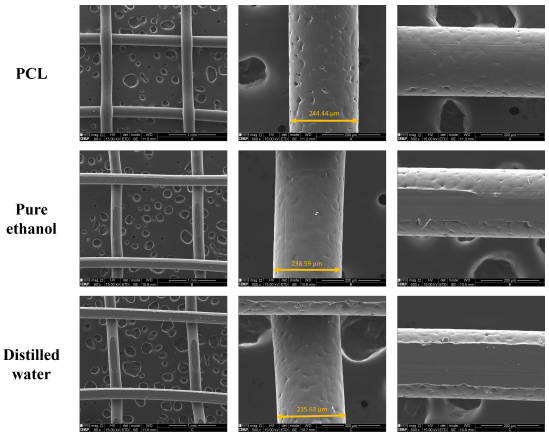
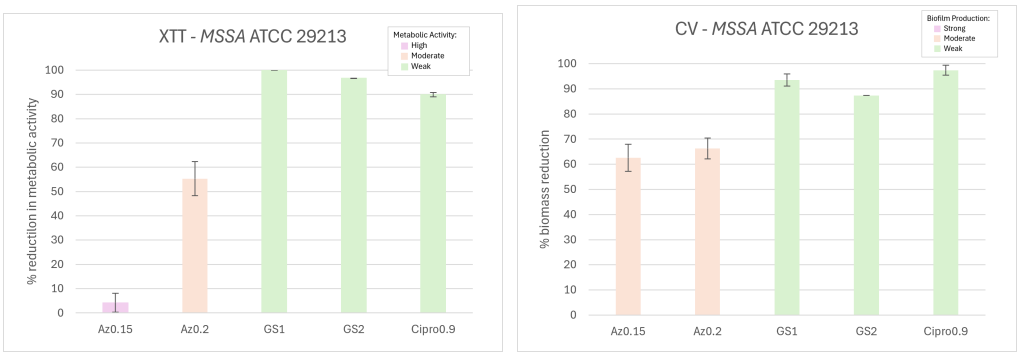


Figure 7.9: SEM images of PCL meshes and incorporated solvents.

Figure 7.10 (b) shows ciprofloxacin and both gentamicin concentrations presented a high reduction of the *MSSA* ATCC 29213 biofilm's biomass. On the other hand, both azithromycin concentrations caused only a moderate decrease in the concentration of biofilm cells. The results for these assays are mostly in accordance, only differing in 0.15% azithromycin's high metabolic activity and moderate biofilm biomass.



(a) (b)

Figure 7.10: *MSSA* ATCC 29213 biofilm formation: (a) XTT assay; (b) CV assay.

The SEM images regarding *MSSA* ATCC 29213 can be seen in Figure 7.11. From these images, it can be seen that the control has a high bacteria and biofilm presence. It is evident that all of the meshes present less bacterial content, with particularly low bacterial presence in ciprofloxacin and gentamicin-loaded meshes. In the azithromycin-incorporated meshes, the bacterial content is moderate.

Figure 7.12 (a) for *MRSA* ATCC 43300 shows that ciprofloxacin presented a high reduction of the biofilm's metabolic activity. On the other hand, for both the 0.2 % azithromycin and 2% gentamicin, the metabolic activity of the bacteria's biofilm was not largely reduced. Ciprofloxacin presented a high biofilm biomass reduction in Figure 7.12 (b) for *MRSA* ATCC 43300. A moderate biofilm concentration reduction can be observed in 2% gentamicin, while 0.2% azithromycin presented a low reduction.

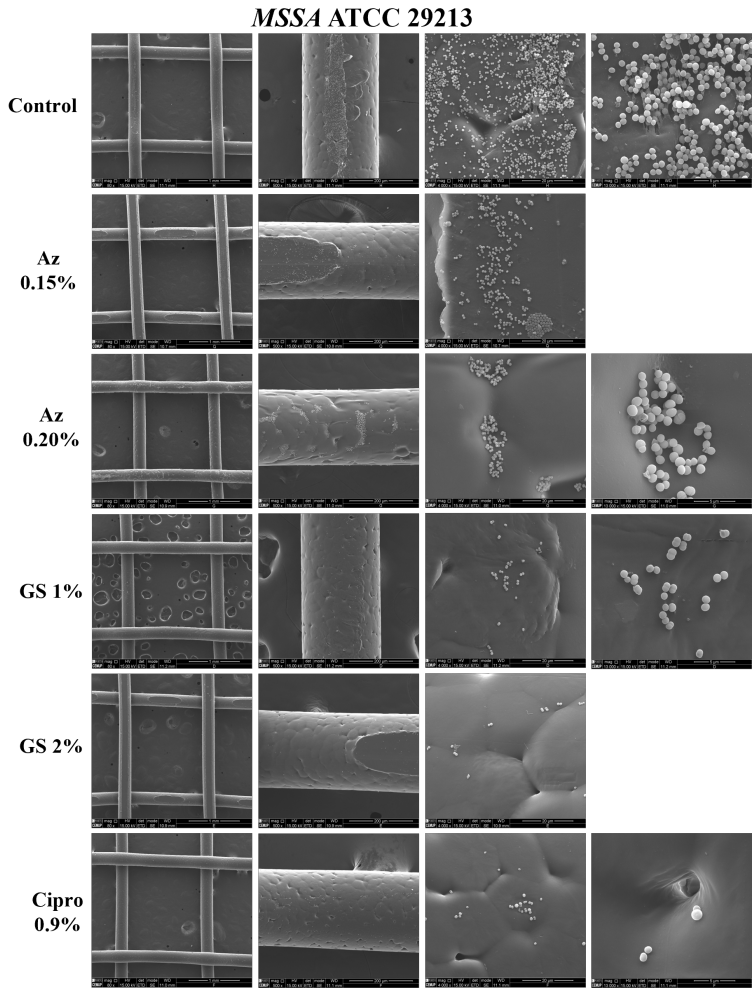
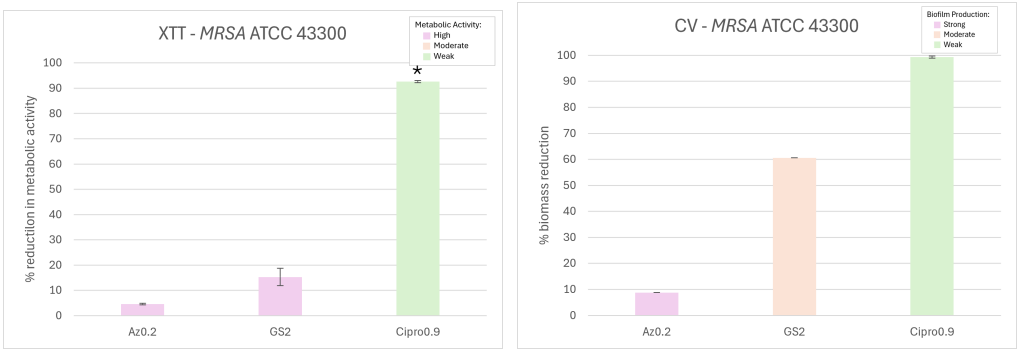


Figure 7.11: SEM images of *MSSA* ATCC 29213 antibiotic loaded meshes.



(a) (b)

Figure 7.12: *MRSA* ATCC 43300 biofilm formation: (a) XTT assay; (b) CV assay.

The obtained SEM images regarding *MRSA* ATCC 43300 can be seen in Figure 7.13. A high reduction of bacterial content is clearly observable in ciprofloxacin-loaded meshes, while this is not observable with azithromycin and gentamicin.

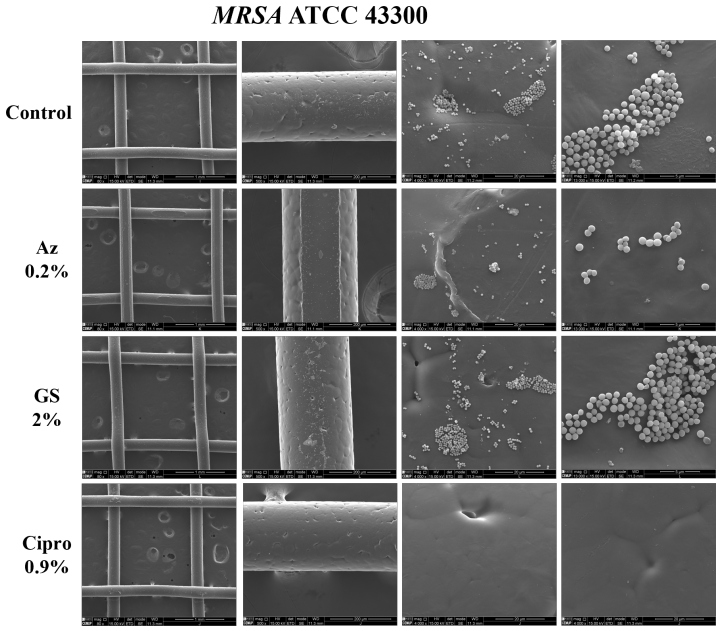
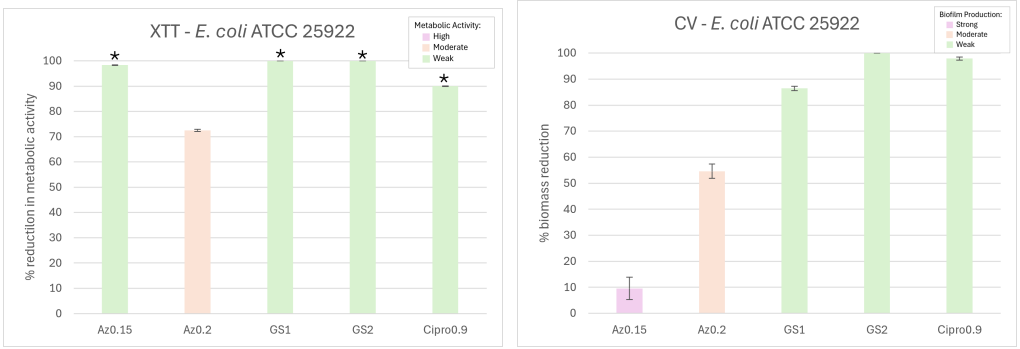


Figure 7.13: SEM images of *MRSA* ATCC 43300 in drug-loaded meshes.

As seen in Figure 7.14 (a), all the antibiotics and concentrations decreased the biofilm's metabolic activity in *E. coli* ATCC 25922 largely, except for the 0.2% azithromycin, which moderately reduced the biofilm's metabolic activity. As seen in Figure 7.14 (b), ciprofloxacin and both concentrations of gentamicin sulfate greatly decreased biofilm production in *E. coli* ATCC 25922. The 0.2% azithromycin moderately decreased the biofilm's biomass, while the 0.15% azithromycin could not reduce the biofilm's production.



(a) (b)

Figure 7.14: *E. coli* ATCC 25922 biofilm formation: (a) XTT assay; (b) CV assay.

SEM images regarding *E. coli* ATCC 25922 can be seen in Figure 7.15. In these SEM images, the control samples show several bacteria colonies and biofilm. Both gentamicin sulfate (GS) concentrations show almost no bacteria presence, while collapsed bacteria can be seen in ciprofloxacin. For both azithromycin concentrations, there is relatively low bacterial content, with the particularity of, in the 0.15% concentration, the bacteria presenting a long shape.

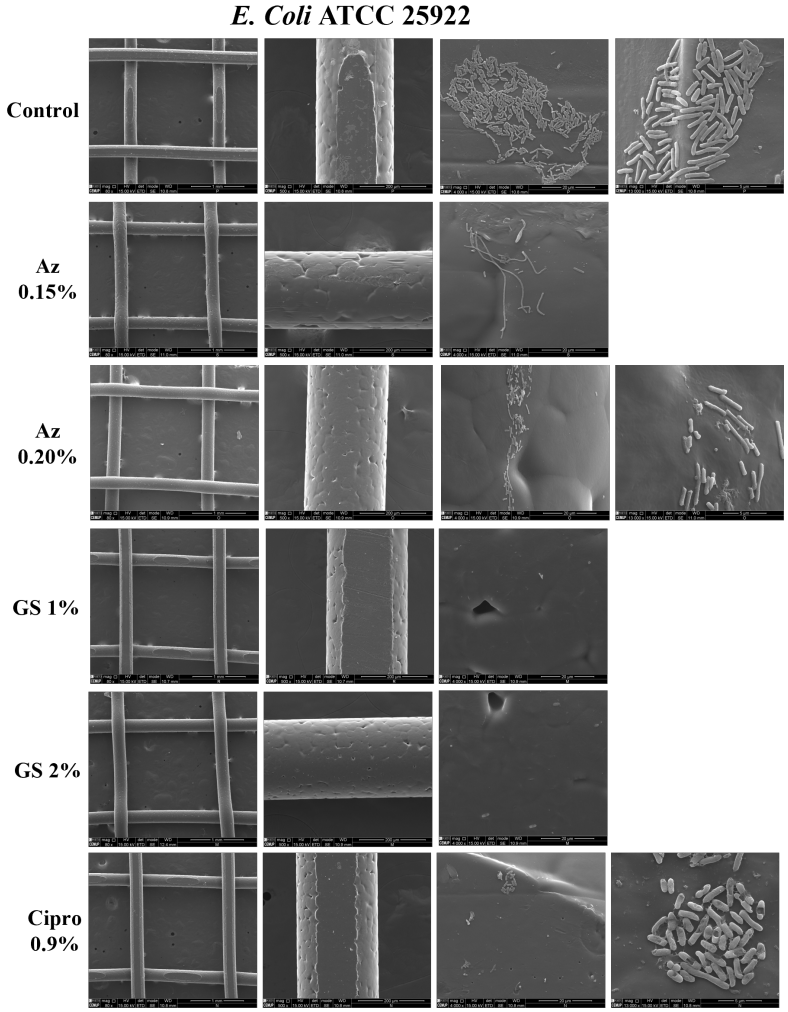


Figure 7.15: SEM images of *E. coli* ATCC 25922 in meshes with antibiotic incorporation.

7.3 Result Analysis

Regarding the PCL's FTIR spectrum, typical peaks of symmetric and asymmetric CH_2 stretching were detected at 2943 and 2866 cm^{-1}, respectively. The most prominent peak at 1721 cm^{-1}, which corresponds to the carbonyl stretching, and the peak complex around the 1471-732 cm^{-1} region were also detected [120]. This complex includes the peak detected at 1294 wavelength, corresponding to the $C-O$ and $C-C$ stretching in the crystalline phase. At 1239 and 1160 cm^{-1} the asymmetric and symmetric COC stretching peaks, respectively, were detected [124].

All of the tested meshes presented FTIR peaks characteristic of PCL, confirming its presence. In the meshes coated with antibiotics, a slight decrease of the PCL peaks intensity can be seen, which suggests that, although PCL is still present, other substances are also present in the meshes, even if other chemical bonds or functional groups are not noticeable.

UV-C light is commonly used for disinfection in various settings. It works by inactivating the DNA of pathogens through the absorption of high photon energy. This causes damage to the peptide and disulfide bonds of the DNA, ultimately destroying the organisms [125]. During this work, it was necessary to ensure the produced meshes were sterile to evaluate the effect of the incorporated antibiotics when in contact with different bacterial strains. FTIR analysis of the only PCL meshes before and after the disinfection process was conducted to confirm whether the material maintained the biochemical characteristics after exposure to UV-C light. The peaks identified in the PCL meshes that underwent UV-C light are similar to those of the PCL meshes that did not go through the sterilization stage. The minor variations in peak intensity suggest slight degradation in the PCL structure due to UV-C exposure, but the overall chemical structure of the polymer remains intact. The absence of new peaks or significant shifts indicates minimal chemical changes due to UV-C exposure.

The solvent's incorporation in the meshes was evaluated through FTIR spectroscopy and SEM images. As expected, the solvents' FTIR spectra coincided with PCL's peaks since the samples were air-dried for 24 hours, causing solvent evaporation [126]. Therefore, it can be concluded that PCL did not suffer chemical degradation. In the SEM images, the filament diameter decreases by about 2.3% with ethanol incorporation and 3.3% with water, presenting minimal differences from the PCL-only filament. Other studies reported polymer swelling or degradation visible in SEM imaging, but this is not the case [127].

Taking into account the results from both of these tests, it can be concluded that the solvents did not alter PCL's chemical structure, influence the presence of the antibiotics, or cause its degradation, which is as expected since PCL is primarily susceptible to hydrolytic degradation in the presence of heat and enzymes. Besides not being chemically degraded, PCL's mechanical properties may be altered due to solvent incorporation, which was not analyzed in the present study [128].

Analysing FTIR spectroscopy results, it was not possible to detect azithromycin's characteristic peaks for any of the concentrations of this drug. However, this does not necessarily mean that azithromycin is absent since FTIR spectroscopy is not always effective at identifying materials in mixtures [129]. According to the literature, the only expected difference between the FTIR spectrum of PCL and azithromycin-loaded PCL is a peak around 3500-3000 cm^{-1}, characteristic of $O-H$ and $N-H$ stretching [130].

For the highest concentration of gentamicin sulfate incorporated in the meshes, two peaks were able to be identified: 1630 cm^{-1} and 1528 cm^{-1}. These peaks are characteristic of the $N-H$ bending vibrations of the aromatic amine present in gentamicin [121, 131]. Although these were small peaks, the incorporation of gentamicin sulfate into the PCL meshes was considered successful for the 2% concentration. These peaks were not identified for the 1% gentamicin-loaded meshes, although in previous studies, the FTIR peaks could be detected for the same concentration of this drug [76].

In the samples containing ciprofloxacin, two signature peaks of this drug were identified besides those from PCL. The peak found at 3441 cm^{-1} is related to the OH stretch vibration, typical of a carboxylic acid [122], and 1625 cm^{-1} peak of the $C == O$ vibration was also detected, typical of carboxylic acids and ketone groups [132], confirming the presence of ciprofloxacin. It can be challenging to distinguish additional peaks from ciprofloxacin in the PCL spectrum when they overlap or fall within densely populated regions by PCL's characteristic peaks. This could be the case for other typical ciprofloxacin peaks, such as the fluorine group $C-F$ stretching, common in fluoroquinolones, which is typically found around the 1050-1000 region [133] and could not be detected.

The presence of antibiotics in the meshes was proved for ciprofloxacin. The presence of gentamicin sulfate was confirmed for the meshes with the highest concentration of this drug. Neither of the concentrations of azithromycin was enough to prove its presence through FTIR spectroscopy. However, it was not concluded that the drugs were absent, as FTIR spectroscopy can be ineffective when identifying materials in mixtures since the antimicrobial's FTIR peaks may overlap with PCL's spectra [129]. Considering this, the microbiological assays were still performed for all the drug concentrations.

The obtained results show that the microbiological assays complement each other, particularly the XTT and CV assays, which provide information regarding biofilm formation. It is important to note that some of the optical density measurements obtained from these assays had to be discarded. Additionally, only a few samples proved to be statistically significant. This disparity in results is likely due to the high sensitivity of spectrophotometry analysis to environmental temperature and luminosity [134].

The SEM images regarding *MSSA* ATCC 29213 clearly show a high biofilm reduction for all the samples compared with the control, which is in accordance with the obtained results from the zone inhibition assay where all the antibiotics showed a radius of inhibition, proving their antimicrobial activity for this bacteria strain. This occurred as expected since this bacteria strain is susceptible to various antimicrobials and is often used as quality control [135].

For *MSSA* ATCC 29213, the results from both XTT and CV assays are mainly in accordance, differing in 0.15% azithromycin. The fact that with this antibiotic concentration, more viable cells were detected than biofilm strength could be due to the microorganisms being in the proliferative stage, resulting in less extracellular matrix and a decrease in biofilm biomass [123]. Regarding the SEM images, more bacteria appear to be visible in the samples with 0.2% azithromycin than in the 0.15% azithromycin. This may be due to the previously explained reason or to the possibility that the difference in the concentrations used is insufficient to cause a more effective antibacterial action. In 2% GS, more bacterial content appears to be present than in 1% GS, but this is probably because the viewed mesh face for 1% GS is the one that solidified on the collector plate during the printing process, being smoother and difficulting bacterial adhesion. Additionally, *S. aureus* have been reported to strongly adhere to the filament holes, which can not be seen from this view [76].

Gentamicin proved to be effective in reducing biofilm formation and cell viability for both of its concentrations, proving its antibacterial activity against *MSSA* ATCC 29213. No major differences between both concentrations were observed in the microbiological assays, suggesting that 1% GS is enough to reduce bacterial activity. Ciprofloxacin, alike GS, proved to be highly effective in reducing the biofilm's metabolic activity and biomass. Once again, this follows the SEM images and zone inhibition assay, proving ciprofloxacin's antibacterial activity against *MSSA* ATCC 29213. This bacteria strain is susceptible to both ciprofloxacin and gentamicin [136]. For 0.9% ciprofloxacin concentration, this susceptibility was confirmed, as well as for both 1% and 2% concentrations of gentamicin. Azithromycin was a less effective antibiotic for *MSSA* ATCC 29213. There was moderate biofilm production with high metabolic activity and visible biofilm in the SEM images despite its antibacterial activity seen in the zone inhibition assay. This suggests that azithromycin is effective against bacteria in their planktonic state, but as they grow and aggregate, they develop a biofilm more tolerant to azithromycin [137]. *MSSA* ATCC 29213 is susceptible to azithromycin [138], but particularly for this strain and concentrations, only a moderate biofilm formation inhibition was seen. Previous studies using 0.01% azithromycin proved to be effective at suppressing the growth of other *S. aureus* strains [10].

MRSA is known as one of the most serious antibiotic-resistant bacteria, contrary to *MSSA*, due to its capability of developing multidrug resistance [139]. The SEM images showed a high bacterial content reduction in *MRSA* ATCC 43300 for ciprofloxacin but not for gentamicin and azithromycin, which is in accordance with the results obtained from the zone inhibition assay, where only ciprofloxacin proved to have antibacterial activity for this bacteria strain.

MRSA ATCC 43300 had a high metabolic activity when in the presence of 0.2% azithromycin and 2% GS, which suggests that the same results would be obtained for the lower concentrations. The difference in 2% GS moderate biofilm biomass and high metabolic activity is possibly due to the bacteria being in the proliferation stage, as previously explained [123].

MRSA ATCC 43300 had high biofilm production with high metabolic activity in the presence of azithromycin, proving its resistance to this antibiotic at the used concentration [139]. *MRSA* ATCC 43300 is also gentamicin-resistant [140], and this resistance was verified for the tested concentration. Although ciprofloxacin's susceptibility to this particular bacteria strain is not well documented, in another study, ciprofloxacin has proved to reduce *MRSA* ATCC 43300 growth by 26% for a lower concentration of this antibiotic, proving the susceptibility of this bacteria strain to ciprofloxacin [141]. For the used concentration in this study, ciprofloxacin has proven to be highly effective in reducing the biofilm's metabolic activity and biomass. This is in accordance with the SEM images, which hardly show bacterial presence, and the zone inhibition assay, which proves ciprofloxacin's antibacterial activity against *MRSA* ATCC 43300 at the used concentration. This is particularly interesting since *MRSA* ATCC 43300 is resistant to several antibiotics [139].

The SEM images obtained for *E. coli* ATCC 25922 show a reduction of bacterial content with the antibiotics, which is mainly in agreement with the zone inhibition assays, in which all antibiotics proved to have antimicrobial activity against this bacteria strain, except for the lowest concentration of azithromycin.

The fact that the *E. coli* ATCC 25922 bacteria in the 0.15% azithromycin present low metabolic activity but high biomass is probably because the XTT assay detects only active cells, while the CV assay may be detecting the extracellular matrix of dead cells from the long cultivation time [123]. On the other hand, the highest concentration of azithromycin exhibits less reduction in metabolic activity in the XTT assay than the lowest concentration, suggesting a possible sample swap during the experimental work.

The 0.2% azithromycin produced moderate biofilm and metabolic activity. This aligns with the SEM images that showed bacterial content, although to a lesser extent. The small inhibition radius formed in the zone inhibition assays suggests azithromycin has a slight antibacterial activity for *E. coli* ATCC 25922. Azithromycin 0.15% had a high biofilm production but low metabolic activity. As previously referred, this may be due to extracellular matrix remainings. In fact, a vast amount of bacteria can not be seen in the SEM images, but the detected ones presented a long fungi-like appearance. This growth of bacteria, called filamentation, occurs when bacteria continue growing when the division stops. This could be due to unfavorable conditions, such as antibiotic exposure, temperature shocks, or genetic mutations [142]. In the zone inhibition assays, the lower azithromycin concentration did not prove to have antibacterial activity against *E. coli* ATCC 25922, which has been proven to be resistant to macrolides, such as azithromycin [143]. The obtained results suggest that some level of antibacterial activity would be seen for higher concentrations of azithromycin. However, there are no studies in the literature that support that conclusion.

Both gentamicin concentrations highly reduced the biofilm's biomass and metabolic activity and showed almost no bacteria presence in the SEM images, following the zone inhibition assay results and proving this drug's antibacterial activity against *E. coli* ATCC 25922. This is as expected since this bacteria strain is susceptible to gentamicin [144], proving its susceptibility and inhibition of biofilm formation for both 1% and 2% concentrations of this antibiotic.

Alike GS, ciprofloxacin caused a pronounced reduction in the biofilm's biomass and metabolic activity. This is consistent with the formed inhibition radius, proving ciprofloxacin's antibacterial activity against *E. coli* ATCC 25922, as expected, since this bacteria strain has been reported to be susceptible to this drug [145]. *E. coli* was detected in the SEM images, although the bacteria appeared to have collapsed. This collapse may be due to several factors, such as sample dehydration, vacuum pressure in the SEM chamber, or too high ciprofloxacin exposure. The sample preparation for this analysis may also cause the collapse, such as using chemical fixatives, like osmium, and improper application of the conductive coating [146].

Overall, the results obtained prove that the antimicrobial incorporation in the PCL meshes was successful. Ciprofloxacin was the most effective antibiotic, inhibiting biofilm formation in the three analyzed bacterial strains. Gentamicin was highly effective against *E. coli* ATCC 25922 and MSSA ATCC 29213. Considering the complications of meshes for POP repair, preventing biofilm formation is important to prevent the infection of these meshes and, therefore, the need to remove them. The tested antibiotics proved to be effective for the desired application, specifically ciprofloxacin, which inhibited the biofilm formation of all the tested bacterial strains.

Chapter 8

Conclusions and Future Work

This chapter summarizes the main conclusions obtained from the developed work and its limitations. Lastly, the steps to follow in future research are outlined.

8.1 Conclusions

Synthetic surgical meshes for pelvic organ prolapse have presented high complication rates. By using biodegradable materials to produce these meshes, their mechanical properties can be adjusted to better match the vaginal tissue's behavior, having lower stiffness and strain and therefore preventing the associated complications with these implants. Additionally, coating these mesh implants with antimicrobial agents can inhibit and prevent biofilm formation, ultimately preventing mesh infection. The performed study and findings present the potential to improve the outcomes of surgical pelvic meshes.

The first stage of the experimental work consisted of calibrating the MEW prototype and subsequent printing of the meshes using technical-grade PCL. Mechanical tests were performed to evaluate the printed meshes' mechanical properties in comparison with vaginal tissues. The main conclusions from this part of the work were:

- The square geometry of the meshes limits their mechanical behavior.
- Meshes with smaller fiber diameters and larger pore sizes, particularly the 160 μm meshes, are the closest to the vaginal tissue's behavior.
- The printed meshes are less stiff than the commercial mesh.
- When subjected to cyclic loading conditions, the samples suffered deformation but resisted failure for 100 cycles. The most damage occurs in the first cycle; after that, the deformation follows a logarithmic shape, where the strain approximately stabilizes.
- The stiffness of the meshes increased after cyclic loading conditions.

Separately, the meshes were coated with azithromycin, gentamicin sulfate, and ciprofloxacin. This incorporation was analyzed through FTIR. Zone inhibition and biofilm formation assays were performed against *E. coli* ATCC 25922, *MSSA* ATCC 29213, and *MRSA* ATCC 43300, to evaluate the meshes' biofilm formation and the drug's capability to prevent it. SEM analysis was also performed to obtain images of the bacterial content in the drug-coated meshes. From this research, it was concluded that:

- FTIR spectroscopy alone is insufficient to confirm antimicrobial incorporation in the 3D-printed PCL meshes.
- FTIR and SEM analyses demonstrated that the filament was not chemically altered by the used solvents or UV-C light exposure.
- Azithromycin and gentamicin sulfate have antibacterial activity against *E. coli* ATCC 25922 and *MSSA* ATCC 29213 strains.
- Ciprofloxacin proved to have antibacterial activity against *E. coli* ATCC 25922, *MSSA* ATCC 29213 and *MRSA* ATCC 43300.
- Gentamicin sulfate significantly inhibited biofilm formation in *E. coli* ATCC 25922 and *MSSA* ATCC 29213.
- Ciprofloxacin substantially reduced biofilm formation in *E. coli* ATCC 25922, *MSSA* ATCC 29213 and *MRSA* ATCC 43300, proving its potential in preventing biofilm formation in these strains at the tested concentrations.

Considering the above, combining melt electrospinning writing technology with antibiotic incorporation has the potential to produce biodegradable implants with appropriate mechanical properties and antibacterial action for pelvic organ prolapse repair, minimizing the complication and failure rates associated with these devices.

8.2 Limitations and Future Work

The developed work presents some limitations; for instance, mesh implants with filament diameters lower than 160 μm were not mechanically tested, though the presented results indicate that lower diameters reduce the complications associated with these implants due to their lower stiffness. Other mesh geometries that could closely match the pelvic tissues' mechanical behavior were not tested. It was also not possible to perform cyclic tests for more than 100 cycles. The material's mechanical degradation with the incorporation of the antibiotics was not tested. Although the tested bacteria strains are the most common in mesh-related infections, other strains and fungi that could also affect the performance of the implants were not tested, nor were other antimicrobial agents and concentrations. The process of microorganism adhesion to the implants was not studied.

Taking into account the mentioned limitations, for future work, the following steps should be performed:

- Mechanically test new mesh geometries to match the vaginal tissue behavior closely.
- Perform cyclic fatigue tests to evaluate the fatigue properties of the produced meshes.
- Perform mechanical tests with solvent or drug-loaded meshes to check if their mechanical properties are altered.
- Optimize the MEW printing process to have more even fibers without holes to allow less bacterial adhesion.
- Conduct adhesion assays to better understand the biofilm production process.
- Performing microbiological assays with fungi and other bacteria strains to evaluate the effectiveness of the developed implants against a wider range of pathogens.

References

[1] T. F. M. Vergeldt, M. Weemhoff, J. Inthout, and K. B. Kluivers, "Risk factors for pelvic organ prolapse and its recurrence: a systematic review," *International Urogynecology Journal*, vol. 26, no. 11, pp. 1559–1573, 2015. [Online]. Available: http://link.springer.com/10.1007/s00192-015-2695-8

[2] C. B. Iglesia and K. R. Smithling, "Pelvic Organ Prolapse," *American Family Physician*, vol. 96, no. 3, 2017. [Online]. Available: www.aafp.org/afp

[3] J. Ferreira, "Biomecânica: Combinar engenharia e experiência clínica para melhorar o tratamento do prolapso de órgãos pélvicos femininos," 2020, (Last accessed 1 June 2024). [Online]. Available: https://www.inegi.pt/pt/noticias/biomecanica-combinar-engenharia-e-experiencia-clinica-para-melhorar-o-tratamento-do-prolapso-de-orgaos-pelvicos-femininos/

[4] C. f. D. a. R. Health, "Urogynecologic Surgical Mesh Implants," Aug. 2023, (Last accessed 25 October 2023). [Online]. Available: https://www.fda.gov/medical-devices/implants-and-prosthetics/urogynecologic-surgical-mesh-implants

[5] N. Mangir, S. Roman, C. R. Chapple, and S. MacNeil, "Complications related to use of mesh implants in surgical treatment of stress urinary incontinence and pelvic organ prolapse: infection or inflammation?" *World Journal of Urology*, vol. 38, no. 1, pp. 73–80, 2020. [Online]. Available: https://www.ncbi.nlm.nih.gov/pmc/articles/PMC6954150/

[6] A. Y. Weintraub, H. Glinter, and N. Marcus-Braun, "Narrative review of the epidemiology, diagnosis and pathophysiology of pelvic organ prolapse," *International Braz J Urol: Official Journal of the Brazilian Society of Urology*, vol. 46, no. 1, pp. 5–14, 2020.

[7] E. Mancuso, C. Downey, E. Doxford-Hook, M. G. Bryant, and P. Culmer, "The use of polymeric meshes for pelvic organ prolapse: Current concepts, challenges, and future perspectives," *Journal of Biomedical Materials Research Part B: Applied Biomaterials*, vol. 108, no. 3, pp. 771–789, 2020. [Online]. Available: https://onlinelibrary.wiley.com/doi/abs/10.1002/jbm.b.34432

[8] M. N. B. da Cunha, R. Rynkevic, M. E. T. da Silva, A. F. Moreira Da Silva Brandao, J. L. Alves, and A. A. Fernandes, "Melt Electrospinning Writing of Mesh Implants for Pelvic Organ Prolapse Repair," *3D Printing and Additive Manufacturing*, vol. 9, no. 5, pp. 389–398, 2021.

[9] J. Domínguez-Robles, C. Mancinelli, E. Mancuso, I. García-Romero, B. F. Gilmore, L. Casettari, E. Larrañeta, and D. A. Lamprou, "3D Printing of Drug-Loaded Thermoplastic Polyurethane Meshes: A Potential Material for Soft Tissue Reinforcement in Vaginal Surgery," *Pharmaceutics*, vol. 12, no. 1, p. 63, Jan. 2020.

[10] J. Ren, R. Murray, C. S. Wong, J. Qin, M. Chen, M. Totsika, A. D. Riddell, A. Warwick, N. Rukin, and M. A. Woodruff, "Development of 3D Printed Biodegradable Mesh with Antimicrobial Properties for Pelvic Organ Prolapse," *Polymers*, vol. 14, no. 4, p. 763, Feb. 2022.

[11] F. J. Calero Castro, Y. Yuste, S. Pereira, M. D. Garvín, M. A. López García, F. J. Padillo, and F. Portilla, "Proof of concept, design, and manufacture via 3-D printing of a mesh with bactericidal capacity: Behaviour in vitro and in vivo," *Journal of Tissue Engineering and Regenerative Medicine*, vol. 13, no. 11, pp. 1955–1964, Nov. 2019. [Online]. Available: https://onlinelibrary.wiley.com/doi/10.1002/term.2944

[12] N. Qamar, N. Abbas, M. Irfan, A. Hussain, M. S. Arshad, S. Latif, F. Mehmood, and M. U. Ghori, "Personalized 3D printed ciprofloxacin impregnated meshes for the management of hernia," *Journal of Drug Delivery Science and Technology*, vol. 53, p. 101164, Oct. 2019. [Online]. Available: https://linkinghub.elsevier.com/retrieve/pii/S1773224719305969

[13] S. R. Chaudhry, A. Nahian, and K. Chaudhry, "Anatomy, Abdomen and Pelvis, Pelvis," in *StatPearls*. Treasure Island (FL): StatPearls Publishing, 2023. [Online]. Available: http://www.ncbi.nlm.nih.gov/books/NBK482258/

[14] D. El-Mowafi, "Anatomy of the female pelvis," *Geneva Foundation for Medical Education and Research*, Aug 2023. [Online]. Available: https://www.gfmer.ch/Obstetrics_simplified/anatomy_of_the_female_pelvis.htm

[15] S. Paramasivam, A. Proietto, and M. Puvaneswary, "Pelvic anatomy and MRI," *Best Practice & Research Clinical Obstetrics & Gynaecology*, vol. 20, no. 1, pp. 3–22, Feb. 2006. [Online]. Available: https://www.sciencedirect.com/science/article/pii/S1521693405001148

[16] R. Kotarinos, "Musculoskeletal Pelvic Anatomy," in *Biomechanics of the Female Pelvic Floor*. Elsevier, 2016, pp. 53–87. [Online]. Available: https://linkinghub.elsevier.com/retrieve/pii/B9780128032282000039

[17] "Pelvis - Names of the Bones, Anatomy, & Labeled Diagram," (Last accessed 1 November 2023). [Online]. Available: https://www.theskeletalsystem.net/pelvis

[18] "Pelvic Organ Prolapse," (Last accessed 1 November 2023). [Online]. Available: https://austinurogynecology.com/pelvic-organ-prolapse/

[19] "Pelvic Floor Muscles: Anatomy, Function & Conditions," (Last accessed 26 October 2023). [Online]. Available: https://my.clevelandclinic.org/health/body/22729-pelvic-floor-muscles

[20] "Treatment options for pelvic organ prolapse: Minnesota Women's Care OBGYN and Urogynecology," (Last accessed 1 November 2023). [Online]. Available: https://mnwcare.com/our-services/treatment-incontinence-pelvic-floor-disorders/pelvic-organ-prolapse

[21] "Eunice Kennedy Shriver National Institute of Child Health and Human Development - NICHD," (Last accessed 25 October 2023). [Online]. Available: https://www.nichd.nih.gov/health/topics/factsheets/pelvicfloor

[22] M. Lin, Y. Lu, and J. Chen, "Tissue-engineered repair material for pelvic floor dysfunction," *Frontiers in Bioengineering and Biotechnology*, vol. 10, 2022. [Online]. Available: https://www.frontiersin.org/articles/10.3389/fbioe.2022.968482

[23] B. T. Haylen, D. De Ridder, R. M. Freeman, S. E. Swift, B. Berghmans, J. Lee, A. Monga, E. Petri, D. E. Rizk, P. K. Sand, and G. N. Schaer, "An International Urogynecological Association (IUGA)/International Continence Society (ICS) joint report on the terminology for female pelvic floor dysfunction," *International Urogynecology Journal*, vol. 21, no. 1, pp. 5–26, Jan. 2010.

[24] "Pelvic Organ Prolapse: Types, Causes, Symptoms & Treatment," (Last accessed 25 October 2023). [Online]. Available: https://my.clevelandclinic.org/health/diseases/24046-pelvic-organ-prolapse

[25] "Pelvic Organ Prolapse Quantification (POP-Q) System," (Last accessed 26 October 2023). [Online]. Available: https://www.physio-pedia.com/Pelvic_Organ_Prolapse_Quantification_(POP-Q)_System

[26] C. Persu, C. Chapple, V. Cauni, S. Gutue, and P. Geavlete, "Pelvic Organ Prolapse Quantification System (POP–Q) – a new era in pelvic prolapse staging," *Journal of Medicine and Life*, vol. 4, no. 1, pp. 75–81, Feb. 2011. [Online]. Available: https://www.ncbi.nlm.nih.gov/pmc/articles/PMC3056425/

[27] U. F. O. Themes, "Pelvic Organ Prolapse," *Abdominal Key*, Jul. 2016. [Online]. Available: https://abdominalkey.com/pelvic-organ-prolapse/

[28] "Diagnosis - Pelvic Organ Prolapse | Voices for PFD," (Last accessed 25 October 2023). [Online]. Available: https://www.voicesforpfd.org/pelvic-organ-prolapse/diagnosis/

[29] "Pelvic organ prolapse - Care at Mayo Clinic - Mayo Clinic," (Last accessed 27 October 2023). [Online]. Available: https://www.mayoclinic.org/diseases-conditions/pelvic-organ-prolapse/care-at-mayo-clinic/mac-20360560

[30] "Pelvic organ prolapse: Pelvic floor exercises and vaginal pessaries," in *InformedHealth.org [Internet]*. Institute for Quality and Efficiency in Health Care (IQWiG), Aug. 2018. [Online]. Available: https://www.ncbi.nlm.nih.gov/books/NBK525762/

[31] "Clinical effect of electrical stimulation biofeedback therapy combined with pelvic floor functional exercise on postpartum pelvic organ prolapse - PMC," (Last accessed 28 October 2023). [Online]. Available: https://www.ncbi.nlm.nih.gov/pmc/articles/PMC8290786/

[32] "Does oestrogen therapy help to treat pelvic organ prolapse in post-menopausal women?" (Last accessed 28 October 2023). [Online]. Available: https://www.cochrane.org/CD014592/INCONT_does-oestrogen-therapy-help-treat-pelvic-organ-prolapse-postmenopausal-women

[33] A. Taithongchai, E. E. Johnson, S. I. Ismail, E. Barron-Millar, A. Kernohan, and R. Thakar, "Oestrogen therapy for treating pelvic organ prolapse in postmenopausal women," *The Cochrane Database of Systematic Reviews*, vol. 7, no. 7, p. CD014592, Jul. 2023.

[34] R. Oliver, R. Thakar, and A. H. Sultan, "The history and usage of the vaginal pessary: a review," *European Journal of Obstetrics & Gynecology and Reproductive Biology*, vol. 156, no. 2, pp. 125–130, Jun. 2011. [Online]. Available: https://www.sciencedirect.com/science/article/pii/S0301211511000200

[35] "Vaginal pessary | Hospital da Luz Lisboa," (Last accessed 28 October 2023). [Online]. Available: https://www.hospitaldaluz.pt/lisboa/en/health-dictionary/vaginal-pessary

[36] B. B. Zeiger, S. da Silva Carramão, C. A. Del Roy, T. T. da Silva, S. M. Hwang, and A. P. F. Auge, "Vaginal pessary in advanced pelvic organ prolapse: impact on quality of life," *International Urogynecology Journal*, vol. 33, no. 7, pp. 2013–2020, 2022. [Online]. Available: https://www.ncbi.nlm.nih.gov/pmc/articles/PMC8571964/

[37] S. G. Dessie, A. Shapiro, M. J. Haviland, M. R. Hacker, and E. A. Elkadry, "Obliterative Versus Reconstructive Prolapse Repair for Women Older than 70: Is There an Optimal Approach?" *Urogynecology*, vol. 23, no. 1, p. 23, Feb. 2017. [Online]. Available: https://journals.lww.com/fpmrs/abstract/2017/01000/obliterative_versus_reconstructive_prolapse_repair.5.aspx

[38] K. J. Ko and K.-S. Lee, "Current surgical management of pelvic organ prolapse: Strategies for the improvement of surgical outcomes," *Investigative and Clinical Urology*, vol. 60, no. 6, pp. 413–424, Nov. 2019. [Online]. Available: https://www.ncbi.nlm.nih.gov/pmc/articles/PMC6821990/

[39] J. Houman, J. M. Weinberger, and K. S. Eilber, "Native Tissue Repairs for Pelvic Organ Prolapse," *Current Urology Reports*, vol. 18, no. 1, p. 6, Feb. 2017. [Online]. Available: https://doi.org/10.1007/s11934-017-0648-0

[40] B. J. BaesslerK, "Surgery for women with pelvic organ prolapse with or without stress urinary incontinence (Review)," *Cochrane Database of Systematic Reviews*, 2018. [Online]. Available: www.cochranelibrary.com

[41] "Risks and benefits of mesh in pelvic floor reconstruction," (Last accessed 3 November 2023). [Online]. Available: https://www.mayoclinic.org/diseases-conditions/pelvic-organ-prolapse/in-depth/transvaginal-mesh-complications/art-20110300

[42] A. Seifalian, Z. Basma, A. Digesu, and V. Khullar, "Polypropylene Pelvic Mesh: What Went Wrong and What Will Be of the Future?" *Biomedicines*, vol. 11, no. 3, p. 741, 2023.

[43] M. Yuan, M. Hu, F. Dai, Y. Fan, Z. Deng, H. Deng, and Y. Cheng, "Application of synthetic and natural polymers in surgical mesh for pelvic floor reconstruction," *Materials & Design*, vol. 209, p. 109984, Nov. 2021. [Online]. Available: https://linkinghub.elsevier.com/retrieve/pii/S0264127521005384

[44] "Surgical Mesh: Use and Complications in Women," (Last accessed 1 November 2023). [Online]. Available: https://my.clevelandclinic.org/health/articles/16298-surgical-mesh-use-and-complications-in-women

[45] K. Baylón, P. Rodríguez-Camarillo, A. Elías-Zúñiga, J. A. Díaz-Elizondo, R. Gilkerson, and K. Lozano, "Past, Present and Future of Surgical Meshes: A Review," *Membranes*, vol. 7, no. 3, p. 47, Aug. 2017. [Online]. Available: https://www.ncbi.nlm.nih.gov/pmc/articles/PMC5618132/

[46] P. K. Amid, "Classification of biomaterials and their related complications in abdominal wall hernia surgery," *Hernia*, vol. 1, no. 1, pp. 15–21, May 1997. [Online]. Available: https://doi.org/10.1007/BF02426382

[47] A. Coda, R. Lamberti, and S. Martorana, "Classification of prosthetics used in hernia repair based on weight and biomaterial," *Hernia*, vol. 16, no. 1, pp. 9–20, Feb. 2012. [Online]. Available: https://doi.org/10.1007/s10029-011-0868-z

[48] U. Klinge and B. Klosterhalfen, "Modified classification of surgical meshes for hernia repair based on the analyses of 1,000 explanted meshes," *Hernia : the journal of hernias and abdominal wall surgery*, vol. 16, pp. 251–8, May 2012.

[49] R. Rynkevic, "In vivo models and in silico simulations of mesh augmented prolapse repair," Ph.D. dissertation, KU Leuven Biomedical Sciences Group Faculty of Medicine Department of Development and Regeneration & University of Porto Faculty of Engeneering of the University of Porto, Jun. 2019. [Online]. Available: https://repositorio-aberto.up.pt/handle/10216/120996

[50] J. W. Moon and H. D. Chae, "Vaginal Approaches Using Synthetic Mesh to Treat Pelvic Organ Prolapse," *Annals of Coloproctology*, vol. 32, no. 1, p. 7, feb 2016. [Online]. Available: /pmc/articles/PMC4783513//pmc/articles/PMC4783513/?report=abstracthttps://www.ncbi.nlm.nih.gov/pmc/articles/PMC4783513/

[51] R. Rynkevic, M. E. Silva, P. Martins, T. Mascarenhas, J. L. Alves, and A. A. Fernandes, "Characterisation of polycaprolactone scaffolds made by melt electrospinning writing for pelvic organ prolapse correction - a pilot study," *Materials Today Communications*, vol. 32, no. January, p. 104101, 2022. [Online]. Available: https://doi.org/10.1016/j.mtcomm.2022.104101

[52] "Pelvic Organ Prolapse (POP): Surgical Mesh Considerations and Recommendations | FDA," (Last accessed 1 November 2023). [Online]. Available: https://www.fda.gov/medical-devices/urogynecologic-surgical-mesh-implants/pelvic-organ-prolapse-pop-surgical-mesh-considerations-and-recommendations

[53] J. Xue, T. Wu, Y. Dai, and Y. Xia, "Electrospinning and Electrospun Nanofibers: Methods, Materials, and Applications Graphical Abstract HHS Public Access," *Chem Rev*, vol. 119, no. 8, pp. 5298–5415, 2019.

[54] "Polymers | free full-text | overview of electrospinning for tissue engineering applications," (Last accessed 10 January 2024). [Online]. Available: https://www.mdpi.com/2073-4360/15/11/2418

[55] A. Keirouz, Z. Wang, V. S. Reddy, Z. K. Nagy, P. Vass, M. Buzgo, S. Ramakrishna, and N. Radacsi, "The History of Electrospinning: Past, Present, and Future Developments," *Advanced Materials Technologies*, vol. 8, no. 11, p. 2201723, Jun. 2023, publisher: Wiley. [Online]. Available: https://www.research.ed.ac.uk/en/publications/the-history-of-electrospinning-past-present-and-future-developmen

[56] M. Khan and S. J. S. Chelladurai, *Recent Developments in Nanofibers Research*. IntechOpen, May 2023. [Online]. Available: https://www.intechopen.com/books/11462

[57] "10 reasons to use electrospinning | nanoscience instruments," (Last accessed 10 January 2024). [Online]. Available: https://www.nanoscience.com/blogs/10-reasons-to-use-electrospinning/

[58] B. K. Tarus, N. Fadel, A. Al-Oufy, and M. El-Messiry, "Investigation of mechanical properties of electrospun poly (vinyl chloride) polymer nanoengineered composite," *Journal of Engineered Fibers and Fabrics*, vol. 15, 2020.

[59] X. Shi, W. Zhou, D. Ma, Q. Ma, D. Bridges, Y. Ma, and A. Hu, "Electrospinning of Nanofibers and Their Applications for Energy Devices," *Journal of Nanomaterials*, vol. 2015, 2015.

[60] A. Khalil, B. Lalia, R. Hashaikeh, and M. Khraisheh, "Electrospun metallic nanowires: Synthesis, characterization, and applications," *Journal of Applied Physics*, vol. 114, p. 171301, Nov. 2013.

[61] C. Salas, "4 - Solution electrospinning of nanofibers," in *Electrospun Nanofibers*, ser. Woodhead Publishing Series in Textiles, M. Afshari, Ed. Woodhead Publishing, Jan. 2017, pp. 73–108. [Online]. Available: https://www.sciencedirect.com/science/article/pii/B9780081009079000040

[62] A. Bachs-Herrera, O. Yousefzade, L. J. del Valle, and J. Puiggali, "Melt Electrospinning of Polymers: Blends, Nanocomposites, Additives and Applications," *Applied Sciences*, vol. 11, no. 4, p. 1808, Jan. 2021, number: 4 Publisher: Multidisciplinary Digital Publishing Institute. [Online]. Available: https://www.mdpi.com/2076-3417/11/4/1808

[63] E. Zdraveva, K. Bendelja, L. Bočkor, T. Dolenec, and B. Mijović, "Detection of Limbal Stem Cells Adhered to Melt Electrospun Silk Fibroin and Gelatin-Modified Polylactic Acid Scaffolds," *Polymers*, vol. 15, no. 3, feb 2023.

[64] "Melt electrospinning technology | Electrospinning nanofibers," (Last accessed 26 October 2023). [Online]. Available: https://www.nanofiberlabs.com/solutions/melt-electrospinning-technology.html

[65] M. Tahir, S. Vicini, and A. Sionkowska, "Electrospun Materials Based on Polymer and Biopolymer Blends—A Review," *Polymers*, vol. 15, no. 7, p. 1654, Jan. 2023, number: 7 Publisher: Multidisciplinary Digital Publishing Institute. [Online]. Available: https://www.mdpi.com/2073-4360/15/7/1654

[66] A. M. Arefin, N. R. Khatri, N. Kulkarni, and P. F. Egan, "Polymer 3D printing review: Materials, process, and design strategies for medical applications," *Polymers*, vol. 13, no. 9, pp. 1–24, 2021.

[67] "What is Additive manufacturing? | 7 Additive Manufacturing types," (Last accessed 26 October 2023). [Online]. Available: https://engineeringproductdesign.com/knowledge-base/additive-manufacturing-processes/

[68] S. Rouf, A. Malik, N. Singh, A. Raina, N. Naveed, M. I. H. Siddiqui, and M. I. U. Haq, "Additive manufacturing technologies: Industrial and medical applications," *Sustainable Operations and Computers*, vol. 3, no. March, pp. 258–274, 2022.

[69] "Schematic diagram of fused filament fabrication (FFF) [91] (reproduced... | Download Scientific Diagram," (Last accessed 26 October 2023). [Online]. Available: https://www.researchgate.net/figure/Schematic-diagram-of-fused-filament-fabrication-FFF-91-reproduced-from-91-with_fig16_341770623

[70] F. Afghah, C. Dikyol, M. Altunbek, and B. Koc, "Biomimicry in Bio-Manufacturing: Developments in Melt Electrospinning Writing Technology Towards Hybrid Biomanufacturing," *Applied Sciences 2019, Vol. 9, Page 3540*, vol. 9, no. 17, p. 3540, aug 2019. [Online]. Available: https://www.mdpi.com/2076-3417/9/17/3540/htmhttps://www.mdpi.com/2076-3417/9/17/3540

[71] Y. Jin, Q. Gao, C. Xie, G. Li, J. Du, J. Fu, and Y. He, "Fabrication of heterogeneous scaffolds using melt electrospinning writing: Design and optimization," *Materials and Design*, vol. 185, p. 108274, 2020. [Online]. Available: https://doi.org/10.1016/j.matdes.2019.108274

[72] S. Loewner, S. Heene, T. Baroth, H. Heymann, F. Cholewa, H. Blume, and C. Blume, "Recent advances in melt electro writing for tissue engineering for 3D printing of microporous scaffolds for tissue engineering," *Frontiers in Bioengineering and Biotechnology*, vol. 10, no. August, pp. 1–16, 2022.

[73] F. M. Wunner, O. Bas, N. T. Saidy, P. D. Dalton, E. M. D.-J. Pardo, and D. W. Hutmacher, "Melt Electrospinning Writing of Three-dimensional Poly(-caprolactone) Scaffolds with Controllable Morphologies for Tissue Engineering Applications," *Journal of Visualized Experiments : JoVE*, no. 130, p. 56289, Dec. 2017. [Online]. Available: https://www.ncbi.nlm.nih.gov/pmc/articles/PMC5908370/

[74] Y. Xie, Q. Fang, H. Zhao, Y. Li, Z. Lin, and J. Chen, "Effects of Six Processing Parameters on the Size of PCL Fibers Prepared by Melt Electrospinning Writing," *Micromachines*, vol. 14, no. 7, p. 1437, Jul. 2023. [Online]. Available: https://www.ncbi.nlm.nih.gov/pmc/articles/PMC10385759/

[75] S. Sterk, "Development of new surgical mesh geometries with different mechanical properties using the design freedom of 3d printing," Master's thesis, Faculdade de Engenharia da Universidade do Porto, 2023.

[76] J. A. P. Martins, "3D printed melt electrowriten drug eluting fibers: pilot study for prevention of infections associated with medical devices," Master's thesis, Faculdade de Engenharia da Universidade do Porto, 2023.

[77] E. M. Mellano, L. Y. Nakamura, J. M. Choi, D. C. Kang, T. Grisales, S. Raz, and L. V. Rodriguez, "The Role of Chronic Mesh Infection in Delayed-Onset Vaginal Mesh Complications or Recurrent Urinary Tract Infections: Results From Explanted Mesh Cultures," *Female Pelvic Medicine & Reconstructive Surgery*, vol. 22, no. 3, pp. 166–171, 2016.

[78] M. E. Falagas, S. Velakoulis, C. Iavazzo, and S. Athanasiou, "Mesh-related infections after pelvic organ prolapse repair surgery," *European Journal of Obstetrics & Gynecology and Reproductive Biology*, vol. 134, no. 2, pp. 147–156, Oct. 2007. [Online]. Available: https://www.sciencedirect.com/science/article/pii/S0301211507001418

[79] L. Boulanger, M. Boukerrou, C. Rubod, P. Collinet, A. Fruchard, R. J. Courcol, and M. Cosson, "Bacteriological analysis of meshes removed for complications after surgical management of urinary incontinence or pelvic organ prolapse," *International Urogynecology Journal*, vol. 19, no. 6, pp. 827–831, Jun. 2008. [Online]. Available: https://doi.org/10.1007/s00192-007-0537-z

[80] G. Pietrocola, D. Campoccia, C. Motta, L. Montanaro, C. R. Arciola, and P. Speziale, "Colonization and Infection of Indwelling Medical Devices by Staphylococcus aureus with an Emphasis on Orthopedic Implants," *International Journal of Molecular Sciences*, vol. 23, no. 11, p. 5958, May 2022. [Online]. Available: https://www.ncbi.nlm.nih.gov/pmc/articles/PMC9180976/

[81] G. Y. C. Cheung, J. S. Bae, and M. Otto, "Pathogenicity and virulence of Staphylococcus aureus," *Virulence*, vol. 12, no. 1, pp. 547–569, 2021. [Online]. Available: https://www.ncbi.nlm.nih.gov/pmc/articles/PMC7872022/

[82] C. H. Feng, D. D. Stevenson, B. Kahn, and P. A. Higginbottom, "Methicillin-resistant *Staphylococcus aureus* pelvic abscesses in a female after gynecologic pelvic surgery," *American Journal of Obstetrics and Gynecology*, vol. 205, no. 5, pp. e4–e5, Nov. 2011. [Online]. Available: https://www.sciencedirect.com/science/article/pii/S0002937811006168

[83] M. Mueller and C. R. Tainter, "Escherichia coli Infection," in *StatPearls*. Treasure Island (FL): StatPearls Publishing, 2024. [Online]. Available: http://www.ncbi.nlm.nih.gov/books/NBK564298/

[84] H. N. Shah and G. H. Badlani, "Mesh complications in female pelvic floor reconstructive surgery and their management: A systematic review," *Indian Journal of Urology : IJU : Journal of the Urological Society of India*, vol. 28, no. 2, pp. 129–153, 2012. [Online]. Available: https://www.ncbi.nlm.nih.gov/pmc/articles/PMC3424888/

[85] M. Kim, S. Lee, H. S. Kim, M. Y. Kwon, J. Yoo, and M. J. Kim, "Microbiome alterations in women with pelvic organ prolapse and after anatomical restorative interventions," *Scientific Reports*, vol. 13, no. 1, p. 17547, Oct. 2023. [Online]. Available: https://www.nature.com/articles/s41598-023-44988-6

[86] M. Drexler and I. o. Medicine (US), "How Infection Works," in *What You Need to Know About Infectious Disease*. National Academies Press (US), 2010. [Online]. Available: https://www.ncbi.nlm.nih.gov/books/NBK209710/

[87] P. Li, R. Yin, J. Cheng, and J. Lin, "Bacterial Biofilm Formation on Biomaterials and Approaches to Its Treatment and Prevention," *International Journal of Molecular Sciences*, vol. 24, no. 14, p. 11680, Jul. 2023. [Online]. Available: https://www.ncbi.nlm.nih.gov/pmc/articles/PMC10380251/

[88] S. Vani, K. Vadakkan, and B. Mani, "A narrative review on bacterial biofilm: its formation, clinical aspects and inhibition strategies," *Future Journal of Pharmaceutical Sciences*, vol. 9, no. 1, p. 50, Jun. 2023. [Online]. Available: https://doi.org/10.1186/s43094-023-00499-9

[89] P. P. Kalelkar, M. Riddick, and A. J. García, "Biomaterial-based delivery of antimicrobial therapies for the treatment of bacterial infections," *Nature reviews. Materials*, vol. 7, no. 1, pp. 39–54, Jan. 2022. [Online]. Available: https://www.ncbi.nlm.nih.gov/pmc/articles/PMC8938918/

[90] Z. Mardina, J. Venezuela, C. Maher, Z. Shi, M. S. Dargusch, and A. Atrens, "Design, mechanical and degradation requirements of biodegradable metal mesh for pelvic floor reconstruction," *Biomaterials Science*, vol. 10, no. 13, pp. 3371–3392, Jun. 2022, publisher: The Royal Society of Chemistry. [Online]. Available: https://pubs.rsc.org/en/content/articlelanding/2022/bm/d2bm00179a

[91] "About azithromycin," Jan. 2022, (Last accessed 10 March 2024). [Online]. Available: https://www.nhs.uk/medicines/azithromycin/about-azithromycin/

[92] P. Labs, "Zithromax® (azithromycin) for iv infusion only initial us approval," U.S. Food and Drug Administration, 2016, (Last accessed 7 June 2024). [Online]. Available: https://www.accessdata.fda.gov/drugsatfda_docs/label/2016/050733s040lbl.pdf

[93] "Azithromycin 83905-01-5," (Last accessed 2 May 2024). [Online]. Available: http://www.sigmaaldrich.com/

[94] B. J. Chaves and P. Tadi, "Gentamicin," in *StatPearls*. Treasure Island (FL): StatPearls Publishing, 2023. [Online]. Available: http://www.ncbi.nlm.nih.gov/books/NBK557550/

[95] "Gentamicin sulfate | DNase I Inhibitor | MedChemExpress," (Last accessed 1 May 2024). [Online]. Available: https://www.medchemexpress.com/Gentamicin__sulfate_.html

[96] "Gentamicin Sulfate Pharmaceutical Secondary Standard; Certified Reference Material 1405-41-0," (Last accessed 1 May 2024). [Online]. Available: http://www.sigmaaldrich.com/

[97] "Gentamicin topical: Uses, Side Effects, Interactions, Pictures, Warnings & Dosing - WebMD," (Last accessed 1 May 2024). [Online]. Available: https://www.webmd.com/drugs/2/drug-75145/gentamicin-topical/details

[98] K. WARD and R. N. THEILER, "Once-daily Dosing of Gentamicin in Obstetrics and Gynecology," *Clinical obstetrics and gynecology*, vol. 51, no. 3, pp. 498–506, Sep. 2008. [Online]. Available: https://www.ncbi.nlm.nih.gov/pmc/articles/PMC2650501/

[99] I. Poudel, M. Annaji, C. Zhang, P. R. Panizzi, R. D. Arnold, A. Kaddoumi, R. H. Amin, S. Lee, N. Shamsaei, and R. J. Babu, "Gentamicin Eluting 3D-Printed Implants for Preventing Post-Surgical Infections in Bone Fractures," *Molecular Pharmaceutics*, vol. 20, no. 8, pp. 4236–4255, Aug. 2023.

[100] J. A. Weisman, D. H. Ballard, U. Jammalamadaka, K. Tappa, J. Sumerel, H. B. D'Agostino, D. K. Mills, and P. K. Woodard, "3D Printed Antibiotic and Chemotherapeutic Eluting Catheters for Potential Use in Interventional Radiology: In Vitro Proof of Concept Study," *Academic Radiology*, vol. 26, no. 2, pp. 270–274, Feb. 2019.

[101] "gentamicin sulfate | CAS 1405-41-0 | LGC Standards," (Last accessed 1 May 2024). [Online]. Available: https://www.lgcstandards.com/BR/pt/Gentamicin-sulfate/p/BP%20174

[102] J. S. Christian, "The quinolone antibiotics," *Primary Care Update for OB/GYNS*, vol. 3, no. 3, pp. 87–92, May 1996. [Online]. Available: https://www.sciencedirect.com/science/article/pii/1068607X96000029

[103] "Ciprofloxacin = 98 HPLC 85721-33-1," (Last accessed 2 May 2024). [Online]. Available: https://www.sigmaaldrich.com/PT/en/product/sial/17850

[104] J. C. Kade and P. D. Dalton, "Polymers for Melt Electrowriting," *Advanced Healthcare Materials*, vol. 10, no. 1, 2021.

[105] M. A. Mohamed, J. Jaafar, A. F. Ismail, M. H. D. Othman, and M. A. Rahman, "Chapter 1 - Fourier Transform Infrared (FTIR) Spectroscopy," in *Membrane Characterization*, N. Hilal, A. F. Ismail, T. Matsuura, and D. Oatley-Radcliffe, Eds. Elsevier, Jan. 2017, pp. 3–29. [Online]. Available: https://www.sciencedirect.com/science/article/pii/B9780444637765000012

[106] "Agilent Cary 630 Ftir Spectrometer," (Last accessed 17 May 2024). [Online]. Available: https://www.indiamart.com/proddetail/agilent-cary-630-ftir-spectrometer-21994483333.html

[107] M. I. A. Pinto, "Melt electrowriting prototype optimization for medical-grade polycaprolactone mesh printing," Master's thesis, Faculdade de Engenharia da Universidade do Porto, 2022.

[108] M. E. Silva, F. Pinheiro, and A. A. Fernandes, "Characterization of biodegradable PCL cog threads for pelvic organ prolapse treatment," *XLIV Ibero-Latin American Congress on Computational Methods in Engineering*, vol. 5, no. 05, 2024, number: 05. [Online]. Available: https://publicacoes.softaliza.com.br/cilamce2023/article/view/5032

[109] S. Roman, N. Mangir, L. Hympanova, C. R. Chapple, J. Deprest, and S. MacNeil, "Use of a simple in vitro fatigue test to assess materials used in the surgical treatment of stress urinary incontinence and pelvic organ prolapse," *Neurourology and Urodynamics*, vol. 38, no. 1, pp. 107–115, jan 2019.

[110] R. Scaffaro, L. Botta, A. Maio, and G. Gallo, "Incorporation of an Antibiotic in Poly(Lactic Acid) and Polypropylene by Melt Processing," *Journal of Applied Biomaterials & Functional Materials*, vol. 14, no. 3, pp. e240–e247, Jul. 2016, publisher: SAGE Publications. [Online]. Available: https://doi.org/10.5301/jabfm.5000285

[111] P. Kralik, V. Beran, and I. Pavlik, "Enumeration of Mycobacterium avium subsp. paratuberculosis by quantitative real-time PCR, culture on solid media and optical densitometry," *BMC Research Notes*, vol. 5, p. 114, Feb. 2012. [Online]. Available: https://www.ncbi.nlm.nih.gov/pmc/articles/PMC3305647/

[112] H. Lade, J. H. Park, S. H. Chung, I. H. Kim, J.-M. Kim, H.-S. Joo, and J.-S. Kim, "Biofilm Formation by Staphylococcus aureus Clinical Isolates is Differentially Affected by Glucose and Sodium Chloride Supplemented Culture Media," *Journal of Clinical Medicine*, vol. 8, no. 11, p. 1853, Nov. 2019. [Online]. Available: https://www.ncbi.nlm.nih.gov/pmc/articles/PMC6912320/

[113] C. Sabença, E. Costa, S. Sousa, L. Barros, A. Oliveira, S. Ramos, G. Igrejas, C. Torres, and P. Poeta, "Evaluation of the Ability to Form Biofilms in KPC-Producing and ESBL-Producing Klebsiella pneumoniae Isolated from Clinical Samples," *Antibiotics*, vol. 12, no. 7, p. 1143, Jul. 2023. [Online]. Available: https://www.mdpi.com/2079-6382/12/7/1143

[114] P. A. L. de Sousa Martins, "Experimental and numerical studies of soft biological tissues," Ph.D. dissertation, Faculdade de Engenharia da Universidade do Porto, 2010.

[115] U. Klinge, J. Otto, and T. Mühl, "High Structural Stability of Textile Implants Prevents Pore Collapse and Preserves Effective Porosity at Strain," *BioMed Research International*, vol. 2015, no. 1, p. 953209, 2015, _eprint: https://onlinelibrary.wiley.com/doi/pdf/10.1155/2015/953209. [Online]. Available: https://onlinelibrary.wiley.com/doi/abs/10.1155/2015/953209

[116] G. L. Clark-Patterson, L. M. Buchanan, B. O. Ogola, M. Florian-Rodriguez, S. H. Lindsey, R. De Vita, and K. S. Miller, "Smooth muscle contribution to vaginal viscoelastic response," *Journal of the Mechanical Behavior of Biomedical Materials*, vol. 140, p. 105702, Apr. 2023.

[117] A. Głuchowski and W. Sas, "Long-Term Cyclic Loading Impact on the Creep Deformation Mechanism in Cohesive Materials," *Materials*, vol. 13, no. 17, p. 3907, Sep. 2020. [Online]. Available: https://www.ncbi.nlm.nih.gov/pmc/articles/PMC7503864/

[118] A. M. Vinogradov and S. Schumacher, "Cyclic Creep of Polymers and Polymer-Matrix Composites," *Mechanics of Composite Materials*, vol. 37, no. 1, pp. 29–34, Jan. 2001. [Online]. Available: https://doi.org/10.1023/A:1010683609939

[119] H. Liu, L. Zhang, K. Lu, and B. Gao, "Study of Cyclic Plasticity and Creep Ratchet Behavior of PTFE," *Applied Sciences*, vol. 13, p. 10039, Sep. 2023.

[120] T. Elzein, M. Nasser-Eddine, C. Delaite, S. Bistac, and P. Dumas, "FTIR study of polycaprolactone chain organization at interfaces," *Journal of Colloid and Interface Science*, vol. 273, no. 2, pp. 381–387, May 2004. [Online]. Available: https://www.sciencedirect.com/science/article/pii/S002197970400102X

[121] C. Dwivedi, H. Panday, A. Pandey, and P. Ramteke, "Fabrication and Assessment of Gentamicin Loaded Electrospun Nanofibrous Scaffolds as a Quick Wound Healing Dressing Material," *Current Nanoscience*, vol. 11, pp. 222–228, Feb. 2015.

[122] S. Durgapal, S. Mukhopadhyay, and L. Goswami, "Preparation, characterization and evaluation of floating microparticles of ciprofloxacin," *International Journal of Applied Pharmaceutics*, vol. 9, p. 1, Dec. 2016.

[123] Z. Xu, Y. Liang, S. Lin, D. Chen, B. Li, L. Li, and Y. Deng, "Crystal Violet and XTT Assays on Staphylococcus aureus Biofilm Quantification," *Current Microbiology*, vol. 73, no. 4, pp. 474–482, Oct. 2016. [Online]. Available: https://doi.org/10.1007/s00284-016-1081-1

[124] S. Shaikh, Z. Khatri, K. W. Oh, I.-S. Kim, and S. Kim, "Preparation and characterization of hybrid polycaprolactone/cellulose ultrafine fibers via electrospinning," *Macromolecular Research*, vol. 22, pp. 562–568, May 2014.

[125] C. C. R. Ramos, J. L. A. Roque, D. B. Sarmiento, L. E. G. Suarez, J. T. P. Sunio, K. I. B. Tabungar, G. S. C. Tengco, P. C. Rio, and A. L. Hilario, "Use of ultraviolet-C in environmental sterilization in hospitals: A systematic review on efficacy and safety," *International Journal of Health Sciences*, vol. 14, no. 6, pp. 52–65, 2020. [Online]. Available: https://www.ncbi.nlm.nih.gov/pmc/articles/PMC7644456/

[126] P. Innocenzi, L. Malfatti, S. Costacurta, T. Kidchob, M. Piccinini, and A. Marcelli, "Evaporation of Ethanol and Ethanol -Water Mixtures Studied by Time-Resolved Infrared Spectroscopy," *The Journal of Physical Chemistry A*, vol. 112, no. 29, pp. 6512–6516, Jul. 2008, publisher: American Chemical Society. [Online]. Available: https://doi.org/10.1021/jp7111395

[127] W.-Y. Chuang, T.-H. Young, D.-M. Wang, R.-L. Luo, and Y.-M. Sun, "Swelling behavior of hydrophobic polymers in water/ethanol mixtures," *Polymer*, vol. 41, no. 23, pp. 8339–8347, 2000. [Online]. Available: https://www.sciencedirect.com/science/article/pii/S0032386100001762

[128] M. Bartnikowski, T. R. Dargaville, S. Ivanovski, and D. W. Hutmacher, "Degradation mechanisms of polycaprolactone in the context of chemistry, geometry and environment," *Progress in Polymer Science*, vol. 96, pp. 1–20, Sep. 2019. [Online]. Available: https://www.sciencedirect.com/science/article/pii/S0079670018303915

[129] "Advantages and Disadvantages of FTIR Spectroscopy," (Last accessed 15 May 2024). [Online]. Available: https://www.chemlabgenius.com/advantages-and-disadvantages-of-ftir-spectroscopy/

[130] S. Bhadra, "Formulation & process development of azithromycin ophthalmic nanosuspension," *International Journal of Pharmacy and Pharmaceutical Sciences*, vol. 5, pp. 490–497, Oct. 2013.

[131] A. Arakkal, P. Sirajunnisa, and G. S. Sailaja, "Natural rubber latex films with effective growth inhibition against S. aureus via surface conjugated gentamicin," *Journal of Bioactive and Compatible Polymers*, vol. 38, no. 3, pp. 220–233, May 2023, publisher: SAGE Publications Ltd STM. [Online]. Available: https://doi.org/10.1177/08839115231153823

[132] S. Sahoo, C. K. Chakraborti, and S. C. Mishra, "Qualitative analysis of controlled release ciprofloxacin/carbopol 934 mucoadhesive suspension," *Journal of Advanced Pharmaceutical Technology & Research*, vol. 2, no. 3, pp. 195–204, 2011. [Online]. Available: https://www.ncbi.nlm.nih.gov/pmc/articles/PMC3217701/

[133] S. Sahoo, C. Chakraborti, S. Mishra, U. Nanda, and S. Naik, "FTIR and XRD investigations of some fluoroquinolones," *International Journal of Pharmacy and Pharmaceutical Sciences*, vol. 3, pp. 165–170, Apr. 2011.

[134] E. F. Haney, M. J. Trimble, J. T. Cheng, Q. Vallé, and R. E. W. Hancock, "Critical Assessment of Methods to Quantify Biofilm Growth and Evaluate Antibiofilm Activity of Host Defence Peptides," *Biomolecules*, vol. 8, no. 2, p. 29, Jun. 2018, number: 2 Publisher: Multidisciplinary Digital Publishing Institute. [Online]. Available: https://www.mdpi.com/2218-273X/8/2/29

[135] H. M. Naimi, H. Rasekh, A. Z. Noori, and M. A. Bahaduri, "Determination of antimicrobial susceptibility patterns in Staphylococcus aureus strains recovered from patients at two main health facilities in Kabul, Afghanistan," *BMC Infectious Diseases*, vol. 17, p. 737, Nov. 2017. [Online]. Available: https://www.ncbi.nlm.nih.gov/pmc/articles/PMC5707873/

[136] S. Nair, S. Desai, N. Poonacha, A. Vipra, and U. Sharma, "Antibiofilm Activity and Synergistic Inhibition of Staphylococcus aureus Biofilms by Bactericidal Protein P128 in Combination with Antibiotics," *Antimicrobial Agents and Chemotherapy*, vol. 60, no. 12, pp. 7280–7289, Nov. 2016. [Online]. Available: https://www.ncbi.nlm.nih.gov/pmc/articles/PMC5119008/

[137] N. Hoiby, K.-A. Henneberg, H. Wang, C. Stavnsbjerg, T. Bjarnsholt, O. Ciofu, U. R. Johansen, and T. Sams, "Formation of *Pseudomonas aeruginosa* inhibition zone during tobramycin disk diffusion is due to transition from planktonic to biofilm mode of growth," *International Journal of Antimicrobial Agents*, vol. 53, no. 5, pp. 564–573, May 2019. [Online]. Available: https://www.sciencedirect.com/science/article/pii/S0924857918303856

[138] A.-L. Prunier, B. Malbruny, D. Tandé, B. Picard, and R. Leclercq, "Clinical Isolates of Staphylococcus aureus with Ribosomal Mutations Conferring Resistance to Macrolides," *Antimicrobial Agents and Chemotherapy*, vol. 46, no. 9, pp. 3054–3056, Sep. 2002. [Online]. Available: https://www.ncbi.nlm.nih.gov/pmc/articles/PMC127407/

[139] S. Bhattacharya, R. Bir, and T. Majumdar, "Evaluation of Multidrug Resistant Staphylococcus aureus and their Association with Biofilm Production in a Tertiary Care Hospital, Tripura, Northeast India," *Journal of Clinical and Diagnostic Research : JCDR*, vol. 9, no. 9, pp. DC01–DC04, Sep. 2015. [Online]. Available: https://www.ncbi.nlm.nih.gov/pmc/articles/PMC4606231/

[140] J. M. O. Oduor, N. Onkoba, F. Maloba, W. O. Arodi, and A. Nyachieo, "Efficacy of lytic Staphylococcus aureus bacteriophage against multidrug-resistant Staphylococcus aureus in mice," *The Journal of Infection in Developing Countries*, vol. 10, no. 11, pp. 1208–1213, Nov. 2016, number: 11. [Online]. Available: https://jidc.org/index.php/journal/article/view/27886033

[141] K. Zawadzka, M. Nowak, I. Piwoński, and K. Lisowska, "The Synergy of Ciprofloxacin and Carvedilol against Staphylococcus aureus–Prospects of a New Treatment Strategy?" *Molecules*, vol. 24, no. 22, p. 4104, Jan. 2019, number: 22 Publisher: Multidisciplinary Digital Publishing Institute. [Online]. Available: https://www.mdpi.com/1420-3049/24/22/4104

[142] J. Cayron, A. Dedieu-Berne, and C. Lesterlin, "Bacterial filaments recover by successive and accelerated asymmetric divisions that allow rapid post-stress cell proliferation," *Molecular Microbiology*, vol. 119, no. 2, pp. 237–251, Feb. 2023.

[143] E. Bizot, A. Cointe, P. Bidet, P. Mariani-Kurkdjian, C. A. Hobson, C. Courroux, S. Liguori, A. Bridier-Nahmias, M. Magnan, M. Merimèche, F. Caméléna, B. Berçot, F.-X. Weill, S. Lefèvre, S. Bonacorsi, and A. Birgy, "Azithromycin Resistance in Shiga Toxin-Producing Escherichia coli in France between 2004 and 2020 and Detection of mef(C)-mph(G) Genes," *Antimicrobial Agents and Chemotherapy*, vol. 66, no. 2, pp. e01 949–21, 2022. [Online]. Available: https://www.ncbi.nlm.nih.gov/pmc/articles/PMC8846429/

[144] J. Arapović, G. Kompes, K. Dedic, S. Teskeredžić, M. Ostojic, M. Travar, N. Tihić, J. Delić, S. Skočibušić, M. Zekiri–Sivro, A. Verhaz, D. Piljic, L. Laura, S. Duvnjak, M. Zdelar–Tuk, M. Arapović, E. Šabotić, I. Reil, J. Nikolić, and S. Špičić, "Antimicrobial resistance profiles of human Brucella melitensis isolates in three different microdilution broths: First multicentre study in Bosnia and Herzegovina," *Journal of Global Antimicrobial Resistance*, vol. 29, Feb. 2022.

[145] E. Mursyida, O. Misfa, S. B. Pratiwi, and A. Shinde, "In Vitro Sensitivity Test of Escherichia coli ATCC 25922 to Various Antibiotics with Well Diffusion Method," *Jurnal Kesehatan Prima*, vol. 17, no. 2, pp. 42–47, Aug. 2023, number: 2. [Online]. Available: http://jkp.poltekkes-mataram.ac.id/index.php/home/article/view/1003

[146] K. M. Hallinen, J. Karslake, and K. B. Wood, "Delayed antibiotic exposure induces population collapse in enterococcal communities with drug-resistant subpopulations," *eLife*, vol. 9, p. e52813, 2020. [Online]. Available: https://www.ncbi.nlm.nih.gov/pmc/articles/PMC7159880/